



THE HONG KONG  
POLYTECHNIC UNIVERSITY

香港理工大學

Pao Yue-kong Library

包玉剛圖書館

---

## Copyright Undertaking

This thesis is protected by copyright, with all rights reserved.

**By reading and using the thesis, the reader understands and agrees to the following terms:**

1. The reader will abide by the rules and legal ordinances governing copyright regarding the use of the thesis.
2. The reader will use the thesis for the purpose of research or private study only and not for distribution or further reproduction or any other purpose.
3. The reader agrees to indemnify and hold the University harmless from and against any loss, damage, cost, liability or expenses arising from copyright infringement or unauthorized usage.

### IMPORTANT

If you have reasons to believe that any materials in this thesis are deemed not suitable to be distributed in this form, or a copyright owner having difficulty with the material being included in our database, please contact [lbsys@polyu.edu.hk](mailto:lbsys@polyu.edu.hk) providing details. The Library will look into your claim and consider taking remedial action upon receipt of the written requests.

**POLYMER OPTICAL FIBER  
ASE LIGHT SOURCE AND RANDOM LASER**

**WING-KIN EDWARD CHAN**

**Ph.D**

**The Hong Kong Polytechnic University**

**2015**

**The Hong Kong Polytechnic University**

**Department of Electrical Engineering**

**Polymer Optical Fiber ASE Light Source and Random Laser**

**Wing-Kin Edward Chan**

**A thesis submitted in partial fulfilment of the requirements**

**for the degree of Doctor of Philosophy**

**July 2013**

## CERTIFICATE OF ORIGINALITY

I hereby declare that this thesis is my own work and that, to the best of my knowledge and belief, it reproduces no material previously published or written, nor material that has been accepted for the award of any other degree or diploma, except where due acknowledgement has been made in the text.

\_\_\_\_\_ (Signed)

Wing-Kin Edward Chan (Name of student)

## ABSTRACT

In this thesis, I investigate aspects of Rhodamine 640 (Rh640)-dye-doped polymer optical fiber (POF) with integrated optical cavity formed by gold mirrors on fiber ends, including design, fabrication, and characterization.

POF fabrication offers great flexibility in core and cladding structural designs as well as allows incorporation of a wide variety of functional materials. This allows the development of dye-doped POF light sources with specific functions. I also investigate POF with a lightly Rh640-dye-doped core and relatively highly Rh640-dye-doped cladding step-index structure and show that a significant improvement in the emission intensity and photostability is achieved.

The latest work has been focused on development of solid core fiber random lasers to experimentally verify some of the published random laser theories, which are still uncertain. I fabricated a solid core POF random laser, with Titanium dioxide ( $\text{TiO}_2$ ) as scatterers and Rh640 dye as gain medium and performed the first demonstration of random lasing in POF. Evenly distributed discrete narrow random lasing peaks with

peak linewidth of 0.5nm and peak separation of 0.9nm in emission spectrum are observed.

A systematic experimental investigation of random laser with various densities of scatterer has been carried out. After optimization of scatterer density, single-mode POF random lasing is achieved for 20ppm  $\text{TiO}_2$  (400nm diameter), POF core diameter of  $\sim 400\text{nm}$ , with scattering mean free path = 11.9mm. Since the modes of a random laser are sensitive to the scatterers, we may use the random laser as a sensor for anything that modifies the scattering characteristics of the medium. Therefore, the study of the effect of perturbation made to the lasing mechanism of random fiber laser and the associated emission spectra characteristics is proposed for future work.

## ACKNOWLEDGEMENTS

First of all, I would like to express my sincerest thanks to my chief supervisor, Prof. Tam Hwa-Yaw of EE department. He provided me with valuable professional knowledge in polymer fiber optics and guided me to this area. His advice and constant support always make me feel confident every time when we discuss the problems encountered in my research works.

I would also like to express my sincerest thanks to my co-supervisor, Prof. Chan Wong Lai-Wa Helen of AP department. She brought me to this interesting and promising research field. Apart from research related issues, she sets a good example in personal characters which is of great benefit to my future professional career.

Research facilities and technical support from our department are gratefully acknowledged. I would also like to express my gratitude to numerous research group members and classmates in our department, especially, to Dr. Tse Ming-Leung Vincent, Dr. Pun Chi-Fung Jeff, and Mr. Cheng Xin.

Special thanks to Dr. Li Feng. His rich simulation knowledge makes the theoretical section of this thesis become possible. And special thanks to Prof. Wai Ping-Kong Alex's interest in this research topic.

I am deeply indebted to my wife and son, my parents, my grandmother, and my sister and brothers. Without their love, understanding, patience, and support, no achievement in my research works can become a reality.

# TABLE OF CONTENTS

<b>CERTIFICATE OF ORIGINALITY</b>	I
<b>ABSTRACT</b>	II
<b>ACKNOWLEDGEMENTS</b>	IV
<b>TABLE OF CONTENTS</b>	VI
<b>LIST OF FIGURES</b>	IX
<b>LIST OF TABLES</b>	XIX
<b>CHAPTER 1</b>	
<b>Introduction</b>	1
1.1 Background	1
1.2 Objective	4
1.3 Methodology	5
1.4 Outline of the thesis	8
1.5 Reference	11
<b>CHAPTER 2</b>	
<b>Literature Review</b>	14
2.1 Development of dye lasers	14
2.2 Solid-state dye lasers	17
2.2.1 Cylindrical rod dye lasers	17
2.2.2 Thin film and slab dye lasers	19
2.2.3 Optical fiber dye lasers	23
2.3 Optical cavity of solid-state dye lasers	26
2.3.1 External cavity	26
2.3.2 Integrated cavity	27
2.4 Development of random lasers	31
2.4.1 Random laser with incoherent feedback	32
2.4.2 Random laser with coherent feedback	36
2.4.3 Transition between two kinds of random lasers	38
2.5 Applications of random lasers	40
2.5.1 Medical diagnostics	40
2.5.2 Speckle-free full-field imaging	42
2.6 The future of random lasers	46
2.7 Reference	47

<b>CHAPTER 3</b>	
<b>POF Dye Lasers and Random Lasers: Materials and Structures</b>	<b>55</b>
3.1 Organic laser dyes	55
3.1.1 Structure and properties of organic laser dyes	55
3.1.2 Light absorption and emission of organic laser dyes	56
3.1.3 Xanthene dyes	58
3.2 Polymeric materials	62
3.2.1 Polymerization techniques	63
3.2.1.1 Solution polymerization	63
3.2.1.2 Bulk polymerization	64
3.2.1.3 Advantages and disadvantages of the solution and bulk polymerization	65
3.2.2 Evaluation of refractive index from chemical structure of polymer	67
3.3 Polymer optical fibers	69
3.3.1 Optical fibers	69
3.3.2 Principle of guiding light in optical fibers	70
3.3.3 Multi-mode fibers and single-mode fibers	72
3.4 POF dye lasers	73
3.4.1 Materials for dye-doped polymeric preform and POF dye lasers	73
3.4.2 Fabrication of dye-doped polymeric preform and POF dye lasers	78
3.5 Random lasers	81
3.5.1 Two kinds of random lasers	83
3.5.2 Scattering of Light in random lasers	85
3.5.3 Three regimes of scattering in random lasing	89
3.5.4 Advantages and disadvantages of random lasers	91
3.6 Reference	93
<b>CHAPTER 4</b>	
<b>POF ASE Light Source</b>	<b>97</b>
4.1 Introduction	97
4.2 Effect of reflectance of gold mirrors coated output coupler on emission characteristics of dye-doped POFs	98
4.2.1 Fabrication	98
4.2.2 Gold mirror coating on fiber end by DC sputtering	99
4.2.3 Study of emission characteristics of Rh640-dye-doped POF with both end-faces coated with gold mirrors	104
4.2.4 Conclusion	112
4.3 Effect of dye concentration in core of Rh640-dye-doped POF on emission characteristics	113
4.3.1 Fabrication	113
4.3.2 Experiment	115

4.3.3 Emission spectra of POF with 20ppm Rh640-dye-doped core POF and 200ppm Rh640-dye-doped cladding	120
4.3.4 Photostability	125
4.3.5 Conclusion	128
4.4 Reference	128
<b>CHAPTER 5</b>	
<b>POF Random Lasers</b>	130
5.1 Introduction	130
5.2 Fabrication of random lasers	131
5.3 Emission spectra characterization of random lasers	133
5.3.1 Lasing spectra of dye-doped POF without nanoparticles	133
5.3.2 Laser action in POF random lasers	139
5.3.3 Lasing mode analysis of POF random lasers	151
5.4 Conclusion	154
5.5 Reference	155
<b>CHAPTER 6</b>	
<b>Effect of Scatterers Concentration on Lasing Properties of POF Random Lasers</b>	156
6.1 Introduction	156
6.2 Fabrication of POF random lasers	157
6.3 Emission spectra of POF random lasers	161
6.3.1 Lasing spectra characterization of dye-doped POF with low concentration of TiO <sub>2</sub> nanoparticles	161
6.3.2 Lasing spectra characterization of dye-doped POF with high concentration of TiO <sub>2</sub> nanoparticles	171
6.3.3 Effect of scatterers concentration on random laser threshold	176
6.4 Theoretical investigation of statistical regimes in random laser emission	177
6.5 Conclusion	188
6.6 Reference	189
<b>CHAPTER 7</b>	
<b>Conclusions and Suggestions for Future Research</b>	190
<b>Appendix 1</b>	193

## LIST OF FIGURES

Fig. 2.1.	Number of publications on dye laser since the discovery of dye laser in 1966.	16
Fig. 2.2	Laser conversion efficiency (%) for (a) Rh640(ClO <sub>4</sub> ) and (b) Rh6G(ClO <sub>4</sub> ) doped PMMA slabs as a function dye concentration [19].	20
Fig. 2.3.	Comparison of laser emission spectra from a dye solution and doped PMMA slab of (a) Rh640(ClO <sub>4</sub> ) and (b) Rh6G(ClO <sub>4</sub> ) [19].	20
Fig. 2.4.	Schematic diagram of experimental set-up for characterization of film dye laser [18].	22
Fig. 2.5.	Emission spectra from Rh6G doped PMMA film of (a) 50 μm and (b) 130 μm thickness when optically excited [18].	23
Fig. 2.6.	Cross-sectional structures of the Rh6G doped GI-POF laser and the Rh6G doped bulk fiber laser [22].	24
Fig. 2.7.	Lasing performances of the GI-POF laser and bulk fiber laser [22].	25
Fig. 2.8.	Lifetime of the GI-POF laser and the bulk fiber laser [22].	26
Fig. 2.9.	Aluminum coatings on the Rh6G-doped PMMA thin slab: side coating on surface A and back-coating on surface B with respect to the nitrogen laser [20].	27
Fig. 2.10(a).	Dye laser output as a function of Rh6G-doped PMMA slab thickness without aluminum coating [21].	28
Fig. 2.10(b).	Effect of side-coated aluminum reflector on the dye laser output [21].	29
Fig. 2.10(c).	Effect of dual-coating of aluminum coatings on surfaces A and B on dye laser output [21].	29
Fig. 2.11.	Random lasing emission spectra of (a) solution of Rh640 perchlorate dye in methanol containing TiO <sub>2</sub> nanoparticles, <i>a</i> corresponds to spectrum from sample without nanoparticles at pump well above threshold, <i>b</i> and <i>c</i> corresponds to spectra from samples with	35

nanoparticles at pump well below and well above threshold respectively, and (b) polymeric sheet containing Rh640 perchlorate dye with TiO<sub>2</sub> nanoparticles [34].

- Fig. 2.12. Emission spectra from ZnO powder when the intensity is (from bottom to top) 400, 562, 763, 875, and 1387kWcm<sup>-2</sup>. The inset in the middle graph shows the formation of closed loop path for recurrent multiple scattering of light in the powder [35]. 37
- Fig. 2.13. (a) Spatial distribution of emission intensity in ZnO powder at pump energy below threshold, and (b) above threshold [35]. 38
- Fig. 2.14. Random lasing emission spectra of human colon tissues infiltrated with a concentrated laser dye, namely R6G. (a) Two typical random lasing emission spectra from a healthy tissue, of which microscopic image is shown in (b). The narrow spectral lines are in fact coherent laser emission modes. The inset shows schematically closed random resonators formed due to scatterers in the gain medium. (c) and (d), same as in (a) and (b), respectively, but for a malignant colon tissue. There are more lines in the laser emission spectra in (c) that are due to more resonators in the tumor; these are caused by the excess disorder that is apparent in (d) [43]. 41
- Fig. 2.15. Fig. 2.15. (a) Schematic of experimental set-up. Five light sources with different degrees of spatial coherence were used: a light-emitting diode (LED), a random laser (RL), an amplified spontaneous emission (ASE) source, a broadband laser (BBL) and a narrowband laser (NBL). (b)–(f) Speckle contrast  $C$  decreases with spatial coherence of the source. The random laser effectively prevents speckle formation, behaving similarly to the LED but very differently from conventional lasers. (g) Intensity fluctuations in the images are measured by the probability density function ( $P$ ) of light intensity ( $I$ ) at each pixel of the camera, normalized by the average intensity ( $I_0$ ), of all pixels. The distribution becomes narrower as the spatial coherence reduces [45]. 43
- Fig. 2.16. Fig. 2.15. (a) Schematic of experimental set-up. Five light sources with different degrees of spatial coherence were used: a light-emitting diode (LED), a random laser (RL), an amplified spontaneous emission (ASE) source, a broadband laser (BBL) and a narrowband laser (NBL). (b)– 45

(f) Speckle contrast  $C$  decreases with spatial coherence of the source. The random laser effectively prevents speckle formation, behaving similarly to the LED but very differently from conventional lasers. (g) Intensity fluctuations in the images are measured by the probability density function ( $P$ ) of light intensity ( $I$ ) at each pixel of the camera, normalized by the average intensity ( $I_0$ ), of all pixels. The distribution becomes narrower as the spatial coherence reduces [45].

Fig. 2.17.	Number of publications on random laser in the past two decades.	46
Fig. 3.1.	Molecular structure of 1,3-butadiene.	56
Fig. 3.2	Simplified energy diagram (singlet states) of organic laser dyes.	57
Fig. 3.3.	Chromophore structure of xanthene dye.	58
Fig. 3.4.	Molecular structures of QSH, rhodamine 6G, B, 3B, 19, 640, 110, and 123.	60
Fig. 3.5.	Absorption spectrum of Rh640 perchlorate in PMMA.	62
Fig. 3.6.	Schematic diagram of process of solution polymerization.	64
Fig. 3.7.	Schematic diagram of process of bulk polymerization.	65
Fig. 3.8.	Illustration of propagating light ray incident on the boundary between two media.	71
Fig. 3.9.	Schematic diagrams of multi-mode (step-index and graded-index) and single-mode fibers.	72
Fig. 3.10.	Actual and preset temperature for polymerization of preform monomers.	79
Fig. 3.11.	Schematic diagram of a conventional laser structure.	81
Fig. 3.12.	Schematic diagram of a random laser with incoherent and non-resonant feedback.	83
Fig. 3.13.	Schematic diagram of a random laser with coherent and resonant feedback.	84
Fig. 4.1.	Schematic diagram of a conventional SEM sputter coater for gold mirror coating on fiber end-face.	100

Fig. 4.2.	Schematic diagram of sputtering system for coating gold mirror on the glass substrate.	101
Fig. 4.3.	Spectral reflectance of sputtering deposition time from 10s to 120s.	101
Fig. 4.4.	Reflectance at 623nm of gold mirror on glass substrate as a function of sputtering deposition time.	102
Fig. 4.5.	Sputtering profile for gold coating on the dye-doped fiber end.	103
Fig. 4.6.	Schematic diagram of Rh640 doped cladding polymer optical fiber.	104
Fig. 4.7.	Experimental set-up for lasing performance characterization of Rh640-dye-doped POF.	105
Fig. 4.8(a)	The fiber output power as a function of pump power for Rh640-dye-doped core POF and undoped core POF without gold mirror coated on the output coupler.	107
Fig. 4.8(b).	The fiber output power as a function of pump power for Rh640-dye-doped core POF and undoped core POF with gold mirror of 30% reflectance coated on the output coupler.	108
Fig. 4.8(c).	The fiber output power as a function of pump power for dye-doped core POF and undoped core POF with gold mirror of 40% reflectance coated on the output coupler.	109
Fig. 4.8(d).	The fiber output power as a function of pump power for dye-doped core POF and undoped core POF with gold mirror of 80% reflectance coated on the output coupler.	110
Fig. 4.8(e).	The fiber output power as a function of pump power for dye-doped core POF and undoped core POF with gold mirror of 90% reflectance coated on the output coupler.	111
Fig. 4.9.	Schematic diagram of step-index POFs with cladding doped with 200ppm Rh640 dye, and cores doped with 200ppm, 50ppm, 20ppm and 0ppm Rh640 dye (top to bottom).	115
Fig. 4.10.	Experimental set-up for lasing spectra characterization of dye-doped POF.	116

Fig. 4.11.	The output power as a function of pump power for POFs: (a) Core: undoped, Cladding: 200ppm Rh640-dye-doped, (b) Core: 20ppm Rh640-dye-doped, Cladding: 200ppm Rh640-dye-doped, (c) Core: 50ppm Rh640-dye-doped, Cladding: 200ppm Rh640-dye-doped, (d) Core: 200ppm Rh640-dye-doped, Cladding: 200ppm Rh640-dye-doped, and (e) Core: 20ppm Rh640-dye-doped, Cladding: undoped.	119
Fig. 4.12(a).	Emission spectrum of 20ppm Rh640-dye-doped core POFs with 200ppm Rh640-dye-doped cladding at a pump power of 9.5mW.	121
Fig. 4.12(b).	Emission spectrum of 20ppm Rh640-dye-doped core POFs with 200ppm Rh640-dye-doped cladding at a pump power of 16.6mW.	121
Fig. 4.12(c).	Emission spectrum of 20ppm Rh640-dye-doped core POFs with 200ppm Rh640-dye-doped cladding at a pump power of 25.9mW.	122
Fig. 4.12(d).	Emission spectrum of 20ppm Rh640-dye-doped core POFs with 200ppm Rh640-dye-doped cladding at a pump power of 35.4mW.	122
Fig. 4.12(e).	Emission spectrum of 20ppm Rh640-dye-doped core POFs with 200ppm Rh640-dye-doped cladding at a pump power of 46.2mW.	123
Fig. 4.12(f).	Emission spectrum of 20ppm Rh640-dye-doped core POFs with 200ppm Rh640-dye-doped cladding at a pump power of 57.6mW.	123
Fig. 4.12(g).	Emission spectrum of 20ppm Rh640-dye-doped core POFs with 200ppm Rh640-dye-doped cladding at a pump power of 67.8mW.	124
Fig. 4.12(h).	Emission spectrum of 20ppm Rh640-dye-doped core POFs with 200ppm Rh640-dye-doped cladding at a pump power of 80.4mW.	124
Fig. 4.13.	The emission linewidth of 20ppm Rh640-dye-doped core POF with 200ppm Rh640-dye-doped cladding as a function of pump power.	125
Fig. 4.14.	The temporal spectrum of the output pulse chain of	126

	20ppm Rh640-dye-doped core POF with 200ppm Rh640-dye-doped cladding. It is just used to demonstrate the pulse form of output.	
Fig. 4.15.	Photostability of 20ppm dye-doped core POF with 200ppm dye-doped cladding with pumping time.	127
Fig. 4.16.	Degradation of laser energy output of the GI POF laser and copolymer bulk laser with number of pulses [2].	127
Fig. 5.1.	Schematic diagram of the POF containing 800ppm (1.3mM) Rh640 dye (magenta color) and 400ppm ( $1.62 \times 10^{10} \text{ cm}^{-3}$ ) TiO <sub>2</sub> nanoparticles (white dots).	132
Fig. 5.2(a).	Emission spectrum of dye-doped POF without nanoparticles for incident pump power of 12.6mW.	134
Fig. 5.2(b).	Emission spectrum of dye-doped POF without nanoparticles for incident pump power of 16.8mW.	134
Fig. 5.2(c).	Emission spectrum of dye-doped POF without nanoparticles for incident pump power of 21.2mW.	135
Fig. 5.2(d).	Emission spectrum of dye-doped POF without nanoparticles for incident pump power of 26.4mW.	135
Fig. 5.2(e).	Emission spectrum of dye-doped POF without nanoparticles for incident pump power of 30.4mW.	136
Fig. 5.2(f).	Emission spectrum of dye-doped POF without nanoparticles for incident pump power of 35.7mW.	136
Fig. 5.2(g).	Emission spectrum of dye-doped POF without nanoparticles for incident pump power of 39.9mW.	137
Fig. 5.2(h).	Emission spectrum of dye-doped POF without nanoparticles for incident pump power of 44.2mW.	137
Fig. 5.2(i).	Emission spectrum of dye-doped POF without nanoparticles for incident pump power of 50.6mW.	138
Fig. 5.3.	Spectral linewidth of the emission in the dye-doped POF lasing spectrum with pump power.	138
Fig. 5.4(a).	Emission spectrum of POF random lasers for incident pump power of 11.0mW.	140

Fig. 5.4(b).	Emission spectrum of POF random lasers for incident pump power of 15.3mW.	141
Fig. 5.4(c).	Emission spectrum of POF random lasers for incident pump power of 21.2mW.	141
Fig. 5.4(d).	Emission spectrum of POF random lasers for incident pump power of 26.0mW.	142
Fig. 5.4(e).	Emission spectrum of POF random lasers for incident pump power of 30.2mW.	142
Fig. 5.4(f).	Emission spectrum of POF random lasers for incident pump power of 36.0mW.	143
Fig. 5.4(g).	Emission spectrum of POF random lasers for incident pump power of 39.8mW.	143
Fig. 5.4(h).	Emission spectrum of POF random lasers for incident pump power of 44.3mW.	144
Fig. 5.4(i).	Emission spectrum of POF random lasers for incident pump power of 52.2mW.	144
Fig. 5.4(j).	Emission spectrum of POF random lasers for incident pump power of 55.1mW.	145
Fig. 5.4(k).	Emission spectrum of POF random lasers for incident pump power of 61.8mW.	145
Fig. 5.4(l).	Emission spectrum of POF random lasers for incident pump power of 66.2mW.	146
Fig. 5.4(m).	Emission spectrum of POF random lasers for incident pump power of 71.9mW.	146
Fig. 5.4(n).	Emission spectrum of POF random lasers for incident pump power of 76.3mW.	147
Fig. 5.4(o).	Emission spectrum of POF random lasers for incident pump power of 81.6mW.	147
Fig. 5.5.	Spectral linewidth of the ASE in the random lasing spectrum with pump power.	151
Fig. 5.6.	Distribution of discrete lasing modes in the emission spectra with pumping power of 26.9mW, 31.2mW,	152

36.0mW, 39.8mW, and 44.3mW (bottom to top).

Fig. 6.1.	Rotating system for ensuring the uniform distribution of TiO <sub>2</sub> nanoparticles in the dye-doped core materials during the long duration (4-5 days) of the preform polymerization (curing) stage. The whole system is put in an oven during the whole polymerization process.	160
Fig. 6.2(a).	Emission spectra of 800ppm (1.3mM) Rh640 dye-doped POF with 10ppm ( $6.69 \times 10^7 \text{ cm}^{-3}$ ) of TiO <sub>2</sub> nanoparticles for pump power of 14.8mW.	162
Fig. 6.2(b).	Emission spectra of 800ppm (1.3mM) Rh640 dye-doped POF with 10ppm ( $6.69 \times 10^7 \text{ cm}^{-3}$ ) of TiO <sub>2</sub> nanoparticles for pump power of 16.5mW.	162
Fig. 6.2(c).	Emission spectra of 800ppm (1.3mM) Rh640 dye-doped POF with 10ppm ( $6.69 \times 10^7 \text{ cm}^{-3}$ ) of TiO <sub>2</sub> nanoparticles for pump power of 42.4mW.	163
Fig. 6.3(a).	Emission spectra of 800ppm (1.3mM) Rh640 dye-doped POF with 15ppm ( $1.00 \times 10^8 \text{ cm}^{-3}$ ) of TiO <sub>2</sub> nanoparticles for pump power of 12.1mW.	163
Fig. 6.3(b).	Emission spectra of 800ppm (1.3mM) Rh640 dye-doped POF with 15ppm ( $1.00 \times 10^8 \text{ cm}^{-3}$ ) of TiO <sub>2</sub> nanoparticles for pump power of 21.5mW.	164
Fig. 6.3(c).	Emission spectra of 800ppm (1.3mM) Rh640 dye-doped POF with 15ppm ( $1.00 \times 10^8 \text{ cm}^{-3}$ ) of TiO <sub>2</sub> nanoparticles for pump power of 44.8mW.	164
Fig. 6.4(a).	Emission spectra of 800ppm (1.3mM) Rh640 dye-doped POF with 20ppm ( $1.34 \times 10^8 \text{ cm}^{-3}$ ) of TiO <sub>2</sub> nanoparticles for pump power of 12.0mW.	165
Fig. 6.4(b).	Emission spectra of 800ppm (1.3mM) Rh640 dye-doped POF with 20ppm ( $1.34 \times 10^8 \text{ cm}^{-3}$ ) of TiO <sub>2</sub> nanoparticles for pump power of 19.4mW.	165
Fig. 6.4(c).	Emission spectra of 800ppm (1.3mM) Rh640 dye-doped POF with 20ppm ( $1.34 \times 10^8 \text{ cm}^{-3}$ ) of TiO <sub>2</sub> nanoparticles for pump power of 40.6mW.	166
Fig. 6.5(a).	Emission spectra of 800ppm (1.3mM) Rh640 dye-doped POF with 25ppm ( $1.67 \times 10^8 \text{ cm}^{-3}$ ) of TiO <sub>2</sub> nanoparticles for pump power of 12.6mW.	166

Fig. 6.5(b).	Emission spectra of 800ppm (1.3mM) Rh640 dye-doped POF with 25ppm ( $1.67 \times 10^8 \text{ cm}^{-3}$ ) of $\text{TiO}_2$ nanoparticles for pump power of 20.7mW.	167
Fig. 6.5(c).	Emission spectra of 800ppm (1.3mM) Rh640 dye-doped POF with 25ppm ( $1.67 \times 10^8 \text{ cm}^{-3}$ ) of $\text{TiO}_2$ nanoparticles for pump power of 40.0mW.	167
Fig. 6.6(a).	Emission spectra of 800ppm (1.3mM) Rh640 dye-doped POF with 40ppm ( $2.67 \times 10^8 \text{ cm}^{-3}$ ) of $\text{TiO}_2$ nanoparticles for pump power of 13.4mW.	168
Fig. 6.6(b).	Emission spectra of 800ppm (1.3mM) Rh640 dye-doped POF with 40ppm ( $2.67 \times 10^8 \text{ cm}^{-3}$ ) of $\text{TiO}_2$ nanoparticles for pump power of 19.7mW.	168
Fig. 6.6(c).	Emission spectra of 800ppm (1.3mM) Rh640 dye-doped POF with 40ppm ( $2.67 \times 10^8 \text{ cm}^{-3}$ ) of $\text{TiO}_2$ nanoparticles for pump power of 44.0mW.	169
Fig. 6.7(a).	Emission spectra of 800ppm (1.3mM) Rh640 dye-doped POF with 100ppm ( $6.69 \times 10^8 \text{ cm}^{-3}$ ) of $\text{TiO}_2$ nanoparticles for pump power of 12.8mW.	171
Fig. 6.7(b).	Emission spectra of 800ppm (1.3mM) Rh640 dye-doped POF with 100ppm ( $6.69 \times 10^8 \text{ cm}^{-3}$ ) of $\text{TiO}_2$ nanoparticles for pump power of 19.1mW.	172
Fig. 6.7(c).	Emission spectra of 800ppm (1.3mM) Rh640 dye-doped POF with 100ppm ( $6.69 \times 10^8 \text{ cm}^{-3}$ ) of $\text{TiO}_2$ nanoparticles for pump power of 41.7mW.	172
Fig. 6.8(a).	Emission spectra of 800ppm (1.3mM) Rh640 dye-doped POF with 600ppm ( $4.01 \times 10^9 \text{ cm}^{-3}$ ) of $\text{TiO}_2$ nanoparticles for pump power of 14.4mW.	173
Fig. 6.8(b).	Emission spectra of 800ppm (1.3mM) Rh640 dye-doped POF with 600ppm ( $4.01 \times 10^9 \text{ cm}^{-3}$ ) of $\text{TiO}_2$ nanoparticles for pump power of 20.4mW.	173
Fig. 6.8(c).	Emission spectra of 800ppm (1.3mM) Rh640 dye-doped POF with 600ppm ( $4.01 \times 10^9 \text{ cm}^{-3}$ ) of $\text{TiO}_2$ nanoparticles for pump power of 41.6mW.	174
Fig. 6.9(a).	Emission spectra of 800ppm (1.3mM) Rh640 dye-doped POF with 1000ppm ( $6.69 \times 10^9 \text{ cm}^{-3}$ ) of $\text{TiO}_2$ nanoparticles	174

	for pump power of 13.3mW.	
Fig. 6.9(b).	Emission spectra of 800ppm (1.3mM) Rh640 dye-doped POF with 1000ppm ( $6.69 \times 10^9 \text{ cm}^{-3}$ ) of $\text{TiO}_2$ nanoparticles for pump power of 20.1mW.	175
Fig. 6.9(c).	Emission spectra of 800ppm (1.3mM) Rh640 dye-doped POF with 1000ppm ( $6.69 \times 10^9 \text{ cm}^{-3}$ ) of $\text{TiO}_2$ nanoparticles for pump power of 41.9mW.	175
Fig. 6.10.	The random laser threshold as a function of the $\text{TiO}_2$ nanoparticle density. The concentration of Rh640 dye is 800ppm (1.3mM).	177
Fig. 6.11.	Schematic diagram of two-dimensional (2D) model of length $RL$ and height $L$ . A square unit of length $l$ at position $(x, y)$ is shown. The shaded area on the left hand side denotes the reflective mirror on the fiber end-face.	179
Fig. 6.12.	Numerical spectra for three different pumping energy in units of $\hbar\omega_0$ : $1 \times 10^5$ for (a), $3 \times 10^6$ for (b) and $9 \times 10^6$ for (c), for scattering mean free path $l_s = 100$ . Experimental emission spectra of POF random laser for $l_s = 1.59\text{cm}$ for three different pumping powers: 12.1mW for (d), 15.2mW for (e), and 44.8mW for (f).	184
Fig. 6.13.	Numerical spectra for three pumping energies in units of $\hbar\omega_0$ : $3 \times 10^5$ for (a), $6 \times 10^6$ for (b), and $9 \times 10^6$ for (c), for extreme value of scattering mean free path $l_s = 200$ . Experimental emission spectra of POF random laser from Chapter 5 for three different pumping powers: 15.3mW for (d), 30.2mW for (e), and 44.3mW for (f).	185
Fig. 6.14.	Numerical spectra for three pumping energies in units of $\hbar\omega_0$ : $1.5 \times 10^5$ for (a), $6 \times 10^6$ for (b), and $9 \times 10^6$ for (c), for extreme value of scattering mean free path $l_s = 1$ . Experimental emission spectra of POF random laser for $l_s = 0.24\text{cm}$ for three different pumping powers: 12.8mW for (d), 30.2mW for (e), and 43.4mW for (f). No random lasing peak is observed in the both strong scattering cases.	186

## LIST OF TABLES

Table 3.1	Quantum yields of rhodamine B, 3B, 6G, 19, 101, 110, and 123.	59
Table 3.2.	Advantages and disadvantages of the solution and bulk polymerization.	66
Table 3.3.	Definition of symbol in Equation 3.1 and 3.2.	68
Table 3.4.	(Left) Molecular structures of MMA, BzMA, and PMMA, and (Right) Values of symbols in Equation 3.2 for MMA and BzMA to calculate the refractive index of the core and cladding materials of POF in this study.	74
Table 3.5.	Summary of preform composition for core and cladding materials.	77
Table 5.1.	The spectral linewidth of the highest discrete lasing peak of each emission spectrum in Figure 5.2(d)-(h).	148
Table 5.2.	Lasing mode positions and the corresponding spectral spacing between adjacent lasing modes.	153
Table 6.1.	The particle density, scattering mean free path, and transport mean free path for the series of dye-doped POF with low concentration of TiO <sub>2</sub> nanoparticles.	158
Table 6.2.	The particle density, scattering mean free path, and transport mean free path for the series of dye-doped POF with high concentration of TiO <sub>2</sub> nanoparticles.	159

# CHAPTER 1

## Introduction

### 1.1 Background

The field of dye lasers have been developed for nearly 50 years. This is not surprising that there is still rising interest in dye lasers, especially in solid-state dye lasers, as documented by the large number of recent papers on dye lasers and their applications.

Since the first observation of stimulated emission from organic dye in solution in 1966 [1] and from solid-state dye lasers in 1967 [2], researchers focused on improving the lasing performance of solid-state dye lasers whatever the shape, by using different organic dyes with high efficiency [3], by changing the crosslinking degrees of host polymer through copolymerization with different monomers [4] or modifying the dye structure through copolymerization of organic dye with different monomers [5]. There is seldom or never a report on studying the lasing characteristics of solid-state dye lasers by structural design of gain media.

In characterizing the lasing performance of solid-state dye lasers, the optical cavities reported were formed by butting dichroic mirrors [3], highly reflective metallic mirror [4, 5, 6, 7, 8], highly reflective dielectric mirrors [9], or some bulk optics to the dye lasers, which made whole lasers bulky, complicated and expensive. There is a lack of simple and integral solid-state dye laser that the cavity reflectors are integrated into the dye lasers. Although a dye-doped thin polymer sheet with integrated cavity was reported [10]. However, to act as a practical device, it might be not suitable to integrate with a state-of-the-art fiber-optics system.

The concept of random laser, which is a new type of cavity-less laser making use of multiple scattering of light in gain medium to generate stimulated emission, was first introduced in 1966 [11]. The theory of stimulated emission from gain medium with disordered scatterers was proposed in 1968 [12]. There are two kinds of feedback: one is intensity or energy feedback which is frequency-insensitive or non-resonant; the other is field or amplitude feedback which is frequency-sensitive or resonant. Based on the feedback mechanisms, random lasers are classified into two categories: incoherent random lasers and coherent random lasers [13].

In 1994, stimulated emission of a system of separate scatterers and liquid gain

medium was experimentally observed and the effect of scatterers on the lasing action was also studied [14]. Since then random lasing in polymeric gain media were report in 1996 [15]. However, in these initial experimental studies, only a narrow and smooth peak was observed under strong amplification near the transition frequency determined by the gain medium. Discrete narrow peaks in the emission spectrum were not observed. This observation indicated that the feedback provided by the disorder-induced scattering was incoherent or non-resonant. In some cases, the random lasers that showed discrete narrow lasing peaks with focused pumping; behaved like conventional multimode lasers. It was believed that light trapping occurred within the scattering medium. Random lasing with coherent feedback in semiconductor power was first observed in 1999 [16]. Moreover, the transition between these two kinds of random lasers was demonstrated by varying the amount of scattering in the gain medium. However, recent numerical and analytical works on random lasers showed that discrete narrow lasing peaks based on interference do exist [17]. It was found that this phenomenon occurs not only in strongly scattered random lasers with localized modes, but also in diffusive and even in weakly scattering random lasers. However, the vast majority of random lasers do not operate in the localized regime; therefore the origin of the laser action in a diffusive or quasi-ballistic random laser is still unknown.

The random laser technology has opened up optical based applications, albeit the underlining physical mechanism that governs the process is still uncertain. One of the main issues is that there is not enough experimental data to ascertain the few proposed theories. Polymer random fiber laser is an excellent medium to study random lasing action, because the fabrication is relatively easy, low cost, in solid state form and large amount of samples are attainable at once. It is capable of hosting many different types of nanoparticles with different concentration because of the low processing temperature. Moreover, it provides high degree of control of mode confinement and directionality. Studying the variety of polymer random fiber lasers will enrich the understanding of the physics of the scattering and gain processes in a disorder medium.

## **1.2 Objective**

This thesis describes some aspects of practical importance regarding structural design in dye-doped POFs that are still missing. On the one hand, I show an experimental study of POFs doped with organic laser dye of different concentrations in core and/or in cladding. On the other hand, I have also carried out an experimental investigation about dye-doped POFs incorporated with different

concentration of nanoparticles, in order to characterize their emission properties through random lasing and demonstrate the first POF random laser. Both studies are very useful to construct a POF light source with integrated optical cavity and cavity-less POF random laser. Hence this project has the following specific objectives:

1. Fabrication of step-index dye-doped-cladding POF with different concentration of dyes incorporated in the fiber core and/or cladding.
2. Characterization of the fibers to investigate the improvement in the lasing performances of POFs with structural design in gain media.
3. Fabrication of solid-core dye-doped polymer random fibre lasers with different concentration of nanoparticles and dyes.
4. Characterization of the lasers to study the underlining working principles of random fibre lasers.

### **1.3 Methodology**

The research methodology adopted in this project includes the following details:

#### **A. Dye-doped POFs**

1. Fabricate PMMA-based preforms, and dye-doped POFs.

In this project, the PMMA-based preforms are fabricated using the bulk polymerization method. The cladding material is pure PMMA. To confine the light in the core, the refractive index of the core is raised by copolymerization of MMA with a high refractive index polymeric material namely BzMA. The refractive index values of the core and cladding are predicted from the chemical structure and composition using a molecular design theory. The organic laser dye adopted is Rh640, because its quantum yield is high and independent of temperature. The POFs are drawn using a home-made fiber drawing tower. The general optical attenuation or purity of the POFs made in this study is good enough to conduct experiment on dye-doped POFs and POF random lasers, because the length requirement is short.

2. Fabricate clad-doped POFs with fixed high reflectivity of back reflector, and characterize the fiber output power with different reflectivity of output coupler.

Two kinds of dye-doped-cladding POFs, one with dye-doped core and one with undoped core, are made to study the effect of transversely pumped dye-doped cladding through the imperfection of core-cladding interface on the lasing performance. Next both kinds of dye-doped-cladding POFs are coated with gold mirrors on fiber end-faces to form optical cavity. One fiber end-face is coated with fixed high reflectivity of gold mirror as back reflector; and another fiber end-face is

coated with different reflectivity and serves as output coupler. This action is to verify which configuration of optical cavity is promising for further study.

3. Fabricate clad-doped POFs with fixed high reflectivity of back reflector, and characterize the fiber output power with different dyes concentration in core.

Based on the dye-doped-cladding POF with promising optical cavity, the core of the POF is doped with different dyes concentration to provide the gain for the stimulated emission under excitation.

#### B. POF random lasers

4. Develop POF random lasers using nanoparticles as scatterers and organic laser dyes to provide optical gains, and characterize the lasing spectra.

Initially,  $\text{TiO}_2$  particle size of  $\sim 400\text{nm}$  and of extremely low density is incorporated as the scatterers in the core medium. Rh640 of  $\sim 1.3\text{mM}$  concentration is doped in the core to provide optical gain. The fabrication method of POF random lasers is the same as the method adopted for POF dye lasers. The lasing spectra are obtained by exciting the samples with a pulse laser.

5. Develop POF random lasers with different nanoparticles concentration and using organic dyes to provide gains, and characterize the lasing spectra, and study the effect of particle density on the lasing threshold pump power.

The work is divided into two main parts. Part I is to fabricate the POFs and to characterize the lasing spectra of POFs with low TiO<sub>2</sub> nanoparticle density; and the POFs are doped with organic dyes Rh640 to provide laser gain. Part II is to fabricate the POFs and to characterize the lasing spectra of POFs with high TiO<sub>2</sub> nanoparticle density; and the POFs is again doped with organic dyes Rh640 to provide laser gain. In practice, the problems encountered in the fabrication of high density scatters POFs can be very different to those of low density, because the required average particles separation is comparable to the lasing wavelength. The lasing spectra are obtained by exciting the samples with a pulse laser; and the effect of particle density on the lasing threshold of POF random lasers are also studied.

## **1.4 Outline of the thesis**

In Chapter 2, an overall literature review regarding the development of dye lasers and random lasers is presented. It starts with the introduction of solid-state dye lasers with different forms, including cylindrical rod, thin film and slab, and optical fiber. Then two different kinds of optical cavity, namely external optical cavity and

integrated optical cavity of solid-state dye lasers are discussed. Next, two kinds of random lasers and their transition are introduced. The first kind is random laser with incoherent feedback while another kind of random lasers with coherent feedback. The application and the future prospect of random lasers are reviewed comprehensively at the end of this chapter.

The background required to understand the optical characteristics of the polymer optical fibers doped with organic laser dyes is shown in Chapter 3. Details include the physical and optical properties of organic dyes, polymeric materials, polymer optical fibers as well as their fabrication methods to the resulting dye-doped polymer optical fibers are presented. Next, the mechanism of stimulated emission in which the light waves are multiply scattered and amplified in random lasers is discussed. The relevant length scales that describe the scattering process as well as its determination are illustrated. The advantages and disadvantages of random lasers are discussed finally.

In Chapter 4, the fabrication process of our dye-doped POF light source as well as the formation of optical cavity by deposition of gold mirrors on fiber end-faces are presented. Next, investigations, including the influence of the reflectivity of gold

mirror integrated on the fiber output coupler of optical cavity on the emission characteristic, and the effect of the dye concentration in the core of POF with dye-doped cladding on the emission performance of the POF light source are thoroughly discussed. Based on the results of the characterizations, a dye-doped POF of structure in which the core is slightly doped and the cladding is highly doped with organic laser dye is proposed. Finally, the emission characteristics and emission lifetime of the specially designed dye-doped POF light source are demonstrated.

The fabrication process and the experimental characterization of the spectral emission of the POF random laser are presented in Chapter 5. Measurements, including spectral evolution with excitation power are illustrated. At the end of this chapter, the lasing mode analysis of POF random laser is discussed.

The influence of scatterers concentration on the number of discrete lasing modes is comprehensively studied in Chapter 6. The investigation is divided into two parts. In part I, the POF random lasers are fabricated and their lasing spectra are characterized with low TiO<sub>2</sub> nanoparticle density. In part II, the POF random lasers are fabricated and their lasing spectra are again characterized with high TiO<sub>2</sub> nanoparticle density. Next, the influence of TiO<sub>2</sub> nanoparticle density on the

threshold pump power is illustrated, and a nanoparticle density of minimum threshold is found.

Finally, in chapter 7, all the works and achievements done in this study are summarized, and some future works in order to keep exploring in the area of POF light source and laser applications are proposed.

## 1.5 Reference

1. P. P. Sorokin and J. R. Lankard, "Stimulated emission observed from an organic dye, chloro-aluminum phthalocyanine", IBM J. Res. Develop. Vol. 10, 162 (1966)
2. B. H. Soffer and B. B. McFarland, "Continuously tunable, narrow-band organic dye lasers", Appl. Phys. Lett., Vol. 10, 266 (1967)
3. R. E. Hermes, T. H. Allik, S. Chandra, and J. A. Hutchinson, " High-efficiency pyrromethene doped solid-state dye lasers", App. Phys. Lett., Vol. 63, 877 (1993)
4. F. Amat-Guerri, A. Costela, J. M. Figuera, F. Florido, and R. Sastre, "Laser action from rhodamine 6G-doped poly (2-hydroxyethyl methacrylate ) matrice with different crosslinking degrees", Chem. Phys. Lett., Vol. 209, 352 (1993)

5. A. Costela, I. Garcia-Moreno, J. M. Figuera, F. Amat-Guerri, R. Mallavia, M. D. Santa-Maria, and R. Sastre, "Solid-state dye lasers based on modified rhodamine 6G dyes copolymerized with methacrylic monomers", *J. Appl. Phys.*, Vol. 80, 3167 (1996)
6. F. Amat-Guerri, A. Costela, J. M. Figuera, F. Florido, I. Garcia-Moreno, and R. Sastre, "Laser action from a rhodamine 640-doped copolymer of 2-hydroxyethyl methacrylate and methyl methacrylate", *Opt. Commun.*, Vol. 114, 442 (1995)
7. A. Costela, F. Florido, I. Garcia-Moreno, R. Duchowicz, F. Amat-Guerri, J. M. Figuera, and R. Sastre, "Solid-state dye lasers based on copolymers of 2-hydroxyethyl methacrylate and methyl methacrylate doped with rhodamine 6G", *Appl. Phys. B*, Vol. 60, 383 (1995)
8. A. Costela, I. García-Moreno, and C. Gómez, O. Garcia, and R. Sastre, "Laser performance of pyrromethene 567 dye in solid polymeric matrices with different cross-linking degrees", *J. Appl. Phys.*, Vol. 90, 3159 (2001)
9. K. Kuriki, T. Kobayashi, N. Imai, T. Tamura, S. Nishihara, Y. Nishizawa, A. Tagaya, Y. Koike, and Y. Okamoto, "High-efficiency organic dye-doped polymer optical fiber lasers", *Appl. Phys. Lett.*, Vol. 33, 331 (2000)
10. T. Y. Tou, S. S. Yap, O. H. Chin, and S. W. Ng, "Optimization of a Rhodamine 6G-

- doped PMMA thin-slab laser", *Opt. Mat.*, Vol. 29, 963 (2007)
11. R. V. Ambartsumyan, N. G. Basov, P. G. Kryukov, and V. S. Letokhov, "A laser with nonresonant feedback", *IEEE J. Quantum Electron.*, Vol. 2, 442 (1966)
  12. V. S. Letokhov, "Generation of light by a scattering medium with negative resonance absorption", *Sov. Phys. Jépt.*, Vol. 26, 835 (1968)
  13. H. Cao, "Lasing in random media", *Waves Random Media* 13, R1 (2003)
  14. N. M. Lawandy, R. M. Balachandran, A. S. L. Gomes, and E. Sauvain, "Laser action in strongly scattering media", *Nature*, Vol. 368, 436 (1994)
  15. R. M. Balachandran, D. P. Pacheco, and N. M. Lawandy, "Laser action in polymeric gain media containing scattering particles", *Appl. Opt.*, Vol. 35, 640 (1996)
  16. H. Cao, Y. G. Zhao, S. T. Ho, E. W. Seelig, Q. H. Wang, and R. P. H. Chang, "Random laser action in semiconductor powder", *Phys. Rev. Lett.*, Vol. 82, 2278 (1999)
  17. J. Andreasen and H. Cao, "Numerical study of amplified spontaneous emission and lasing in random media", *Phys. Rev. A*, Vol. 82, 063835 (2010)

## CHAPTER 2

### Literature Review

#### 2.1 Development of dye lasers

The observation of stimulated emission from an ethanolic solution of organic dye, namely chloro-aluminum phthalocyanine, being incorporated in a resonator and optically excited by a ruby laser, was first reported by P. P. Sorokin *et al.* in 1966 [1]. Although the dye is an organometallic compound in which the central metal atom is directly bonded to an organic ring-type molecule, the emission is originated in the organic part of the molecule. The emission wavelength was centered at 755.5nm. In the same year, F. P. Schäfer *et al.* observed intense stimulated emission in near infrared region from a photosensitizing dye, 3,3'-diethylthiatricarbocyanine iodide, dissolved in methyl and ethyl alcohol respectively [2]. The dye solution was put in a spectrophotometer cuvette with polished walls acted as resonator mirrors, and optically excited by a giant-pulse ruby laser. They obtained tunable wavelength range of more than 60nm by varying the concentration of dye and the reflectivity of resonator mirror. Their results suggested that coherent beams of light can be emitted from many other known photosensitizing dye. Subsequent studies of lasing action from organic dye solution were carried out by F. P. Schäfer *et al.* in 1966 [3],

and also performed by B. B. McFarland in 1967 [4].

Another important advance was made by B. H. Soffer *et al.* in 1967 [5]. They substituted a diffraction grating for one of the dielectric resonator mirrors to introduce wavelength dependent optical feedback. They obtained efficient spectral narrowing from 6nm using all dielectric reflectors cavity, to 0.6nm when the grating was employed, with continuous emission wavelength tuning range of 45nm.

The first demonstration of solid-state dye lasers, a solid solution of Rhodamine 6G (Rh6G) in poly(methyl methacrylate) (PMMA), by P. P. Sorokin *et al.* in 1967 [6] and by O. G. Peterson *et al.* in 1968 [7] established a new research direction in the development of nonvolatile, nonflammable, nontoxic, compact, and mechanically stable dye lasers in the following 40 years.

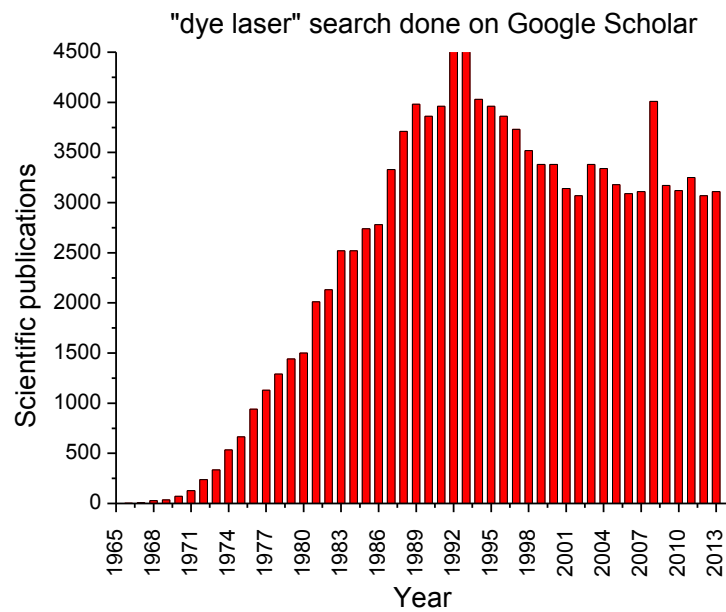


**Fig. 2.1. Number of publications on dye laser since the discovery of dye laser in**

**1966.**

Fig. 2.1 shows the number of publications on dye laser since the discovery of dye laser in liquid solution in 1966. It can be seen that the amount of research carried out on dye laser has increased dramatically both theoretically and experimentally from 1966 and to reach a maximum in 1992, and then began to drop until 2000. Then the number of publications keeps around 3000 until now. The constant number reflects that the technology of dye laser is very mature.

## **2.2 Solid-state dye lasers**

Since then, polymeric materials have been widely used as the host materials for laser dyes in the fabrication of solid-state dye lasers, owing to their features such as low manufacturing temperature, high flexibility in any shapes, low manufacturing cost, etc. Solid-state dye lasers in the form of cylindrical rods [8, 9, 10, 11, 12, 13, 14], thin films [15, 16, 17, 18, 19], thin slabs [20, 21], optical fibers [22, 23, 24], and microstructured fibers [25, 26] have been realized, and their lasing performances have been extensively investigated.

### **2.2.1 Cylindrical rod dye lasers**

In 1993, R. E. Hermes *et al.* demonstrated laser emission from pyrromethane dyes, namely Pyrromethene 567 (PM567), Pyrromethene 570 (PM570), and Pyrromethene 612 (PM612), incorporated in modified acrylic cylindrical samples [9]. The laser cavity consisted of flat dichoric mirrors separated by 2.5cm. The cylindrical sample was put into the cavity without touching the dichoric mirrors. The experiment was performed by end pumping the laser cavity at 532nm by a frequency doubled Nd:YAG laser. Slope efficiencies as high as 85%, 77%, and 52% were obtained in the sample containing PM570, PM567, and PM612 of 2.5cm cavity length. A control sample which consisted of a static ethanolic solution of PM570

was optically excited in an uncoated cuvette, and the slope efficiency was 82%. The result indicates that embedding organic dyes in solid host does not significantly affect the lasing performance. Proper resonators design and modest advance in host materials may overcome the loss in performance.

In the works reported by F. Amat-Guerri *et al.* in 1993 and 1995, and A. Costela *et al.* in 1995, 1996 and 2001 [10, 11, 12, 13], the dye-doped polymeric samples were cast in cylindrical rod of 10mm diameter and 20mm length. The laser oscillation cavity was formed by a flat aluminum mirror of 90% reflectivity and the end face of a sample rod, with a cavity length of 40mm. The samples were transversely pumped at 337nm by a N<sub>2</sub> laser with pulse width of 5ns and pulse energy of 2.4mJ. In their early works, they varied the rigidity of the polymeric matrix of poly(2-hydroxyethyl methacrylate) (PHEMA) by introducing different amounts of crosslinking monomer of ethylene glycol dimethacrylate (DEGMA) during the polymerization process. Their results showed that increasing the rigidity of polymeric matrix by decreasing the polymer free volume results in significant increases of both lasing efficiency and photostability. By combining the good dye solubility of HEMA with the high laser damage resistance of MMA, they also demonstrated high energy conversion efficiency of ~4% and long lifetime of 700 pulses at 15Hz of pumping of Rhodamine

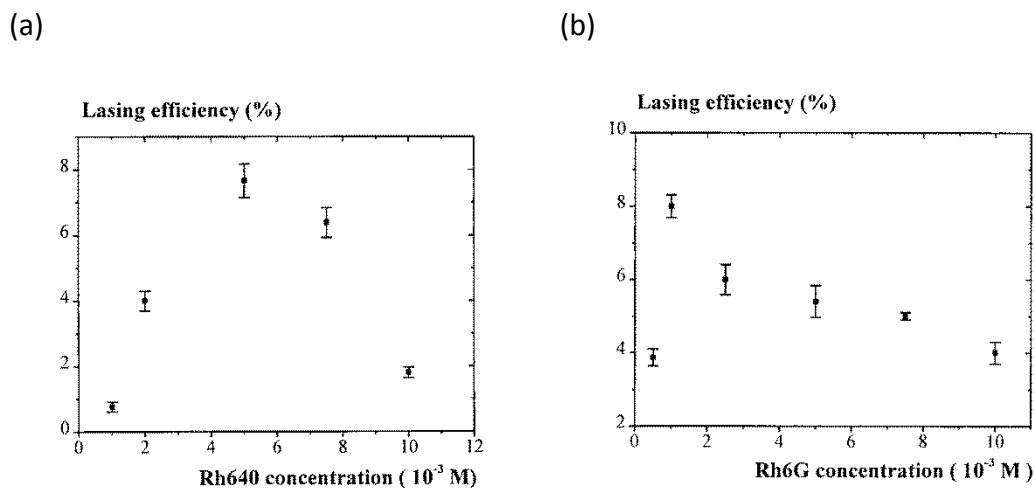
640 (Rh640) dye-doped copolymers of methyl methacrylate (MMA) and 2-hydroxyethyl methacrylate (HEMA). It seems that large local rises in temperature are the main cause of degradation of the dyes incorporated into polymeric matrices leading to short lifetime. Their further work showed that molecular modifications of organic dye facilitating the dissipation of absorbed energy that is not converted into emission could avoid early degradation.

### **2.2.2 Thin film and slab dye lasers**

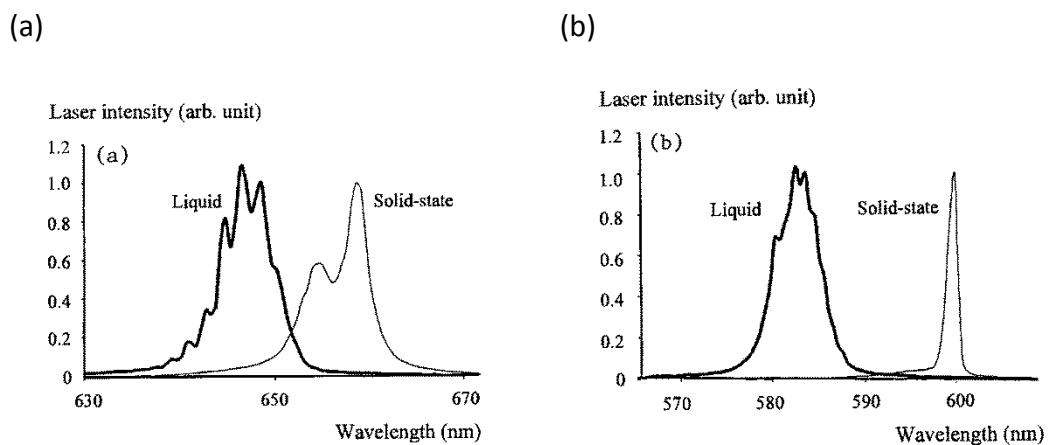
A hot-press molding technique, as an alternative to the method of radical-initiated polymerization for the fabrication of dye-doped PMMA slabs, was presented by Kwong-Cheong Yee *et al.* in 1998 [20]. In their experiments, Rh640(ClO<sub>4</sub>) and Rh6G(ClO<sub>4</sub>) doped PMMA rectangular slabs with dimensions of 4.5cm × 1.5cm × 0.5cm were fabricated. The lasing efficiency and emission spectra of this slabs were obtained by transversely pumped at 337nm by a 7ns nitrogen laser.

Fig. 2.2 shows the effects of dye concentration on the laser conversion efficiency for Rh640(ClO<sub>4</sub>) and Rh6G(ClO<sub>4</sub>) doped PMMA slabs. There is a common observation that the output efficiency initially increases with the concentration to reach a maximum value and then decreases. This is attributed to the concentration

quenching effect and aggregation of the dye molecules.



**Fig. 2.2.** Laser conversion efficiency (%) for (a) Rh640(ClO<sub>4</sub>) and (b) Rh6G(ClO<sub>4</sub>) doped PMMA slabs as a function dye concentration [20].



**Fig. 2.3.** Comparison of laser emission spectra from a dye solution and doped PMMA slab of (a) Rh640(ClO<sub>4</sub>) and (b) Rh6G(ClO<sub>4</sub>) [20].

Moreover, the lasing emission spectra, shown in Fig. 2.3, from Rh640(ClO<sub>4</sub>) and Rh6G(ClO<sub>4</sub>) doped PMMA slabs were both shifted to longer wavelengths (red shift) in comparison with their liquid-state counterparts. The emission spectrum was collapsed, and the emitted light was then re-absorbed and re-emitted inside the cavity which caused a red shift in the emission spectrum.

In 2006, K. Geetha *et al.* presented a compact solid-state laser based on leaky mode propagation in a dye-doped polymer free-standing film waveguide [19]. The free-standing film waveguide with dimensions of 4 cm × 2 cm × 50 μm was a thin sheet of PMMA doped with Rh6G. The emission spectrum from the edge of thin film waveguide indicated the existence of periodic resonant lasing modes. The optical feedback was provided by the light reflections from the lateral surfaces of the free-standing film, thus giving rise to a Fabry-Pérot-like optical cavity whose length corresponds to the film thickness. Fig. 2.4 shows the schematic diagram of their experimental set-up. The emitted light collected at the front edge was the leaky mode propagating along the narrow striped pump during the excitation.

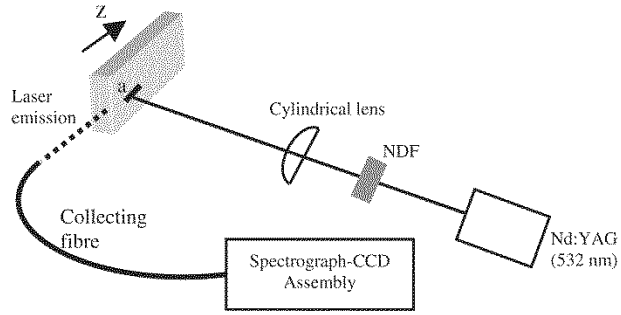


**Fig. 2.4. Schematic diagram of experimental set-up for characterization of film dye laser [19].**

Fig. 2.5 shows the emission spectra collected from the edge of Rh6G doped PMMA films when optically excited, with thickness of 50  $\mu\text{m}$  and 130  $\mu\text{m}$  respectively. Multiple narrow lasing peaks superimposed over the whole amplified spontaneous emission (ASE) were observed in both emission spectra which were attributed to the stimulated laser emission with resonant feedback. The peaks were equally spaced over the whole gain which was similar to conventional multi-mode laser. The lasing mode spacing was dependent on the film thickness. The average mode spacing was decreased from 2.3 nm to 0.9nm when the film thickness was increased from 50  $\mu\text{m}$  to 130  $\mu\text{m}$ . For Fabry-Pérot cavity, the mode spacing can be determined using the equation

$$\Delta\lambda = \frac{\lambda^2}{2nL} \quad \text{Equation 2.1}$$

, where  $\lambda$  is the wavelength of the strongest emission peak,  $n$  is the refractive index and  $L$  is the cavity length.

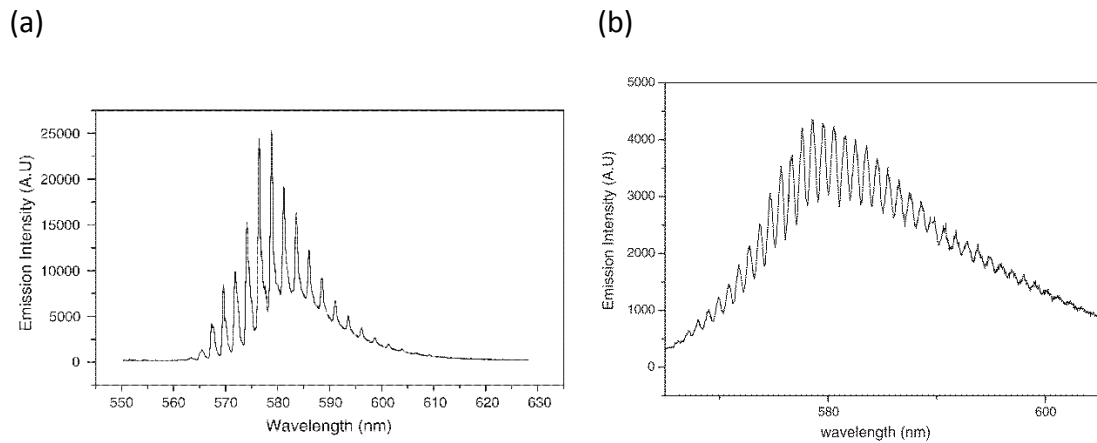


**Fig. 2.5. Emission spectra from Rh6G doped PMMA film of (a) 50  $\mu\text{m}$  and (b) 130  $\mu\text{m}$  thickness when optically excited [19].**

### 2.2.3 Optical fiber dye lasers

After the first demonstration of graded-index polymer optical fiber (GI-POF) by Yasuhiro Koike *et al.* in 1992, the group reported the lasing action from dye-doped GI-POF in 2000 [22]. The dyes used were Rhodamine B (RhB), Rhodamine 6G (Rh6G), Perylene orange (PEO), and Pyrromethene 567 (PM567), and the fibers were fabricated by copolymers of MMA and HEMA. The fibers, which have a core

diameter of 0.6mm and an outer diameter of 1mm, of 5cm length, were transversely pumped at 532nm by a frequency doubled Q-switch Nd:YAG laser. The laser resonator was formed by a dielectric mirror butted directly to one fiber end-face and another fiber end-face acted as an output coupler. Slope efficiency of 24% and lifetime of 200,000 pulses at 10Hz of pumping were achieved with a Rh6G doped GI-POF and a RhB doped GI-POF respectively. They also compared the lasing performance of a Rh6G doped GI-POF laser with a Rh6G doped bulk fiber laser. The cross sections of these fibers are shown in Fig. 2.6. The excitation method and laser resonator configuration were the same as their previous work.

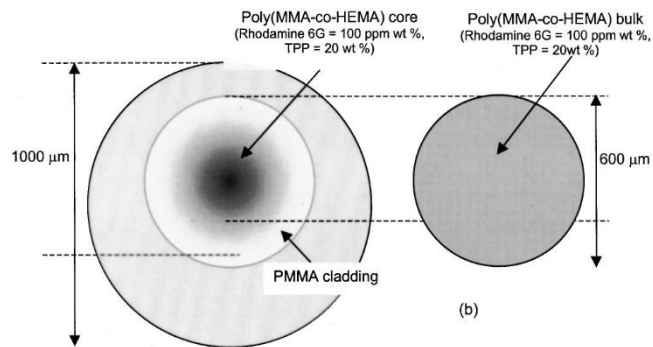


**Fig. 2.6. Cross-sectional structures of the Rh6G doped GI-POF laser and the Rh6G doped bulk fiber laser [22].**

The GI-POF laser showed both higher slope efficiency, shown in Fig. 2.7 and longer

lifetime, shown in Fig. 2.8 than the bulk fiber laser. This result might be due to the dye deactivation by oxygen of the bulk fiber laser without cladding. In other words, a cladding is necessary in preventing the reaction of the organic dye with oxygen. In view of the high slope efficiency and long lifetime, it is important to know that the high surface area-to-volume ratio of fiber geometry can effectively eliminate the thermal problem, which is a critical limiting factor in conventional solid-state dye lasers.

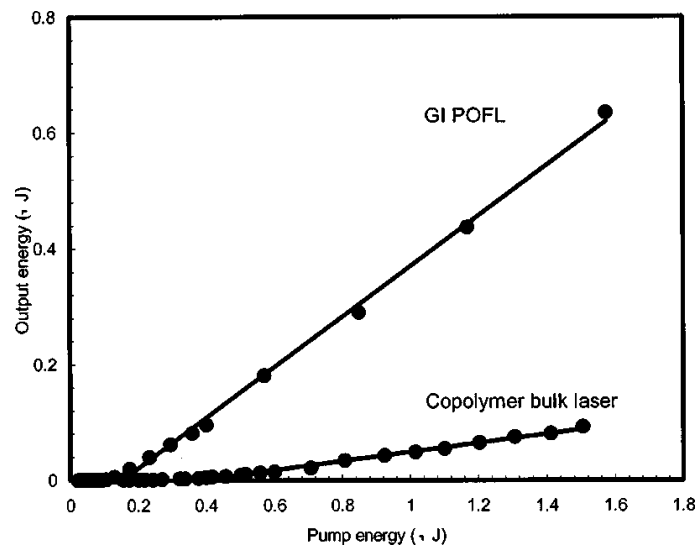


**Fig. 2.7. Lasing performances of the GI-POF laser and bulk fiber laser [22].**

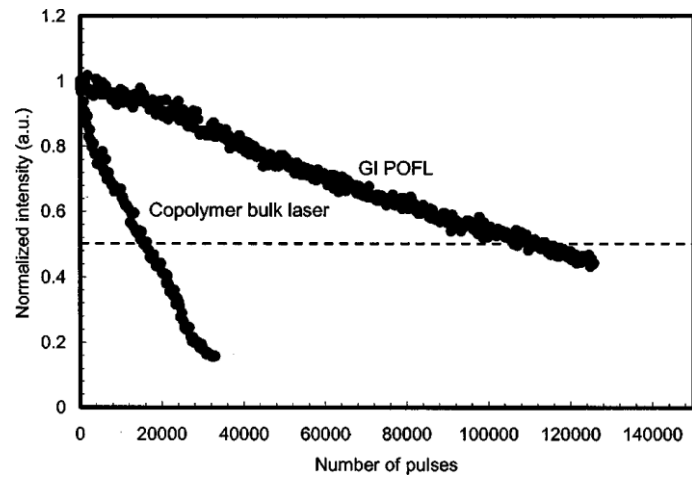


Fig. 2.8. Lifetime of the GI-POF laser and the bulk fiber laser [22].

## 2.3 Optical cavity of solid-state dye lasers

### 2.3.1 External cavity

In the developments of solid-state dye lasers or light sources, the optical cavities were formed by dichroic mirrors [9], highly reflective metallic mirror and sample end face [10, 11, 12, 13, 14], or directly butting dielectric mirror [22] to one of the sample end face and another end face as output coupler. This bulk optics made the dye-doped POF laser bulky, complicated and expensive. There is a lack of simple and integral dye-doped POF laser or light source that the cavity reflectors are integrated into the dye-doped POF laser or light source.

### 2.3.2 Integrated cavity

Literature survey reveals that there is seldom or never a report on studying the emission characteristics of a dye-doped POF by applying an integrated cavity reflectors directly to the small fiber end-face. Although other researchers had coated aluminum reflectors directly on the surfaces of a dye-doped thin polymer sheet [21]. In their work, the solid-state dye laser was in a form of thin slab of PMMA doped with Rh6G. The thin slab dye laser was fabricated by hot-press molding technique. As shown in Fig. 2.9, aluminum was coated on two surfaces of the dye-doped thin slab. The back-coated surface acted as a back reflector of the optical cavity of the dye-doped thin slab laser, while the side-coated surface as a reflector for back-scattering of dye fluorescence.

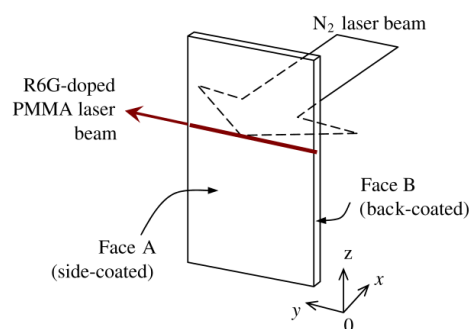


**Fig. 2.9. Aluminum coatings on the Rh6G-doped PMMA thin slab: side coating on surface A and back-coating on surface B with respect to the nitrogen laser [21].**

Figs 2.10(a)-(c) show the detailed comparisons between the lasing outputs of dye-doped thin slabs without any aluminum coating, with aluminum coated on side surface only, and with aluminum coated on both side and back surfaces, respectively. The results indicate that integrated reflectors have positive effect on the lasing performance. Fig. 2.10 also show that the laser output increases with concentration of dye, however, it significantly drops for high concentration of dye. This is attributed to the re-absorption of the emitted light by the dye molecules. Therefore, high laser output cannot be achieved by only increasing the concentration of dye in the guiding medium.

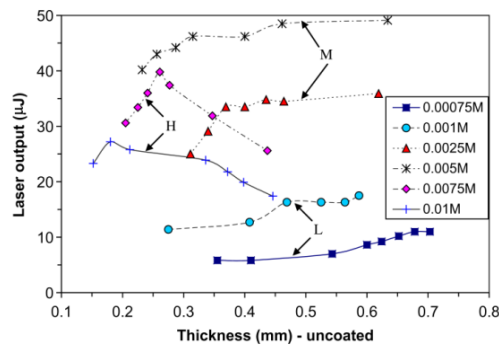


**Fig. 2.10(a). Dye laser output as a function of Rh6G-doped PMMA slab thickness**

**without aluminum coating [21].**

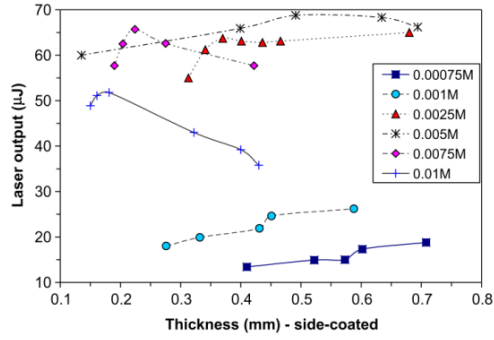


**Fig. 2.10(b). Effect of side-coated aluminum reflector on the dye laser output [21].**

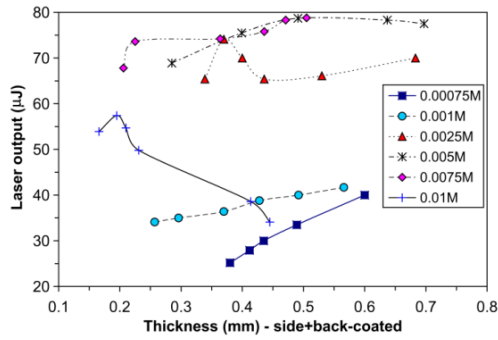


**Fig. 2.10(c). Effect of dual-coating of aluminum coatings on surfaces A and B on dye laser output [21].**

Moreover, film or slab-shaped optical device is not a convenient and suitable form in the area of telecommunication, sensing, and biomedical applications. In view of this, polymer optical fiber is a very promising candidate due to its superior light guiding ability, ease of fabrication, and low manufacturing temperature that are

very suitable for incorporation of organic laser dye.

Therefore, it is important and interesting to investigate the lasing performance of a dye-doped POF with integrated optical cavity. For this work, one fiber end-face was coated with highly reflective metallic mirror as a back reflector, and another fiber end-face was also coated with same type of metallic mirror with different reflectivity.

The dye-doped samples were prepared in the form of slab of several mm thickness, cylindrical rod, and free-standing thin film. The cylindrical rods were often prepared through bulk polymerization of dye-doped monomer solution. This was cast in a container of cylindrical shape. The dye-doped thin film was prepared by spin-coating or dip-coating dye-doped solution on a glass substrate. When the solvent was completely evaporated, the thin film was then peeled off from the glass substrate. The dye-doped slab was prepared via hot-press molding of dye-doped polymer powder in low vacuum environment to get rid of air bubbles inside the slab. However, fiber is a very promising form in the area of telecommunication and bio-medical applications. Dye-doped fiber was often fabricated from an intermediate dye-doped preform via bulk polymerization of dye-doped monomer

solution.

## 2.4 Development of random lasers

In 1966, the concept of a random laser (RL) was first introduced by Ambartsumyan *et al.* [27]. They realized a new type of laser by replacing one mirror of the Fabry-Pérot cavity with a scattering surface. In this configuration, the light suffered multiple scattering and did not return to its original position after one round trip in the gain medium. Since the paths of the light were random in the cavity, the feedback was non-resonant. The mean frequency of emission of such a laser with non-resonant feedback was therefore determined by the resonant frequency of the maximum gain in the active medium. There was only a continuous peak formed by spectrally overlap of large number of broad peaks rather than individual sharp peaks of traditional laser in the emission spectrum. The emission of such a laser was incoherent. The theory of stimulated emission from gain medium embedded with disordered scatterers was proposed by Letokhov *et al.* in 1968 [28]. They suggested that the generation of light from a disordered active medium was possible when the photon mean free path due to scattering is much smaller than the dimensions of the scattering volume but longer than the wavelength of light. In this case, the motion of photon is diffusive. They solved the diffusion equation for photon energy

density in the presence of a homogeneous gain and found that there exists a critical volume. If the volume of scattering medium exceeds the critical volume, the photon energy density increases exponentially with time. This means the generation of light diverges but this will not happen in reality because the gain is depleted quickly. Based on the coherence among multiple-scattered light waves in a gain medium, in general, there are two categories of optical feedback in RL. One is the intensity or energy feedback which is incoherent (phase insensitive) and non-resonant (frequency independent), and the other is field or amplitude feedback which is coherent (phase sensitive) and resonant (frequency dependent) [29].

#### **2.4.1 Random laser with incoherent feedback**

In 1994, Lawandy *et al.* used a system of separate scatterers and gain medium to study the effect of scatterers on lasing action of strongly scattering gain media [30]. They suspended TiO<sub>2</sub> nanoparticles in methanol containing Rh640 perchlorate dyes. The advantage of this method is that the amount of scattering can easily be varied by changing the density or concentration of the scatterers. In this configuration, remarkable narrowing both in the spectral and temporal emission spectra from the scattering gain media was observed.

Subsequent studies in spectral and temporal measurements of laser action of organic dye in strongly scattering media were performed by W. L. Sha *et al.* [31]. They demonstrated that a well-defined emission threshold occurred and depended on the concentration of the dye and the particle density. The occurrence of threshold suggested the existence of feedback in the scattering gain media. The featureless emission spectrum above the threshold revealed that the feedback was incoherent and non-resonant. The stimulated emission was enhanced significantly by increasing the amount of scattering, because the photons travelled longer distance in the gain region which led to large interaction lengths with large gain. The results indicated that multiple scattering of light in gain medium played a positive role in determining the random lasing process. Recurrent scattering of light not only increases the transport path length of light in an active medium, but also enhances light amplification by stimulated emission with feedback [32].

The term *Random Laser* was introduced by D. S. Wiersma *et al.* in 1995 [33]. They argued that the multiple scattering process of light is elastic, interference effect are present in all random laser materials. The question is whether the interference effect is observed in a specific experimental configuration. For example, some interference effects are averaged out by using long pumping pulses or by averaging

over several random lasing shots. They stated that a clear and good definition of random laser is an optical structure or material that satisfies two criteria: (1) Light is multiply scattered owing to randomness and amplified by stimulated emission. (2) There exists a threshold, due to multiple scattering, above which total gain is larger than total loss. It should be noted that this definition appears to include all disordered gain media, and there is no lower bound for the transport mean free path but the upper bound is limited by the sample size.

In most previous studies of random lasing, the host media for gain and scattering elements were in liquid state. The sedimentation of scattering elements in the liquid hosts was a common problem which caused the instability of emission in the random lasing studies. In 1996, R. M. Balachandran *et al.* used a polymer sheet as the host for the dye and scattering particles made by the cell-casting technique. Compared with liquid disordered gain media, shown in Fig. 2.11, similar results of random lasing in the polymeric disordered gain media were reported [34], which opened up a number of possible applications in the civil and military area. However, in these initial experimental studies, only a narrow and continuous peak was observed under strong amplification near the transition frequency determined by the gain medium. Discrete narrow lines in the emission spectrum were not

observed. This phenomenon indicated that the feedback provided by the disorder-induced scattering was incoherent or non-resonant.

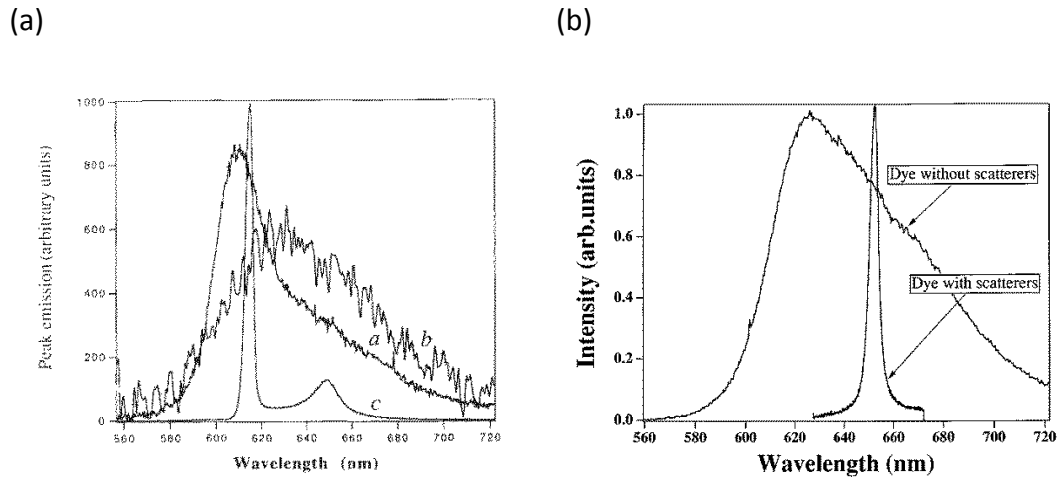


**Fig. 2.11. Random lasing emission spectra of (a) solution of Rh640 perchlorate dye in methanol containing  $\text{TiO}_2$  nanoparticles, *a* corresponds to spectrum from sample without nanoparticles at pump well above threshold, *b* and *c* corresponds to spectra from samples with nanoparticles at pump well below and well above threshold respectively, and (b) polymeric sheet containing Rh640 perchlorate dye with  $\text{TiO}_2$  nanoparticles [34].**

## 2.4.2 Random laser with coherent feedback

In some cases, the random lasers that showed discrete narrow lasing lines with focused pumping; behaved like conventional multimode lasers. It was believed that light trapping occurred within the scattering medium. In 1999, H. Cao *et al.* reported the first random lasing observation with coherent feedback semiconductor (ZnO) powder [35]. Discrete lasing modes in emission spectrum, shown in Fig. 2.12, have been observed. In the ZnO powder, the emitted light was strongly scattered due to the short scattering mean free path. In the course of recurrent multiple scattering in the powder, many closed loop paths were formed which served as ring cavities for emitted light. Since the loss in the cavities were different, once the gain in the low-loss cavities exceeded the loss, laser oscillations occurred and resulted in discrete lasing modes in the emission spectrum. When the pump power increased, the gain exceeded the loss in the more lossy cavities which resulted in more discrete lasing modes in the emission spectrum. They have also observed spatial confinement of laser lights in the same ZnO powder as shown in Fig. 2.13. Their experimental results indicated that the spatial confinement was attributed to the interference effect enhanced by coherent amplification of scattered light [36].

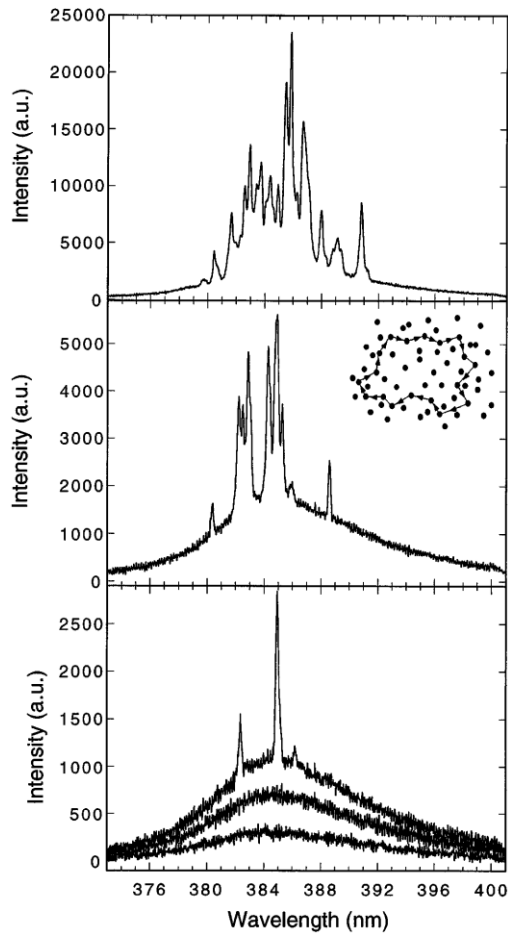


**Fig. 2.12. Emission spectra from ZnO powder when the intensity is (from bottom to top) 400, 562, 763, 875, and 1387kWcm<sup>-2</sup>. The inset in the middle graph shows the formation of closed loop path for recurrent multiple scattering of light in the powder [35].**

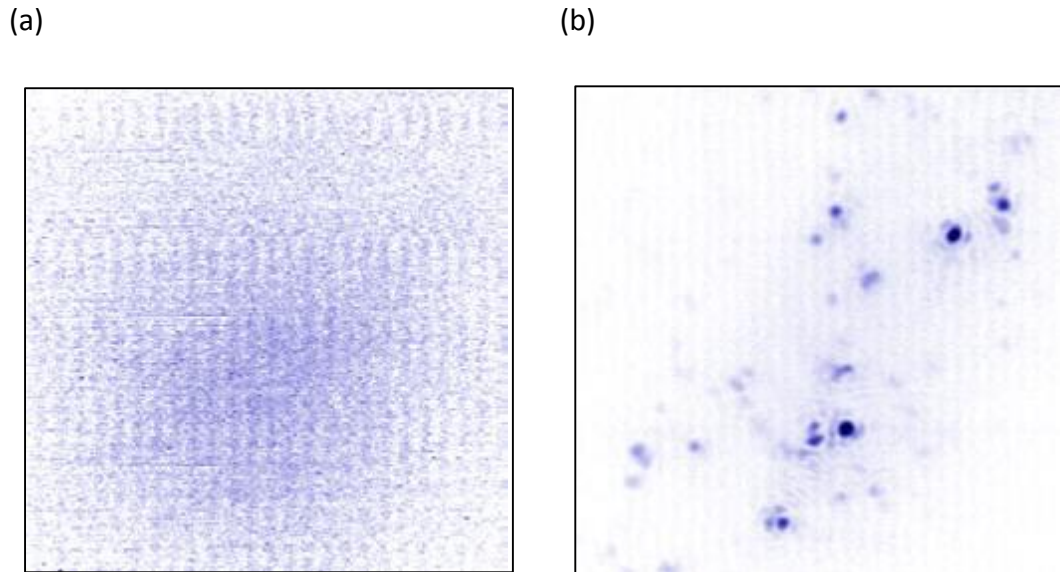


**Fig. 2.13. (a) Spatial distribution of emission intensity in ZnO powder at pump energy below threshold, and (b) above threshold [35].**

### 2.4.3 Transition between two kinds of random lasers

Moreover, Y. Ling *et al.* have experimentally studied and analytically illustrated the different lasing mechanisms between random lasers with coherent feedback and that with non-resonant feedback [37]. H. Cao *et al.* also demonstrated the difference in the transition between these two kinds of random lasers by varying the amount of scattering in the gain medium [38]. In general, scattering can be distinguished into three regimes [39]: (1) Weak scattering with gain (transport mean free path  $l_t$  is of the order of sample size  $L$  or  $l_t \sim L$ ) – the introduction of low density scatterers only diffused the ASE of the laser. (2) Modest scattering with gain

(transport mean free path is much smaller than sample size but still larger than the wavelength of light  $\lambda$ , or  $L \gg l_t \gg \lambda$ ) – the presence of scatterers not only lengthens the transport path of light, but also prolong the dwelling time of light in the active medium which resulted in strong gain narrowing. (3) Strong scattering with gain (transport mean free path is equal to or smaller than the wavelength of light or  $l_t \leq \lambda$ ) – localization and recurrent scattering of light occur forming closed loop paths which provide coherent and resonant feedback in the random laser.

Experimentally, discrete narrow lasing lines based on interference of scattered lights occurs in the emission spectrum for random lasers with coherent (resonant) feedback, whereas there is only a continuous narrow peak in the emission spectrum for random lasers with incoherent (non-resonant) feedback. However, recent numerical and analytical works on random lasers by J. Andreasen *et al.* [40] showed that discrete narrow lasing lines based on interference of scattered light do exist. It was found that this phenomenon occurs not only in strongly scattered random lasers with localized modes, but also in diffusive and even in weakly scattering random lasers [41, 42]. However, the vast majority of random lasers do not operate in the localized regime; therefore the origin of the laser action in a diffusive or quasi-ballistic random laser is still unknown.

## **2.5 Applications of random lasers**

### **2.5.1 Medical diagnostics**

Because the random lasing characteristics are strongly related to the structural properties of the disordered media, the random lasing technology could be used as a diagnostic tool in structural imaging. An application in medical diagnostics for random lasers was proposed by R. C. Polson *et al.* in 2004 [43]. When human tissues as scattering media were infiltrated with laser dye solution, random lasing was induced in the tissues by optical excitation. The results, shown in Fig. 2.14, illustrated that cancerous tissue could be distinguished from healthy tissue as their random lasing emission spectra were completely different.

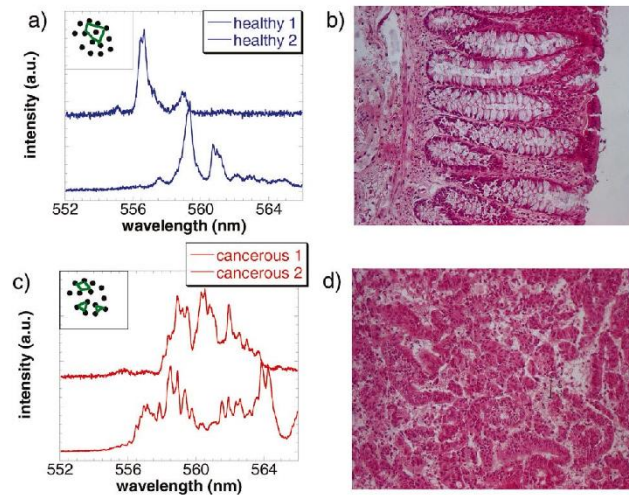


**Fig. 2.14. Random lasing emission spectra of human colon tissues infiltrated with a concentrated laser dye, namely R6G. (a) Two typical random lasing emission spectra from a healthy tissue, of which microscopic image is shown in (b). The narrow spectral lines are in fact coherent laser emission modes. The inset shows schematically closed random resonators formed due to scatterers in the gain medium. (c) and (d), same as in (a) and (b), respectively, but for a malignant colon tissue. There are more lines in the laser emission spectra in (c) that are due to more resonators in the tumor; these are caused by the excess disorder that is apparent in (d) [43].**

### **2.5.2 Speckle-free full-field imaging**

Another possible application using the random lasing characteristic of spatial coherence is that the low spatial coherence of specifically designed random lasers can be used in speckle-free full-field imaging in the setting of intense optical scattering [44, 45]. They performed a series of experiments to characterize the spatial coherence of different light sources on imaging. These light sources illuminated a scattering film and imaged the transmitted signal onto a CCD camera. Obj, S, OP, and IP represent the microscope objective, scattering film, object plane, and image plane, respectively. As shown in Fig. 2.15, the speckle in the taken images was clearly seen when using ASE source, broadband laser, and narrowband laser, but Light-emitting diode (LED) and random laser exhibit speckle-free images.

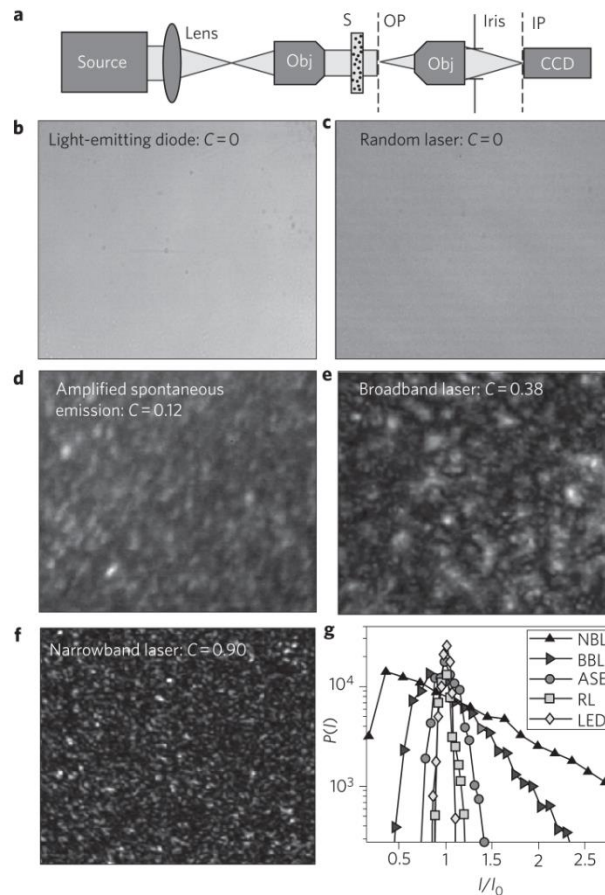


**Fig. 2.15. (a) Schematic of experimental set-up. Five light sources with different degrees of spatial coherence were used: a light-emitting diode (LED), a random laser (RL), an amplified spontaneous emission (ASE) source, a broadband laser (BBL) and a narrowband laser (NBL). (b)–(f) Speckle contrast  $C$  decreases with spatial coherence of the source. The random laser effectively prevents speckle formation, behaving similarly to the LED but very differently from conventional lasers. (g) Intensity fluctuations in the images are measured by the probability density function ( $P$ ) of light intensity ( $I$ ) at each pixel of the camera, normalized by the average intensity ( $I_0$ ), of all pixels. The distribution becomes narrower as the spatial coherence reduces [45].**

Another experimental result from [45] shown in Fig. 2.16 shows that the images, generated with random laser illumination, exhibit superior quality than images generated with spatially coherent illumination generated from conventional light sources, namely, ASE source, broadband laser, and narrowband laser. By providing intense laser illumination without the drawback of coherent artefacts, random lasers are well suited for a host of full-field imaging applications from full-field microscopy to miniature digital light projector systems to medical imaging. For example, for full-field optical coherence tomography, using thermal light sources or LEDs is not an option because low spatial coherent and high intensities are required to probe deeper into the tissue. This provides random lasers with a unique opportunity.

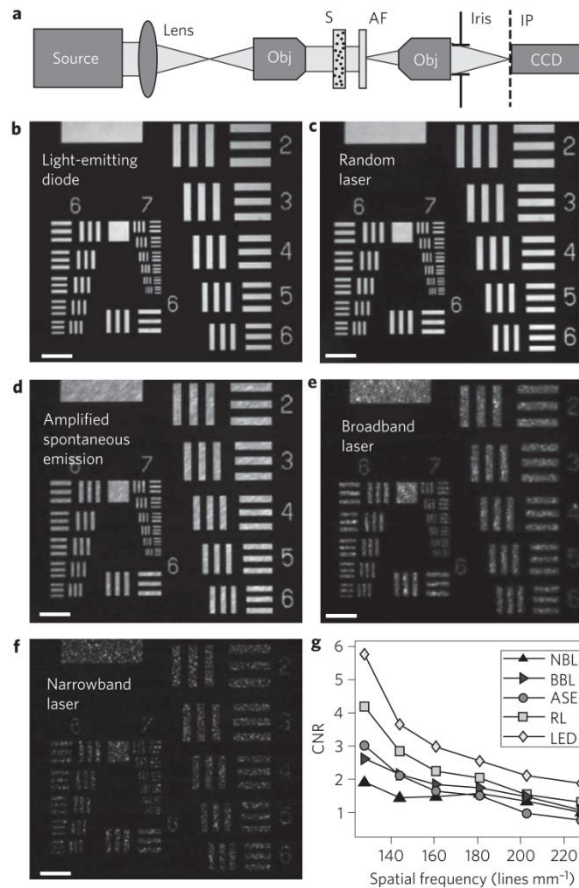


**Fig. 2.16. (a) Schematic of the experimental set-up. Five light sources, described in Fig. 2.15, were used to image an AF resolution test chart. (b)–(f) Images taken with the five sources showing that the spatially coherent sources, particularly the narrowband laser and the broadband laser, produce speckles in the bright area of the image (transparent bars in the test chart). The background of the image, which corresponds to the opaque area on the object, remains dark. (g) As a quantitative measure of image degradation by the speckle, the contrast-to-noise Ratio (CNR) was extracted from the images and plotted as a function of the spatial frequency of the features on the test chart. This confirms that the random laser produces superior images to conventional lasers and the ASE source [45].**

## 2.6 The future of random lasers

Figure 2.17 shows the number of publications on random laser in the past two decades. It can be seen in recent years that the amount of research carried out on random laser has increased dramatically both theoretically and experimentally. Researchers are starting to look at different methods and scattering media to induce random lasing, for examples, bone-tissues random laser [46] and cold-atom random laser [47] have been demonstrated.

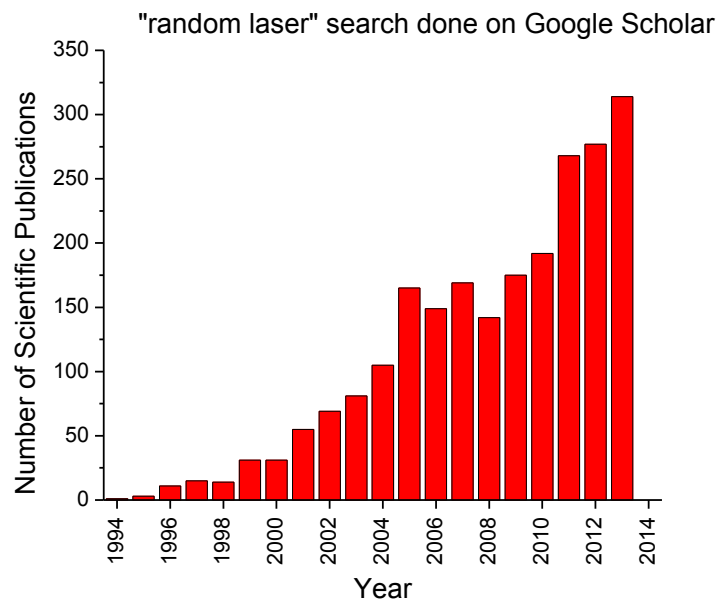


**Fig. 2.17.** Number of publications on random laser in the past two decades.

However, the amount of research done on random fibre laser is still relatively small. In 1997, the first random fibre laser was demonstrated by filling a hollow core microstructured fibre with Rh640 solution [48] (improved result reported in 2012 [49]). Since then only a few fibre-related random lasers have been reported. The most recent random fibre lasers utilized the Raman-Rayleigh scattering [50] and Brillouin scattering [51] properties of ultralong (25 to 100 km) telecommunication fibres. These random fibre lasers are state-of-the-art, because the scatterers are in fixed stable positions inside a solid fibre. However, to act as a practical device, they might be too long with a large footprint.

## 2.7 Reference

1. P. P. Sorokin and J. R. Lankard, "Stimulated emission observed from an organic dye, chloro-aluminum phthalocyanine", IBM J. Res. Develop. Vol. 10, 162 (1966)
2. F. P. Schäfer, "Principles of dye laser operation", Top. Appl. Phys. Vol. 1, 1-85, (1977).
3. F. P. Schäfer, W. Schmidt, and J. Volze, "Organic dye solution laser", Appl. Phys. Lett., Vol. 9, 306 (1966)
4. B. B. McFarland, "Laser second-harmonic-induced stimulated emission of

- organic dyes”, *Appl. Phys. Lett.* Vol. 10, 208 (1967)
5. B. H. Soffer and B. B. McFarland, “Continuously tunable, narrow-band organic dye lasers”, *Appl. Phys. Lett.*, Vol. 10, 266 (1967)
  6. P. P. Sorokin, W. H. Culver, E. C. Hammond, and J. R. Lankard, “End pumped stimulated emission from a Thiocarbocyanine dye”, *IBM J. Rev. Develop.*, Vol. 10, 401 (1966)
  7. O. G. Peterson and B. B. Snavely, “Stimulated emission from flashlamp excited organic dyes in polymethyl methacrylate”, *Appl. Phys. Lett.*, Vol.12, 238 (1968)
  8. M. L. Spaeth and D. P. Bortfeld, “Stimulated emission from polymethine dyes”, *Appl. Phys. Lett.*, Vol 9, 179 (1966)
  9. R. E. Hermes, T. H. Allik, S. Chandra, and J. A. Hutchinson, “ High-efficiency pyrromethene doped solid-state dye lasers”, *App. Phys. Lett.*, Vol. 63, 877 (1993)
  10. F. Amat-Guerri, A. Costela, J. M. Figuera, F. Florido, and R. Sastre, “Laser action from rhodamine 6G-doped poly (2-hydroxyethyl methacrylate ) matrice with different crosslinking degrees”, *Chem. Phys. Lett.*, Vol. 209, 352 (1993)
  11. F. Amat-Guerri, A. Costela, J. M. Figuera, F. Florido, I. Garcia-Moreno, and R. Sastre, “Laser action from a rhodamine 640-doped copolymer of 2-hydroxyethyl methacrylate and methyl methacrylate”, *Opt. Commun.*, Vol.

114, 442 (1995)

12. A. Costela, F. Florido, I. Garcia-Moreno, R. Duchowicz, F. Amat-Guerri, J. M. Figuera, and R. Sastre, "Solid-state dye lasers based on copolymers of 2-hydroxyethyl methacrylate and methyl methacrylate doped with rhodamine 6G", *Appl. Phys. B*, Vol. 60, 383 (1995)
13. A. Costela, I. Garcia-Moreno, J. M. Figuera, F. Amat-Guerri, R. Mallavia, M. D. Santa-Maria, and R. Sastre, "Solid-state dye lasers based on modified rhodamine 6G dyes copolymerized with methacrylic monomers", *J. Appl. Phys.*, Vol. 80, 3167 (1996)
14. A. Costela, I. García-Moreno, and C. Gómez, O. Garcia, and R. Sastre, "Laser performance of pyrromethene 567 dye in solid polymeric matrices with different cross-linking degrees", *J. Appl. Phys.*, Vol. 90, 3159 (2001)
15. V. Deshpande and E. B. Namdas, "Lasing action of rhodamine B in polyacrylic acid films", *Appl. Phys. B*, Vol. 64, 419 (1997)
16. S. S. Yap, T. Y. Tou, and S. W. Ng, "Laser emissions from disodium fluorescence-doped poly(vinyl alcohol) films," *Jpn. J. Appl. Phys.* Vol. 39, 5855 (2000)
17. S. S. Yap, W. O. Siew, T. Y. Tou, and S. W. Ng, "Red-Green-Blue Laser Emissions from Dye-Doped Poly(Vinyl Alcohol) Films", *Appl. Opt.*, Vol. 41, 1725 (2002)

18. K. Geetha, M. Rajesh, V. P. N. Nampoory, C. P. G. Vallabhan, and P. Radhakrishnan, "Loss characterization in rhodamine 6G doped polymer film waveguide by side illumination fluorescence", *J. Opt. A: Pure Appl. Opt.* Vol. 6, 379 (2004)
19. K. Geetha, M. Rajesh, V. P. N. Nampoory, C. P. G. Vallabhan, and P. Radhakrishnan, "Laser emission from transversely pumped dye-doped free-standing polymer film," *J. Opt. A: Pure Appl. Opt.*, Vol. 8, 189 (2006)
20. K. C. Yee, T. Y. Tou, and S. W. Ng, "Hot-Press Molded Poly(Methyl Methacrylate) Matrix for Solid-State Dye Lasers," *Appl. Opt.*, Vol. 37, 6381 (1998)
21. T. Y. Tou, S. S. Yap, O. H. Chin, and S. W. Ng, "Optimization of a Rhodamine 6G-doped PMMA thin-slab laser", *Opt. Mat.*, Vol. 29, 963 (2007)
22. K. Kuriki, T. Kobayashi, N. Imai, T. Tamura, Y. Koike, and Y. Okamoto, "Organic dye-doped polymer optical fiber laser", *Polym. Adv. Technol.*, Vol. 11, 612 (2000)
23. K. Kuriki, T. Kobayashi, N. Imai, T. Tamura, S. Nishihara, Y. Nishizawa, A. Tagaya, Y. Koike, and Y. Okamoto, "High-efficiency organic dye-doped polymer optical fiber lasers", *Appl. Phys. Lett.*, Vol. 33, 331 (2000)
24. M. Sheeba, K. J. Thomas, M. Rajesh, V. P. N. Nampoory, C. P. G. Vallabhan, and P. Radhakrishnan, "Multimode laser emission from dye doped polymer optical

- fiber”, *Appl. Opt.*, Vol. 44, 8089 (2007)
25. A. Argyros, M. A. van Eijkelenborg, S. D. Jackson, and R. P. Mildren, “Microstructured polymer fiber laser. *Opt. Lett.*, Vol. 29, 1882 (2004)
  26. A. Argyros, M. A. van Eijkelenborg, S. D. Jackson, and R. P. Mildren, “Reply to comment on "Microstructured polymer fiber laser", *Optics Letters*, Vol. 30, 1829 (2005)
  27. R. V. Ambartsumyan, N. G. Basov, P. G. Kryukov, and V. S. Letokhov, “A laser with nonresonant feedback”, *IEEE J. Quantum Electron.*, Vol. 2, 442 (1966)
  28. V. S. Letokhov, “Generation of light by a scattering medium with negative resonance absorption”, *Sov. Phys. Jépt.*, Vol. 26, 835 (1968)
  29. H. Cao, “Lasing in random media”, *Waves Random Media* 13, R1 (2003)
  30. N. M. Lawandy, R. M. Balachandran, A. S. L. Gomes, and E. Sauvain, “Laser action in strongly scattering media”, *Nature*, Vol. 368, 436 (1994)
  31. W. L. Sha, C. –H. Liu, and R. R. Alfano, “Spectral and temporal measurements of laser action of Rhodamine 640 dye in strongly scattering media”, *Opt Lett.*, Vol. 19, 1922 (1994).
  32. R. M. Balachandran and N. M. Lawandy, “Interface reflection effects in photonic paint”, *Opt. Lett.*, Vol. 20, 1271 (1995)
  33. D. S. Wiersma, M. P. van Albada, and Ad Lagendijk, “Random laser?”, *Nature*,

Vol. 373, 203 (1995)

34. R. M. Balachandran, D. P. Pacheco, and N. M. Lawandy, "Laser action in polymeric gain media containing scattering particles", *Appl. Opt.*, Vol. 35, 640 (1996)
35. H. Cao, Y. G. Zhao, S. T. Ho, E. W. Seelig, Q. H. Wang, and R. P. H. Chang, "Random laser action in semiconductor powder", *Phys. Rev. Lett.*, Vol. 82, 2278 (1999)
36. H. Cao, J. Y. Xu, and D. Z. Zhang, "Spatial Confinement of Laser Light in Active Random Media", *Phys. Rev. Lett.*, Vol. 84, 5584 (2000)
37. Y. Ling, H. Cao, A. L. Burin, M. A. Ratner, X. Liu, and R. P. H. Chang, "Investigation of random lasers with resonant feedback", *Phys. Rev. A.*, Vol. 64, 063808 (2001)
38. H. Cao, J. Y. Xu, S. H. Chang, and S. T. Ho, "Transition from amplified spontaneous emission to laser action in strongly scattering media", *Phys. Rev. E.*, Vol. 61, 1985 (2000)
39. D. S. Wiersma and Ad Lagendijk, "Interference effects in multiple-light scattering with gain", *Phys. A*, Vol. 241, 82 (1997)
40. J. Andreasen and H. Cao, "Numerical study of amplified spontaneous emission and lasing in random media", *Phys. Rev. A*, Vol. 82, 063835 (2010)

41. X. Wu, W. Fang, A. Yamilov, A. A. Chabanov, A. A. Asatryan, L. C. Botten, and H. Cao, "Random lasing in weakly scattering systems", *Phys. Rev.*, Vol. 74, 053812 (2006)
42. X. Wu and H. Cao, "Statistical studies of random-lasing modes and amplified spontaneous-emission spikes in weakly scattering systems", *Phys. Rev.*, Vol. 77, 013832 (2008)
43. R. C. Polson and Z. Vardeny, "Random lasing in human tissues", *Appl. Phys. Lett.*, Vol. 85, 1289 (2004)
44. B. Redding, M. A. Choma, and H. Cao, "Spatial coherence of random laser emission", *Opt. Lett.*, Vol. 36, 3404 (2011)
45. B. Redding, M. A. Choma, and H. Cao, "Speckle-free laser imaging using random laser illumination", *Nature Photon.*, Vol. 6, 355 (2012)
46. Q. Song, S. Xiao, Z. Xu, J. Liu, X. Sun, V. Drachev, V. M. Shalaev, O. Akkus, and Y. L. Kim, "Random lasing in bone tissues," *Opt. Lett.*, Vol. 35, 1425 (2010)
47. Q. Baudouin, N. Mercadier, V. Guarrera, W. Guerin, and R. Kaiser, "A cold-atom random laser," *Nature Phys.*, Vol. 9, 357 (2013)
48. C. J. S. de Matos, L. de S. Menezes, A. M. Brito-Silva, M. A. M. Gamez, A. S. L. Gomes, and C. B. de Araujo, "Random fiber laser," *Phys. Rev. Lett.*, Vol. 99, 153903 (2007)

49. Z. Hu, H. Zheng, L. Wang, X. Tian, T. Wang, Q. Zhang, G. Zou, Y. Chen, and Q. Zhang, "Random fiber laser of POSS solution-filled hollow optical fiber by end pumping," *Opt. Comm.*, Vol. 285, 3967 (2012)
50. S. K. Turitsyn, S. A. Babin, A. E. El-Tacher, P. Harper, D. V. Churkin, S. I. Kablukov, J. D. Ania-Castanon, V. Karalekas, and E. V. Podivilov, "Random distributed feedback fibre laser," *Nature Photon.*, Vol. 4, 231 (2010)
51. M. Pang, X. Bao, and L. Chen, "Observation of narrow linewidth spikes in the coherent Brillouin random fiber laser," *Opt. Lett.* Vol. 38, 1866 (2013)

## **CHAPTER 3**

# **POF Dye Lasers and Random Lasers: Materials and Structures**

### **3.1 Organic laser dyes**

Amplifying medium is an essential constituent of a laser. For dye lasers, the amplifying medium can be a liquid or solid solution of organic laser dye. For the solid solution of organic laser dye, the dye can be dissolved in the liquid monomer of a polymeric material, and then solidified through polymerization. The polymerization techniques will be discussed later in this chapter. Compared to gases lasing media, organic laser dyes exhibit a much wider absorption band in the near-ultraviolet, visible, or near-infrared region of the electromagnetic spectrum. This property is mainly determined by the structure of organic laser dyes.

#### **3.1.1 Structure and properties of organic laser dyes**

Only organic compounds, which contain an extended system of conjugated bonds, i.e. alternating single and double bonds, have the wide absorption property [1]. Fig. 3.1 shows a typical example of conjugated double bonds in the molecule of 1,3-butadiene.

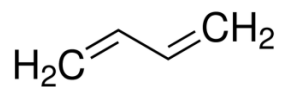


**Fig. 3.1. Molecular structure of 1,3-butadiene.**

### **3.1.2 Light absorption and emission of organic laser dyes**

The wide absorption band of laser dyes is attributed to the transition from electronic ground state  $S_0$  to the first excited singlet state  $S_1$ , shown in Fig. 3.2. The radiative transition from  $S_1$  to  $S_0$  is responsible for the spontaneous emission known as fluorescence and for the stimulated emission in dye lasers. This radiative transition has a lifetime on the order of nanoseconds [2].

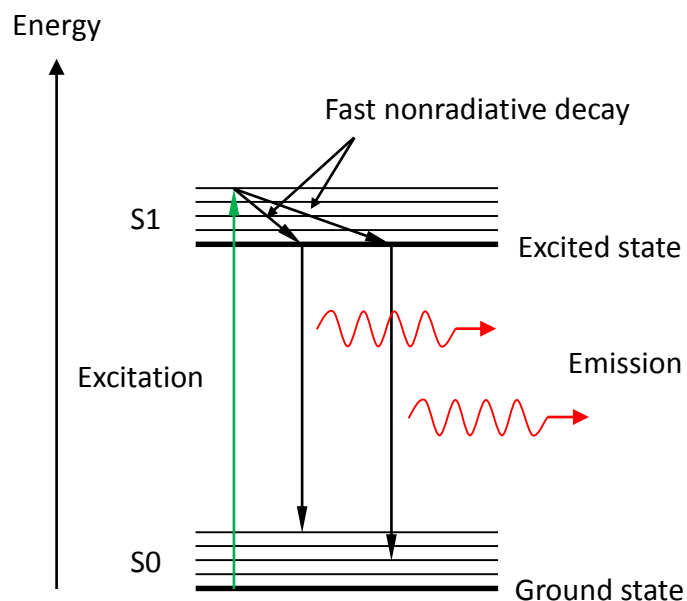


**Fig. 3.2. Simplified energy level diagram (singlet states) of organic laser dyes.**

When the dye in the laser is excited by an intense light source such as flashlamp or laser, the dye molecules are excited to some higher energy levels in the singlet manifold, and then they relax within picoseconds to the lowest excited level of S1. However, there are many non-radiative processes that compete effectively with the light emission process and thus reduce the fluorescence efficiency. The non-radiative decay of the lowest excited singlet state S1 directly to the ground state S0 is mostly responsible for the loss of fluorescence efficiency in organic dyes. The rate of the non-radiative decay is influenced by the molecular structure of the

dye and the properties of the solvent. It has been known for a long time that a rigid, planar molecular structure favors high fluorescence efficiency.

### 3.1.3 Xanthene dyes

Most efficient organic laser dyes used today belong to the class of xanthene dyes [2]. The chromophore of the xanthene dyes is illustrated in Fig. 3.3. The conjugated chromophore is responsible for the emission color of the dye. The main absorption at long wavelengths is oriented parallel to the long axis of the molecule whereas the absorption at shorter wavelength is oriented perpendicular to the long axis. Besides, their emission wavelengths cover the visible range from 500nm to 700nm.

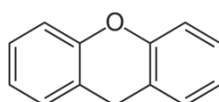


**Fig. 3.3. Chromophore structure of xanthene dye.**

They are soluble in water, but also tend to form dimers and aggregates in water which affects the resulting absorption spectrum. The dimers usually have absorption band at shorter wavelengths than the monomers and often have an additional weaker absorption band at the long-wavelength side of monomer band.

Moreover, they are only weakly fluorescent. The equilibrium between monomers and dimers is determined by the concentration and temperature of dye.

Table 3.1 shows the fluorescence quantum yields of rhodamine B, 3B, 6G, 19, 101, 110, and 123 at 25°C measured in [3]. Quinine sulfate dihydrate (QSH) in 1.0N H<sub>2</sub>SO<sub>4</sub> was used as the reference standard in the measurement. Derivatives like rhodamine 6G, 19, and 101 give high fluorescence quantum yields. However, there is a great difference in quantum yield between some common dyes such as rhodamine 101 ( $\Phi = 0.96$ ) and B ( $\Phi = 0.65$ ), which is attributed to the non-radiative decay caused by structural mobility of dye or the cavity loss due to absorption of fluorescence from monomers by the dimerization of dye. It has been known that the aggregation of dyes in aqueous solution can be prevented by addition of organic solvents. Their molecular structures are illustrated in Fig. 3.4.

**Table 3.1. Quantum yields of rhodamine B, 3B, 6G, 19, 101, 110, and 123.**

Quantum yields at 25°C					
Compound	(mol/l) $c (\times 10^{-7})$	$\lambda_E$ (nm)	$\lambda_F$ peak (nm)	$\Phi_F$	Remarks
QSH	9.24	350	458	0.55	Standard
Rhodamine 6G	1.05	248–528	558	0.95	
Rhodamine B	1.58	259–542	568	0.65	Basic EtOH
Rhodamine 3B	2.48	257–556	580	0.45	
Rhodamine 19	1.47	245–516	544	0.95	Basic EtOH
Rhodamine 101	1.34	265–563	588	0.96	Basic EtOH
Rhodamine 110	1.85	267–501	524	0.92	Basic EtOH
Rhodamine 123	1.76	245–510	534	0.90	

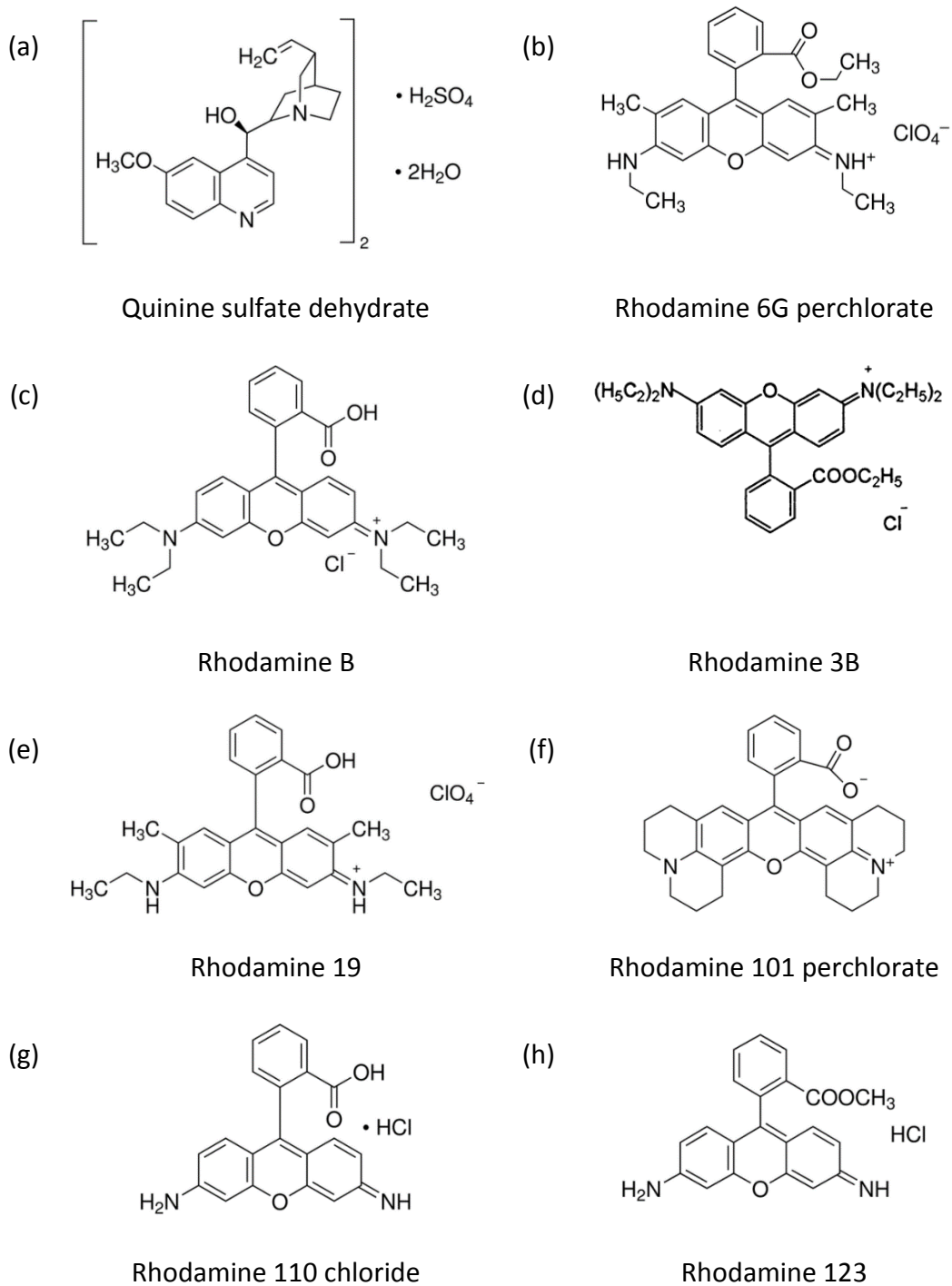
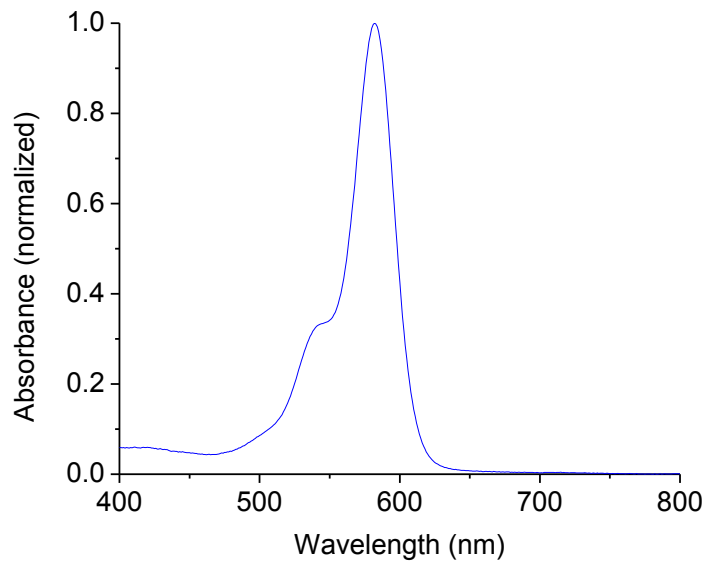


Fig. 3.4. Molecular structures of QSH, rhodamine 6G, B, 3B, 19, 640, 110, and 123.

For example, in rhodamine dyes such as rhodamine B, the temperature-dependent mobility of the diethylamino group, as shown in Fig. 3.4(c), affects the fluorescence efficiency. However, these groups are very rigid in rhodamine 101 (also known as rhodamine 640, and this name is used throughout in this thesis) and their quantum yield of fluorescence, independent of temperature and solvent, is very close to 1 [3].

Due to the high quantum yield, the organic laser dye chosen for all of our works is rhodamine 640 (Rh640) perchlorate (Exciton) mentioned in foregoing discussion. The appearance of Rh640 perchlorate is dark green crystals with brown sheen. The molecular weight is 591.05. The chemical formula is  $C_{32}H_{31}N_2O_3 \cdot ClO_4$ . The molecular structure of Rh640 perchlorate is shown in Fig. 3.4(f). The absorption spectrum of the Rh640 perchlorate in poly(methyl methacrylate) (PMMA) was obtained by cutting a 1mm thick disc slice from a 200ppm Rh640 dye-doped polymer preform (the fabrication process of the polymeric preform will be discussed in section 3.4), and was measured by using a UV-Vis spectrophotometer (Varian, Cary 300). The absorption spectrum of the Rh640 doped preform disc is shown in Fig. 3.5.



**Fig. 3.5. Absorption spectrum of Rh640 perchlorate in PMMA.**

The main absorption peaks are at the wavelengths of 532nm and 575nm. It is therefore as a convenience, the second harmonic output (532nm) of Nd:YAG laser is used as the pumping light source in all experiments of our research study.

### **3.2 Polymeric materials**

Since the development of solid-state dye lasers, polymeric materials have been used as solid host media for organic laser dyes. Compared to inorganic glasses, organic laser dyes show better solubility and compatibility with polymeric materials. Moreover, polymeric host media have the advantages of ease of fabrication due to

low processing temperature, low manufacturing cost suitable for mass production, availability of miniaturization and flexibility of shape design, etc. A great majority of polymeric host media for solid-state dye lasers are poly(methyl methacrylate) (PMMA) or methyl methacrylate (MMA) based co-polymer.

PMMA plays a very important role in polymer optical materials since it is transparent in the visible region of the electromagnetic spectrum. Chemically, it is a synthetic polymer of MMA monomers. Polymerization is a process of combining monomer molecules together in a chemical reaction to form polymer chains.

### **3.2.1 Polymerization techniques**

There are four free-radical polymerization methods, namely solution, bulk, suspension, and emulsion polymerizations. The first two techniques are used to produce single-phase or homogeneous polymers, whereas the last two are used to synthesize multi-phase or heterogeneous polymers.

#### **3.2.1.1 Solution polymerization**

Solution polymerization is a process that is used to produce polymers by dissolving a monomer and a catalyst in a non-reactive solvent. Fig. 3.6 describes the process in

solution polymerization. During polymerization process, the heat released by the chemical reaction is absorbed by the solvent which limits the overall reaction rate. The solvent used in the process usually acts as a solvent for the resulting polymer. Therefore solution polymerization is only suitable for production of wet polymer types. It is mainly used for vinyl acetate, acrylonitrile, and esters of acrylic acid.

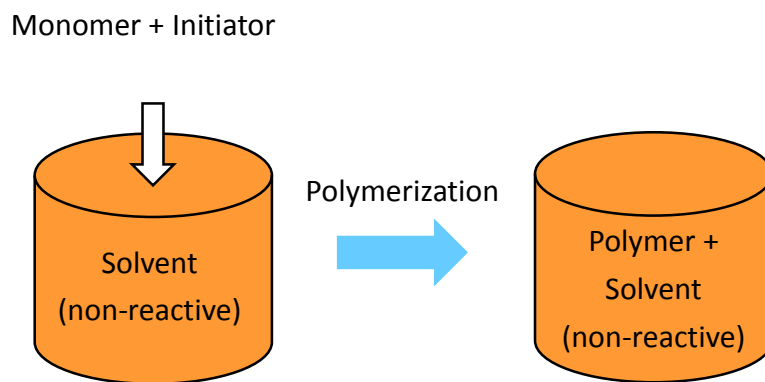


**Fig. 3.6. Schematic diagram of process of solution polymerization.**

### **3.2.1.2 Bulk polymerization**

Fig. 3.7 illustrates the general process in bulk polymerization. Bulk polymerization is a process that is carried out by adding soluble initiator to pure monomer in liquid state. The reaction is initiated by heating or exposing to radiation. As the chemical reaction proceeds the mixture becomes more viscous. The resulting polymer is in solid state. Bulk polymerization is mainly used for ethylene, styrene, and methyl

methacrylate.

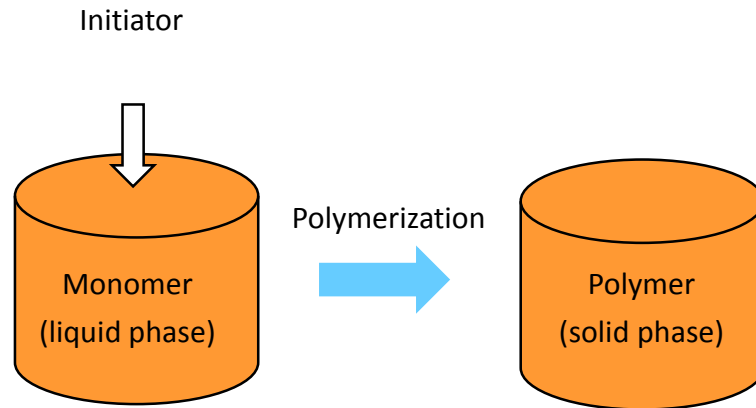


**Fig. 3.7. Schematic diagram of process of bulk polymerization.**

### **3.2.1.3 Advantages and disadvantages of the solution and bulk polymerization**

The advantages and disadvantages of the solution and bulk polymerization are

listed in Table 3.2.

**Table 3.2 Advantages and disadvantages of the solution and bulk polymerization**

Solution polymerization	Bulk polymerization
<p>Advantages:</p> <ul style="list-style-type: none"> <li>● Useful for polymer used as solution</li> <li>● Better heat control - solvent can absorb generated heat</li> <li>● Solvent can reduce viscosity to make process easier</li> </ul>	<p>Advantages:</p> <ul style="list-style-type: none"> <li>● Simple process</li> <li>● High purity of resulting polymer</li> <li>● Large casting is possible</li> <li>● Wide range of molecular masses can be obtained with the use of chain transfer agent</li> </ul>
<p>Disadvantages:</p> <ul style="list-style-type: none"> <li>● Low molecular weight of resulting polymer</li> <li>● Difficult to remove solvent in the resulting polymer</li> <li>● Solvent has to be removed to obtain pure polymer</li> <li>● Expensive due to additional solvent cost</li> <li>● Environmental unfriendly due to solvent release</li> </ul>	<p>Disadvantages:</p> <ul style="list-style-type: none"> <li>● Difficult to mix as viscosity of mixture increases</li> <li>● Heat transfer problem due to exothermic reaction</li> </ul>

### 3.2.2 Evaluation of refractive index from chemical structure of polymer

The refractive index of polymer or co-polymers can be evaluated by the Lorentz-Lorentz equation, a correlation between chemical structure and refractive index [4, 5]. The refractive index is then deduced by

$$\frac{n^2 - 1}{n^2 + 2} \cdot \frac{N_A \sum_i \Delta V_i}{K_{av}} = R \quad \text{Equation 3.1}$$

For amorphous and glassy homo-polymer blends or co-polymers, Equation 3.1 becomes

$$\begin{aligned} \frac{n^2 - 1}{n^2 + 2} \cdot \frac{N_A [\alpha_1 (\sum_i \Delta V_i)_1 + \alpha_2 (\sum_i \Delta V_i)_2 + \dots + \alpha_n (\sum_i \Delta V_i)_n]}{K_{av}} & \quad \text{Equation 3.2} \\ & = \alpha_1 R_1 + \alpha_2 R_2 + \dots + \alpha_n R_n \end{aligned}$$

, where the definitions of symbols in Equation 3.1 and 3.2 are listed in Table 2.3.

**Table 3.3. Definition of symbol in Equation 3.1 and 3.2**

Symbol	Definition	Unit
$n$	Refractive index	
$N_A$	Avogadro constant: $6.023 \times 10^{23}$	$mol^{-1}$
$\Delta V_i$	Van-der-Waals volume of the $i$ -th atom in the chemical structure of the repeating unit	$\text{\AA}^3$
$\sum_i \Delta V_i$	Van-der-Waals volume of the repeating unit	$\text{\AA}^3$
$K_{av}$	Molecular packing coefficient, a universal constant For bulk polymer: 0.681 For film prepared from solution: 0.695	
$(\sum_i \Delta V_i)_1, (\sum_i \Delta V_i)_2, \dots, (\sum_i \Delta V_i)_n$	Van-der-Waals volume of the repeating unit for each component in a co-polymer or a polymer blend	$\text{\AA}^3$
$\alpha_1, \alpha_2, \dots, \alpha_n$	Molar fraction for each component in a co-polymer or a polymer blend	
$R_1, R_2, \dots, R_n$	Molar fraction of the repeating unit for each component in a co-polymer or a polymer blend	$cm^3 mol^{-1}$

### **3.3 POF**

POF is an optical fiber which is entirely made out of polymer. A typical POF consists of PMMA core and fluorinated or perfluorinated [6, 7] polymers cladding. Similar to traditional glass fiber, POF transmits light through the core of the fiber by total internal reflection. However, the core size of POF is 100 times larger than glass fiber. Since the attenuation of POF is much higher than that of glass fiber, POFs are usually used for short-range optical data transmission in home and automotive networks. Due to the superior advantages of polymeric materials, POFs doped with organic laser dyes can be used as fiber light sources and lasers.

#### **3.3.1 Optical fibers**

Optical fiber is a flexible, transparent fiber made of high quality glass or polymer. Optical fiber typically consists of a transparent dielectric core surrounded by a transparent dielectric cladding material. The boundary between the core and the cladding can be step or gradual in the sense of index of refraction profile. If the profile is a step, it is called step-index fiber. If the profile is gradual, it is called graded-index fiber.

Optical fiber can function as a waveguide to transmit light between the two ends of

the fiber. To confine light in the core, the refractive index of the core must be greater than that of the cladding. The underlying working principle is the total internal reflection at the interface between the core and cladding, which confines the propagating light beam within the core.

### **3.3.2 Principle of guiding light in optical fibers**

Total internal reflection is a phenomenon that happens when a propagating light hits a boundary in a medium (core) at an angle larger than a critical angle with respect to the normal to the boundary surface. If the refractive index of the medium (core) the light travelling is larger than the other side (cladding) of the boundary, the light is completely reflected from the boundary, and it bounces back and forth off the boundary along the whole fiber. The critical angle can be determined by using the Snell's law (see Fig. 3.8 for illustration),

$$n_1 \sin \theta_i = n_2 \sin \theta_t \quad \text{Equation 3.3}$$

, where  $n_1$  and  $n_2$  are the refractive indices of respective media,  $\theta_i$  and  $\theta_t$  are the angles of incidence and refraction of light ray measured from the normal of the boundary between respective media.

To determine the critical angle, we have to find  $\theta_i$  when  $\theta_t = 90^\circ$ , and thus  $\sin \theta_t = 1$ . Therefore the value of  $\theta_i$  is equal to the critical angle  $\theta_c$ . Now, the critical angle is

$$\theta_c = \theta_i = \sin^{-1}\left(\frac{n_2}{n_1}\right) \quad \text{Equation 3.4}$$

This equation is only valid for  $n_2 < n_1$ . If the incident light ray is at the critical angle, the refracted light ray is tangent to the boundary and propagates along the boundary. However, if the incident angle of light ray is larger than the critical angle, the light ray is completely reflected from the boundary.

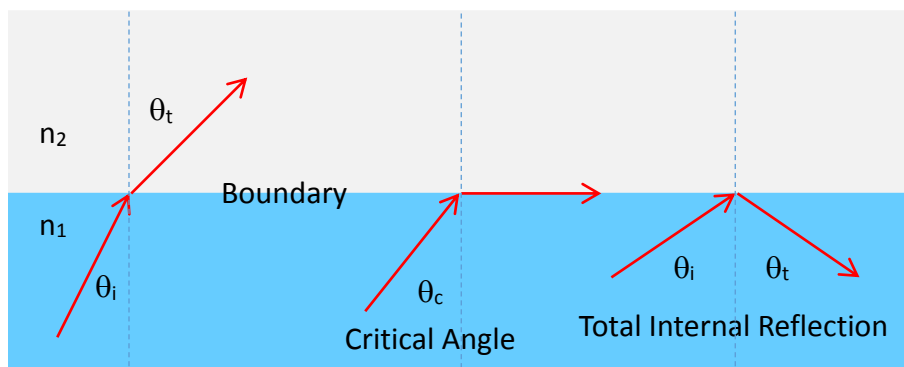


**Fig. 3.8. Illustration of propagating light ray incident on the boundary between two media.**

### 3.3.3 Multi-mode fibers and single-mode fibers

There are two types of optical fibers as illustrated in Fig. 3.9: one type is called multi-mode fiber (MMF) which can support numerous propagation paths or transverse modes of light; another type is called single-mode fiber (SMF) which can only support a single transverse mode of light. MMFs generally have a larger core diameter, and are used for short-haul communications and for applications of high power transmission, whereas SMFs are mainly used for long-haul communications.

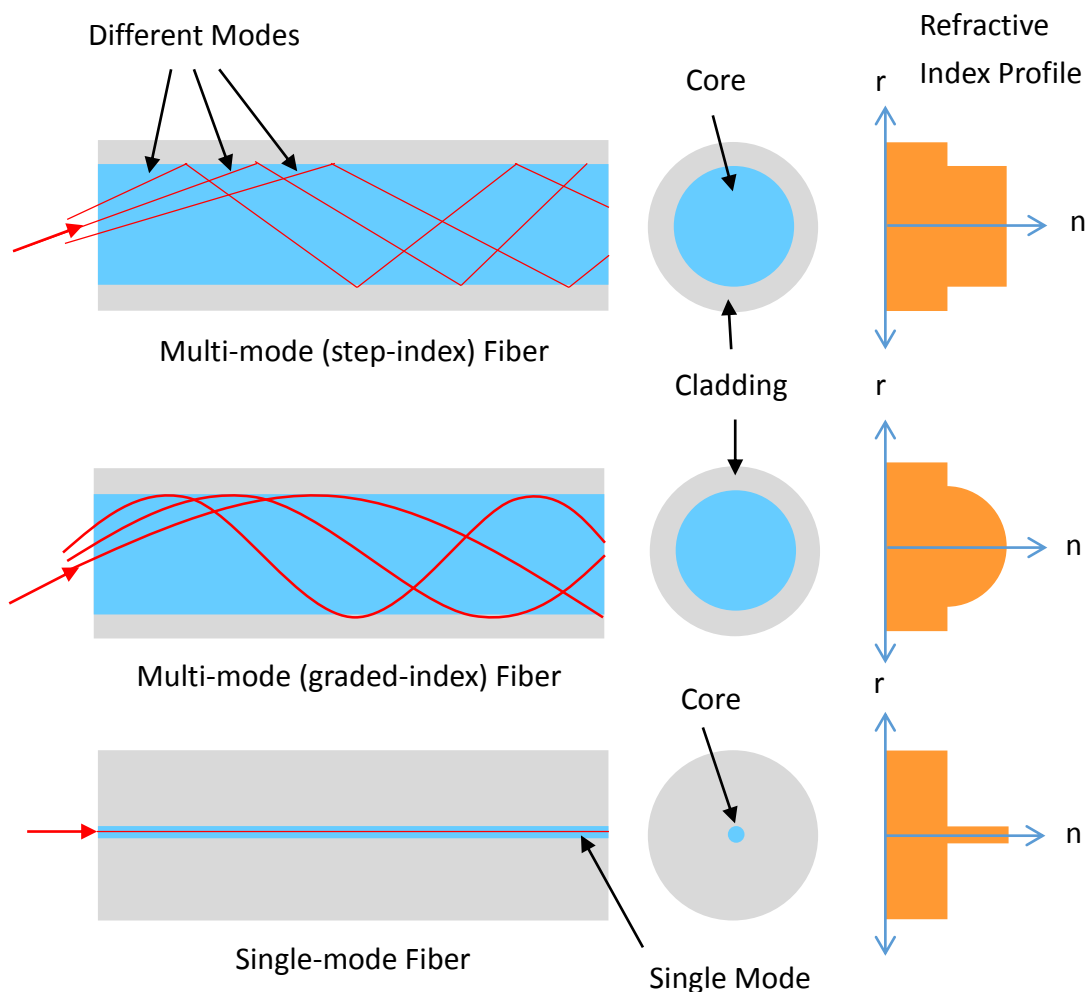


Fig. 3.9. Schematic diagrams of MMFs (step-index and graded-index) and SMF.

### 3.4 POF dye lasers

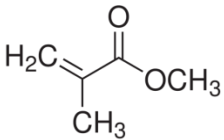
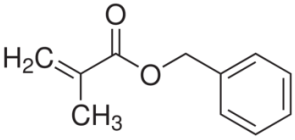
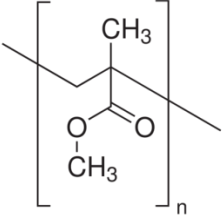
#### 3.4.1 Materials for dye-doped polymeric preform and POF dye lasers

In this study, the main constituent of POFs is PMMA. MMA can also be co-polymerized with other monomers to modify the physical properties of the resultant copolymer. For instance, the overall glass transition temperature ( $T_g$ ) of a polymeric preform can be decreased by adding suitable amount of benzyl methacrylate (BzMA), which has a lower  $T_g$  of 54°C compared with 105°C of MMA after polymerization [8]. With lower  $T_g$ , polymeric preform can be easily drawn at lower temperature. Besides, BzMA has a higher refractive index of 1.568 compared to 1.490 of MMA after polymerization [8]. It can therefore be used to increase the overall refractive index of the resultant copolymer. This resultant copolymer can be used as the core material of POFs. The molecular structures of MMA, BzMA, and PMMA are shown in Table 3.4.

**Table 3.4. (Left) Molecular structures of MMA, BzMA, and PMMA, and (Right)**

**Values of symbols in Equation 3.2 for MMA and BzMA to calculate the refractive**

**index of the core and cladding materials of POF in this study.**

Molecular Structure	Values of Symbols in Equation 3.2 (from Appendix 1 and 2 of [26])
 <p data-bbox="416 992 788 1025">Methyl methacrylate (MMA)</p>	$(\sum_i \Delta V_i)_1 = 96.7 \times 10^{-24} \text{ cm}^3$ $\alpha_1 = 0.75$ $R_1 = 24.744 \text{ cm}^3 \text{ mol}^{-1}$
 <p data-bbox="416 1379 788 1413">Benzyl methacrylate (BzMA)</p>	$(\sum_i \Delta V_i)_2 = 172.5 \times 10^{-24} \text{ cm}^3$ $\alpha_2 = 0.25$ $R_2 = 48.851 \text{ cm}^3 \text{ mol}^{-1}$
 <p data-bbox="368 1809 836 1843">Poly(methyl methacrylate) (PMMA)</p>	

For all the works in this study, the core material of POF is a copolymer of MMA and BzMA in mole ratio of 75 to 25 whereas the cladding material is pure PMMA. By using Equation 3.2 and the parameters in Table 3.4, the evaluated refractive indexes of the core and cladding of our POF are 1.5135 and 1.4904 respectively.

In this study, the polymeric preform was produced by bulk polymerization. The polymerization process is carried out by adding a small amount of soluble initiator to the pure monomers in liquid phase. The role of the initiator is to produce radical species and promote radical reaction as well as accelerate the reaction rate at the beginning stage of polymerization [9]. Azo compounds, organometallic reagents, Lewis acids and peroxides are typically used as the radical initiators. In this study, lauroyl peroxide (LP) was used as the radical initiator. On the other hand, 1-decanethiol (DT) was used as the chain transfer agent, which was employed as a regulator of molecular weight of polymer [10]. Since the molecular weight distribution of the resultant polymer can be easily changed by varying the amount of chain transfer agent, DT is important in determining how easily the polymeric preform can be processed into fibers.

The best method for making high-quality preforms is to start with a liquid monomer,

dissolve the dopant in the monomer, and polymerize the material. Polymerization requires an initiator (which starts the polymerization process), a chain transfer agent (which limits the chain lengths of the polymer formed), and a plasticizer (which controls the rheological properties of the polymer) [27]. Polymer molecular weight is important because it determines many physical properties such as glass transition temperature and viscosity. Unlike small molecules, however, the molecular weight of a polymer is not one unique value. Rather, a given polymer will have a distribution of molecular weights. The distribution will depend on the way the polymer is produced.

It is important to match the initiator, the chain transfer agent that cause the chemical reaction that forms the polymer, with the dopant dyes. Certain initiators cause the dyes to decompose while others cause bubbling and foaming. The bond between two oxygens in the peroxide is very weak and breaks apart from thermal activation with a half-life that decreases with temperature. The two radicals of the peroxide are highly chemically active. Each one bonds to one side of a monomer molecule and opens a chemically active site on the other side of the monomer molecule. This site then bonds to a second monomer molecule to begin chain formation and is followed by sequential chain growth until the process is terminated

by encountering a molecule of the chain transfer agent. The average chain length of the polymer is therefore determined by the chain transfer agent concentration.

For a polymer to have the correct mechanical properties for fiber drawing, it is important to control the average chain length during the polymerization process. If the chain length is too short, the fiber is brittle and cracks upon handling. If the chain length is too long, the polymer does not flow even at temperatures well beyond the decomposition temperature of the dyes.

**Table 3.5 Summary of preform composition for core and cladding materials.**

	Monomer (mol%)		Initiator (mol%)	Chain Transfer Agent (mol%)
	MMA	BzMA	LP	DT
Core Material	75	25	0.1	0.25
Cladding Material	100	0	0.1	0.25

**Error! Reference source not found.**3.5 lists the composition of the core and cladding materials, the initiator, and the chain transfer agent for the fabrication of

the polymeric preform in this study. The fabrication process of dye-doped polymeric preform was mainly divided into two parts. The first part was to prepare a pure PMMA tube as the cladding of the preform. The second part was to make the core of the preform by filling the pure PMMA tube prepared in first part with MMA/BzMA co-polymer. The details of the fabrication process is discussed in the next section.

### **3.4.2 Fabrication of dye-doped polymeric preform and POF dye lasers**

The first step of the polymeric preform fabrication is the pre-polymerization process. Firstly the monomers, the initiator, and the chain transfer agent were mixed together in a glass conical flask. The solution mixture was then stirred at temperature of 75°C until it became viscous. The pre-polymerization process lasted for about 30 minutes. The partially-polymerized mixture was then be poured into a glass mold. The mold is a 22mm diameter glass test tube with a 10mm diameter Teflon rod inserted at the centre. The glass mold was transferred to an oven for further polymerization which took about 4 days. The temperature of the oven was computer controlled to give a pre-defined temperature profile. Fig. 3.10 shows the relation between the actual and preset polymerization temperature as a function of time.

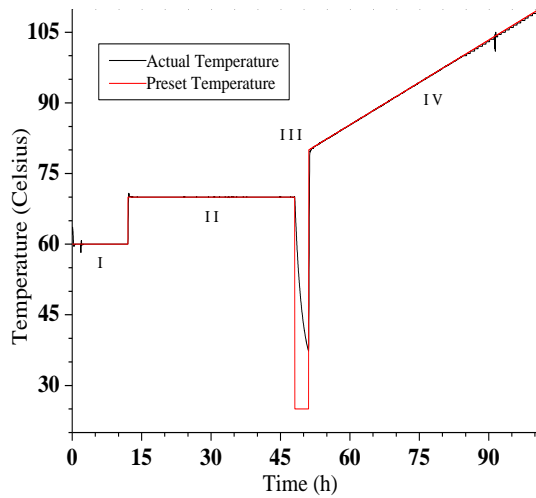


**Fig. 3.10. Actual and preset temperature for polymerization of preform monomers.**

Because the viscosity of pre-polymerized mixture is high, it is very easy for the gelatinous effect to occur. Therefore, polymerization has to start at a lower temperature of 60°C at stage I to prevent explosive polymerization. Stage II offers sufficient time for the mixture to reach conversion equilibrium that monomers are converted to polymer. Such conversion equilibrium for PMMA can be calculated by the empirical equation:  $\text{conversion (\%)} = 0.225 \cdot T (\text{°C}) + 78.25$ , where  $T$  is the polymerization temperature [11]. It implies that at the end of stage II, at  $T = 70^\circ\text{C}$ , conversion = 94%. This means that only 6% of monomer residue is left in the mixture. At stage III, the temperature is then decreased to room temperature to let

the polymer contract and detach from the glass mold. Otherwise, it is hard to remove the polymer from the glass mold after polymerization. Then during Stage IV, the temperature is elevated again gradually from 80°C to 110°C for the fully polymerization of the polymer preform. Finally, the glass mold is taken out from the oven and cooled slowly at room temperature. The solidified PMMA tube is then obtained by breaking the glass mold carefully.

The cladding preforms are then placed back to oven and heated at 95C for several days to remove any remaining volatiles such as the chain transfer agent.

The PMMA tube is then filled with MMA/BzMA monomers in liquid phase, and goes through the same polymerization process mentioned above to obtain the polymeric preform for this study. For dye-doped polymeric preform, organic laser dyes can be introduced into the mixture of monomers, initiator, and chain transfer agent during the pre-polymerization process. The resultant polymeric preform was drawn into POF at 235-260°C using a home-made fiber drawing tower.

### 3.5 Random lasers

A laser is a device that emits coherent light through the process of optical amplification based on stimulated emission of electromagnetic radiation. Therefore, LASER stands for Light Amplification by Stimulated Emission of Radiation. The main difference between random laser and conventional laser is the optical feedback mechanism.

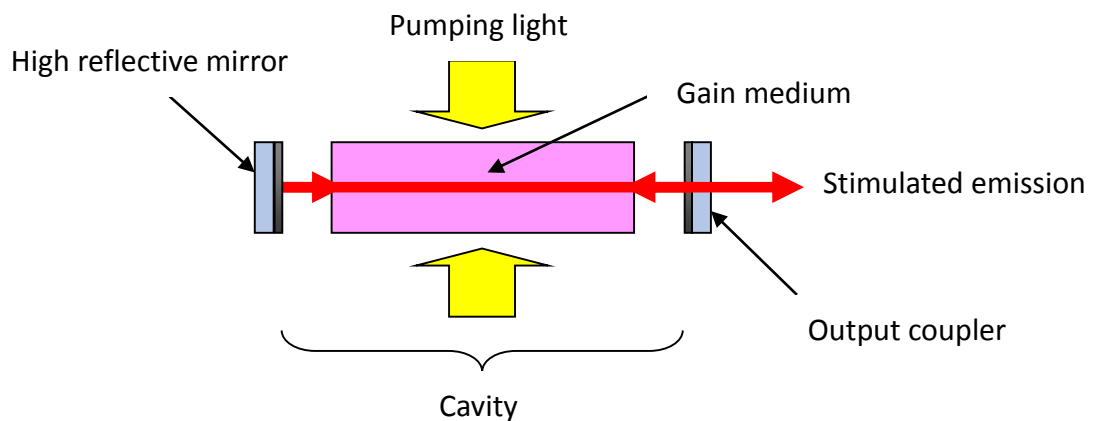


**Fig. 3.11. Schematic diagram of a conventional laser structure.**

A conventional laser consists of two essential components: a gain medium and a cavity, as shown in Fig. 3.11. The gain medium supplied with energy can amplify

light by stimulation emission. The cavity, generally formed by two mirrors, provides coherent optical feedback for the stimulated emission in the gain medium. The light passes through the gain medium and gets amplified while bouncing back and forth between the mirrors. Typically, one of the mirrors has a reflectivity of 99%, and another one, acts as an output coupler, is partially transparent. Laser light can escape through this mirror.

Light scattering has been considered detrimental to lasing process because it changes the direction and spatial coherence of light paths in traditional laser cavity. However, light scattering plays an important and positive role in random lasers. The optical feedback in a random laser is provided by multiple scattering of light in a disordered medium. Multiple scattering can increase the travel path length or time of light in the gain medium, hence the optical amplification by stimulated emission is enhanced. In addition, recurrent multiple scattering of light can provide coherent feedback for laser oscillation. In multiple scattering, the emitted light may return back to the scattering position where it is scattered previously, and a closed loop path is therefore formed. When the gain obtained by the emitted light through the amplification along the closed loop path exceeds the loss, laser oscillation can occur in a closed loop path which forms the laser resonator.

### 3.5.1 Two kinds of random lasers

In general, there are two kinds of optical feedback in random laser. One is the intensity or energy feedback which is incoherent and non-resonant, and the other is field or amplitude feedback which is coherent and resonant [12].

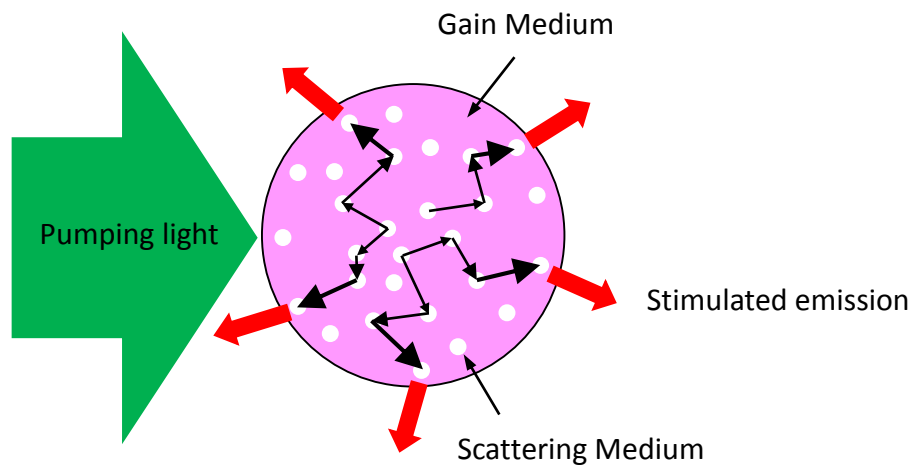


**Fig. 3.12. Schematic diagram of a random laser with incoherent and non-resonant feedback.**

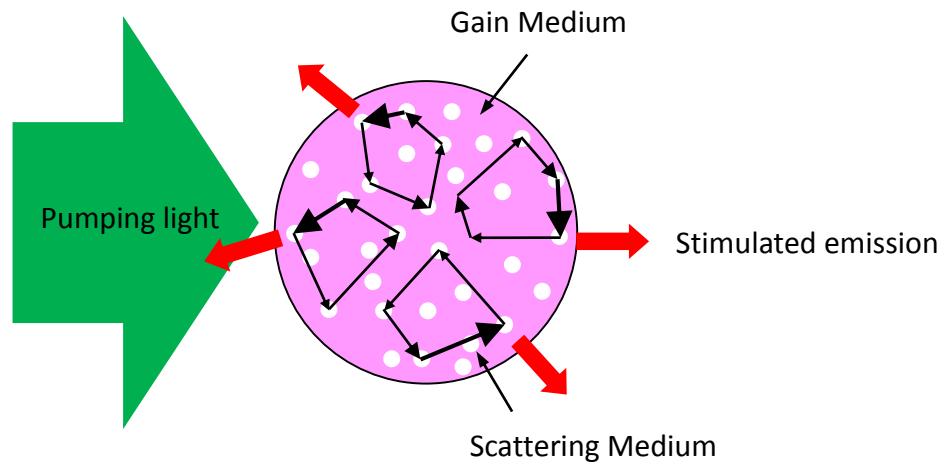


**Fig. 3.13. Schematic diagram of a random laser with coherent and resonant feedback.**

As shown in Fig. 3.12, when the scattering is weak, light is scattered and undergoes a random walk; and during each random walk of scattering, the light is amplified along the open trajectory before leaving the disordered gain medium. The optical feedback of this lasing mechanism is incoherent and non-resonant. However, when the scattering is strong, as shown in Fig. 3.13, light may return to the initial scattering position after a random walk of scattering in the disordered medium, which forms a closed loop path. When the gain obtained by the amplified light along the closed loop path exceeds the loss, laser oscillation can occur in the closed

loop path which acts as a laser resonator. Since the light may come back to the original position through many different paths, all of the backscattered light waves interfere and determine the lasing frequencies. This kind of optical feedback provided by recurrent multiple scattering is coherent and resonant.

### **3.5.2 Scattering of light in random lasers**

Scattering of light happens everywhere in our daily life such as blue sky during day time, red sky at sunrise and sunset, white cloud, what we see through scattering of light from surface, etc. Rayleigh scattering is an elastic scattering of light by particles of size much smaller than the wavelength of light that is scattered by the particles. Mie scattering is the general case for scattering of light by particles of any size.

Light scattering is a form of scattering in which light is the form of propagating energy which is scattered. Light scattering in random laser in general is elastic. Elastic scattering of light by particles, depending on their size, can be classified into three regimes: (1) Rayleigh scattering regime is an elastic scattering of light by particles of size much smaller than the wavelength of light that is scattered by the

particles. (2) Geometric optics can be used to study the scattering of light by spherical or non-spherical particles under the condition that the size of particle is much larger than the wavelength of light. (3) Mie scattering is the general case for scattering of light by particles of any size.

To distinguish the three scattering regimes, a relevant size parameter  $x$  for light scattering of wavelength  $\lambda_0$  from spherical dielectric particle of radius  $a$  is defined by

$$x = ka = \frac{2\pi n_m a}{\lambda_0} \quad \text{Equation 3.5}$$

, where  $k$  is the wavenumber and  $n_m$  is the refractive index of the medium.

The Rayleigh scattering limit is when  $x \ll 1$ . For the classical geometric optics limit,  $x \gg 1$ . Scattering from any spherical particle with an arbitrary value of  $x$  can be approximated by Mie scattering.

Despite the above different optical feedback mechanisms, the scattering process is characterized by two important length scales, namely scattering mean free path  $l_s$

and transport mean free path  $l_t$ . Scattering mean free path  $l_s$  is defined as the average distance of light travelling between two consecutive scattering events. Transport mean free path  $l_t$  is defined as the average distance that light travels before its propagating direction is changed. These lengths scales are related by

$$l_t = \frac{l_s}{1 - \langle \cos \theta \rangle} \quad \text{Equation 3.6}$$

, where  $\langle \cos \theta \rangle$  is the average cosine of the scattering angle, which can be found from the differential scattering cross section. For Rayleigh scattering,  $\langle \cos \theta \rangle = 0$  or  $l_t = l_s$ , while for Mie scattering,  $\langle \cos \theta \rangle \approx 0.5$  or  $l_t \approx 2l_s$  [12].

The transport mean free path can be characterized by conducting coherent back scattering experiment [13, 14]. In the experiment, a probe light with wavelength very close to the emission wavelength of the incorporated dye is incident on the sample. To avoid the absorption of the probe light, the sample contains only the scatterers but not the dye molecules. Provided that the sample size is much larger than the transport mean free path, the transport mean free path is calculated by

$$l_t = \frac{\lambda}{2\pi w(1 + z_e)} \quad \text{Equation 3.7}$$

, where  $\lambda$  is the wavelength of probe light,  $w$  is the angular width of the back scattering cone, and  $z_e$  is the extrapolated length ratio [15]. It is assumed that it only depends on the overall reflectivity  $R$  at the sample-air interface [15], Equation 3.6 becomes

$$l_t = \frac{\lambda}{2\pi w \left[ 1 + \frac{2(1 + R)}{3(1 - R)} \right]} \quad \text{Equation 3.8}$$

On the other hand, when the average size of the scatterers is much larger than the wavelength of light that travels in the disordered medium, the scattering mean free path can be deduced theoretically by Mie theory.

Assume the scatterers are non-light-absorbing spherical particles of diameter  $d$  and occupy a volume fraction  $\phi$  in a disordered medium. The scattering mean free path  $l_s$  of photons in such scattering system can be calculated by

$$l_s = \frac{2d}{3\phi Q_s} \quad \text{Equation 3.9}$$

, where  $Q_s$  is the scattering efficiency factor, which is defined as the ratio of the scattering cross section  $\sigma_s$  to the physical cross section ( $\pi r^2$ ) of the particle, that is,  $Q_s = \sigma_s/(\pi r^2)$ . It can be evaluated numerically for spherical particles by Mie theory calculation. The detailed model and programming code [16, 17] are listed in Appendix.

### 3.5.3 Three regimes of scattering in random lasing

Since the optical feedback of random laser is provided by multiple scattering of light in a disordered medium, the laser action depends on the amount of scattering in the gain medium. In general, scattering can be distinguished into three regimes [18]: (1) weak scattering with gain (scattering mean free path is of the order of sample size  $L$  or  $l_s \sim L$ ) [19] – the introduction of some scatterers only diffuse the ASE of random laser, (2) modest scattering with gain (scattering mean free path is much smaller than sample size but still larger than the wavelength of light  $\lambda$ , or  $L \gg l_s \gg \lambda$ ) [20, 21] – the presence of scatterers not only lengthens the transport path of light, but also prolong the dwelling time of light in the active medium which results in strong gain narrowing, and (3) strong scattering with gain (scattering

mean free path is equal to or smaller than the wavelength of light or  $l_s \leq \lambda$ ) [22, 23, 24] – localization and recurrent scattering of light occur forming closed loop paths which provide coherent and resonant feedback in random laser. The scattering mean free path can be estimated by the Mie theory. The details of the theory and the numerical method used to determine the scattering mean free path are shown in Section 4.3.

Experimentally, discrete narrow lasing lines based on interference of scattered lights occurs in the emission spectrum for random lasers with coherent (resonant) feedback, whereas there is only a smooth narrow peak in the emission spectrum for random lasers with incoherent (non-resonant) feedback. However, recent numerical and analytical works on random lasers reported by J. Andreasen and co-workers [25] showed that discrete narrow lasing lines based on interference do exist. It was found that this observation occurs not only in strongly scattering random lasers based on localized modes, but also in diffusive and even in weakly scattering random lasers. However, the vast majority of random lasers do not operate in the localized regime, so the nature and origin of the laser action in a diffusive or quasi-ballistic random laser are still not clear.

### 3.5.4 Advantages and disadvantages of random lasers

Random lasers offer many advantages over conventional lasers. The four main advantages are:

1. Low spatial coherence of random lasers

The low spatial coherence of specifically designed random lasers can be used in speckle-free full-field imaging in the setting of intense optical scattering. The images generated with random laser illumination exhibit superior quality than images generated with spatially coherent illumination generated from conventional light sources. By providing intense laser illumination without the drawback of coherent artefacts, random lasers are well suited for a host of full-field imaging applications from full-field microscopy to miniature digital light projector systems to medical imaging. For example, for full-field optical coherence tomography, using thermal light sources or LEDs is not an option because low spatial coherent and high intensities are required to probe deeper into the tissue. This provides random lasers with a unique opportunity.

2. Compactness of random lasers with cluster of nano-scatterers

The scatterers in a random laser are made of nanoparticles, thus the laser cavity can be formed in a micro-cluster of the particles, rendered a small footprint of the laser. For example, a spectrometer with a spectral resolution of

0.75 nm at a wavelength of 1,500 nm in a 25-mm-radius structure has been reported. Such a compact, high-resolution spectrometer is well suited for lab-on-a-chip and lab-in-a-fibre spectroscopy applications.

3. Sensitivity of random lasing modes to scatterer density

Because the modes of a random laser are sensitive to the scatterers, one may use the random laser as a sensor for anything that modifies the scattering characteristics of the medium. So sensing is certainly one potential application. For example, one can insert a small random fibre laser sensor head to a fibre system that can be employed in hostile environments.

4. Uniqueness of random lasing frequency

The lasing frequency acts as a fingerprint of the random system. The counterfeiting industry would benefit, as well as for medical diagnostics. For example, by understanding the lasing process in a disordered medium, researchers have looked at using random lasers to distinguish cancer cells from healthy human cells. This is a very active field which makes use of the fact that different tissue and bone types have different optical structures and transport mean free path.

### 3.6 Reference

1. F. P. Schäfer, "Principles of dye laser operation", Top. Appl. Phys. Vol. 1, 1-85, ISBN 0-387-08470-3 (1977)
2. K. H. Drexhage, "Structure and properties of laser dyes", Top. Appl. Phys. Vol. 1, 144-193 (1977)
3. R. F. Kubin and A. N. Fletcher, "Fluorescence quantum yields of some rhodamine dyes", J. Lumin., Vol. 27, 455 (1982)
4. A. Askadskii, "Influence of chemical structure on the properties of polymers", Pure & Appl. Chem., Vol. 46, 19 (1976)
5. A. Askadskii, "Physical properties of polymers prediction and control", ISBN: 2-88449-155-4, Gordon and Breach Publishers, The Netherlands (1996)
6. Y. Koike, "Graded-index and single-mode polymer optical fiber", MRS proc., Vol. 247, 817 (1992)
7. Y. Koike, T. Ishigure, and E. Nihei, "High-bandwidth graded-index polymer optical fiber", J. Light. Tech., Vol. 13, 1475 (1995)
8. J. Brandrup, E. H. Immergut, E. A. Grulke, "Polymer handbook," ISBN: 0471166286, a Wiley-Interscience publication, 4th edition (1999)
9. Robert O. Ebewele, "Polymer Science and Technology", CRC Press, ISBN: 978-0-8493-8939-9 (2000)

10. Seymour, Carraher, "Polymer Chemistry", 7<sup>th</sup> Edition, ISBN: 1-4200-5102-4, CRC Press (2008)
11. Li, B.G., Yu, Z. Z., Cai, Q. Z., Li, B. F., Gao Fen Zi Tong Xun, Vol. 5, 326 (1984)
12. H. Cao, "Lasing in random media", Wav. Rand. Med., Vol. 13, R1 (2003)
13. M. P. van Albada and A. Lagendijk, "Observation of weak localization of light in a random medium", Phys. Rev. Lett., Vol. 55, 2692 (1985)
14. P. E. Wolf and G. Maret, "Weak localization and coherent backscattering of photons in disordered media", Phys. Rev. Lett., Vol. 55, 2696 (1985)
15. Y. Ling, H. Cao, A. L. Burin, M. A. Ratner, X. Liu, and R. P. H. Chang, "Investigation of random lasers with resonant feedback", Phys. Rev. A., Vol. 64, 063808 (2001)
16. Guillaume Baffou, "Mie theory for metal nanoparticles", Chargé de recherche CNRS, Institut Fresnel, Université Aix-Marseille, France, (2012)
17. C. F. Bohren and D. R. Huffman, "Absorption and scattering of light by small particles", Wiley interscience, (1983)
18. D. S. Wiersma and Ad Lagendijk, "Interference effects in multiple-light scattering with gain", Phys. A, Vol. 241, 82 (1997)

19. X.Wu, W. Fang, A. Yamilov, A. A. Chabanov, A. A. Asatryan, L. C. Botten, and H. Cao, "Random lasing in weakly scattering systems," *Phys. Rev. A*, Vol. 74, 053812 (2006)
20. C. Vanneste, P. Sebbah, and H. Cao, "Lasing with resonant feedback in weakly scattering random systems," *Phys. Rev. Lett.*, Vol. 98, 143902 (2007)
21. C. Vanneste and P. Sebbah, "Complexity of two-dimensional quasimodes at the transition from weak scattering to Anderson localization," *Phys. Rev. A*, Vol. 79, 041802(R) (2009)
22. X. Jiang and C. M. Soukoulis, "Time dependent theory for random lasers", *Phys. Rev. Lett.*, Vol. 85, 70–73 (2000)
23. C. Vanneste and P. Sebbah, "Selective excitation of localized modes in active random media," *Phys. Rev. Lett.*, Vol. 87, 183903 (2001)
24. P. Sebbah and C. Vanneste, "Random laser in the localized regime," *Phys. Rev. B*, Vol. 66, 144202 (2002)
25. J. Andreasen, A. A. Asatryan, L. C. Botten, M. A. Byrne, H. Cao, L. Ge, L. Labonté, P. Sebbah, A. D. Stone, H. E. Türeci. And C. Vanneste, "Modes of random lasers", *Adv. Opt. Phot.*, Vol. 3, 88 (2011)
26. J. M. Yu, "Photosensitive polymer optical fibers and grating", PhD Thesis (2005)

27. Mark G. Kuzyk, "Polymer fiber optics: materials, physics, and applications", CRC Press, ISBN 1-57444-7068-8 (2007)

## **CHAPTER 4**

### **POF ASE Light Source**

#### **4.1 Introduction**

In this chapter, we present a simple approach to form an optical feedback cavity of a dye-doped POF ASE light source. The optical feedback cavity was formed by directly coating a gold mirror with high reflectance on one cleaved and polished fiber end-face to act as a back reflector. The other fiber end-face was cleaved and polished with or without gold mirror to act as an output coupler. To study the effect of cavity mirror reflectivity at the output coupler on the emission characteristics, dye-doped POF with various cavity mirror reflectivity were fabricated, and the experimental results are presented in section 4.2.

Moreover, among the demonstrated POF lasers in [22, 23, 24] of Chapter 2, it was observed previously that organic laser dye was only doped in fiber core, or in the whole fiber without core. These kinds of POF lasers might suffer from high optical cavity loss, because the core was highly doped in order to maintain an acceptable level of output power and the required operating lifetime. In view of this, we propose a novel doping structure of step-index dye-doped POF in which the

cladding is highly doped and the core is slightly doped with organic laser dye to implement a prolonged operating lifetime with useful output power. To investigate the effect of core doping concentration on emission characteristics, the core was doped with various concentrations of dye. The emission spectrum, output power as well as emission lifetime as a function of input pump power are demonstrated and shown in section 4.3.

## **4.2 Effect of reflectance of gold mirrors coated output coupler on emission characteristics of dye-doped POFs**

### **4.2.1 Fabrication**

In this study, a step-index dye-doped POF was drawn from a preform produced by the casting/moulding method as described in Chapter 3. The preform has an inner diameter and an outer diameter of 10mm and 22mm respectively. The inner cylindrical core is made of copolymer of MMA and BzMA in mole ratio of 75 to 25. The outer tubular cladding is made of pure MMA. Both core and cladding are doped with 200ppm Rh640 (Exciton) organic laser dye. The preform was drawn into fiber with outer diameter of 950 $\mu$ m, and a core diameter of 450 $\mu$ m. Another step-index dye-doped POF of same structure with undoped core was fabricated for comparison.

The dye-doped POF was cut into 5cm long pieces, and their end-faces were polished to optical grade by hand using fiber polishing sheets of 6 $\mu$ m, 3 $\mu$ m and 1 $\mu$ m grit size in turn. Five dye-doped POF with 5cm long were prepared. The detailed technique for coating of gold on the fiber end-face is described in the following section 4.2.2.

#### **4.2.2 Gold mirror coating on fiber end by DC sputtering**

The optical feedback cavity was formed by directly coating a gold mirror on one cleaved and polished fiber end-face to act as a back reflector. The other fiber end-face was cleaved and polished, and then also coated with gold mirror to act as an output coupler. The process of gold mirror coating was performed using a DC sputter deposition machine (KYKY SBC-12; a conventional scanning electronic microscope (SEM) sputter coater) as illustrated in Fig. 4.1. In each coating process, only one end-face was exposed to the gold plasma, and the rest of the fiber was protected by a glass capillary jacket. This is important because the rest of the fiber surface needed to be transparent for side-pumping.

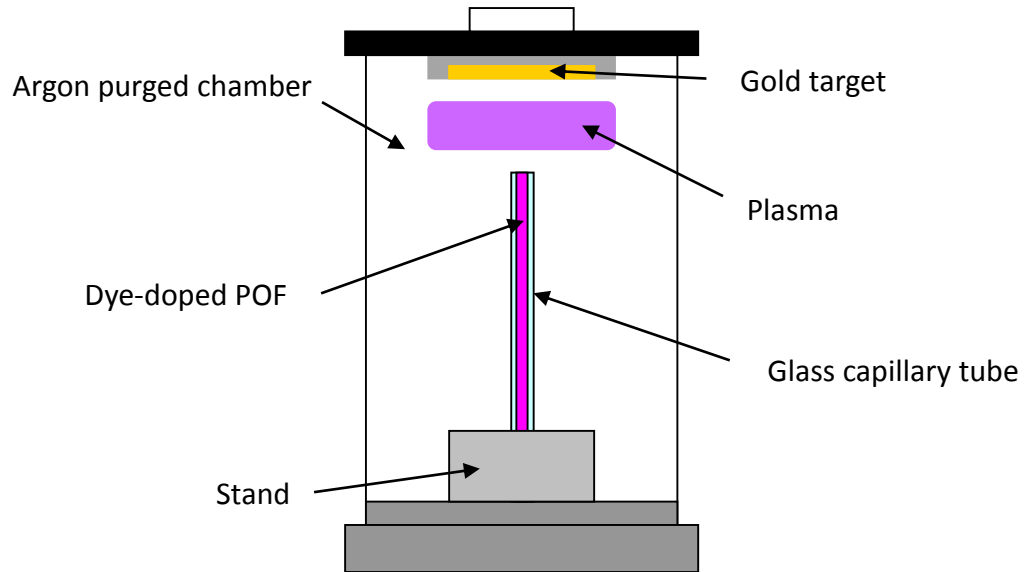


**Fig. 4.1. Schematic diagram of a conventional SEM sputter coater for gold mirror coating on fiber end-face.**

The reflectivity of gold mirror formed on one fiber end-face depends on its thickness which is a function of the deposition time. To obtain a high reflectivity of gold mirror coated on a fiber end, an optimal sputtering deposition time has to be determined. Since the reflective index of the fiber core material is close to that of the flat glass slide, the reflectivity measured can be approximated to the reflectivity of gold mirror on polymer fiber end. A flat glass slide was positioned at the same height of the fiber end-face inside the sputtering chamber as shown in Fig. 4.2. A thin layer of gold was formed on the glass slide surface by sputtering. The reflectance of the gold mirror was measured by a UV-Vis spectrophotometer

(Varian Cary 100). Fig. 4.3 shows the dependence of reflectance on sputtering deposition time over the visible spectrum for gold mirror formed on flat glass slide.

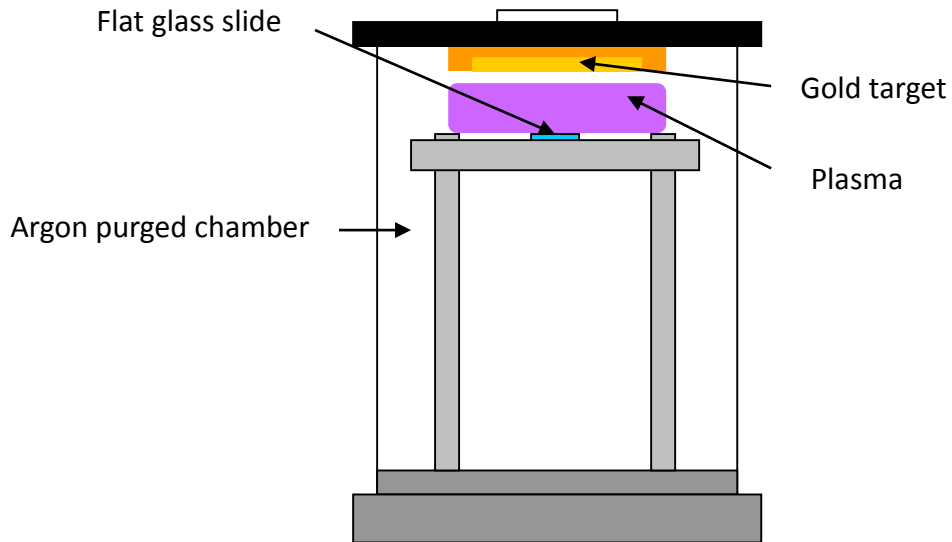


**Fig. 4.2. Schematic diagram of sputtering system for coating gold mirror on the glass substrate.**

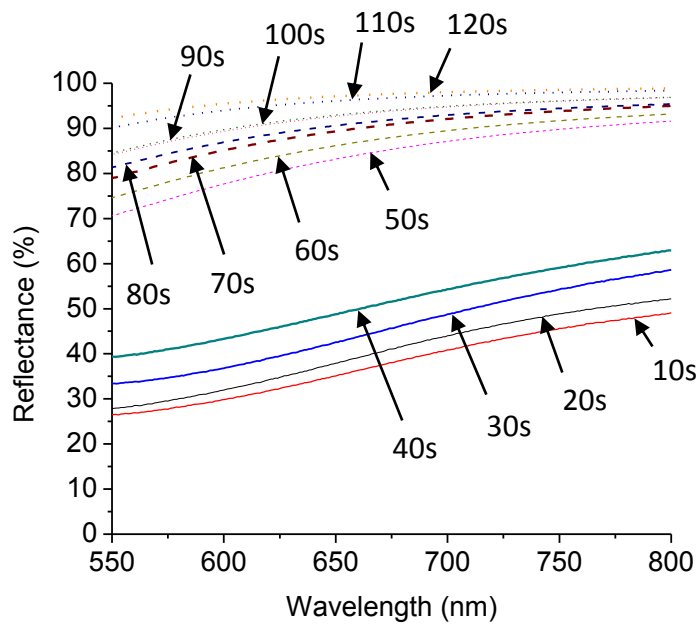


**Fig. 4.3. Spectral reflectance of sputtering deposition time from 10s to 120s.**

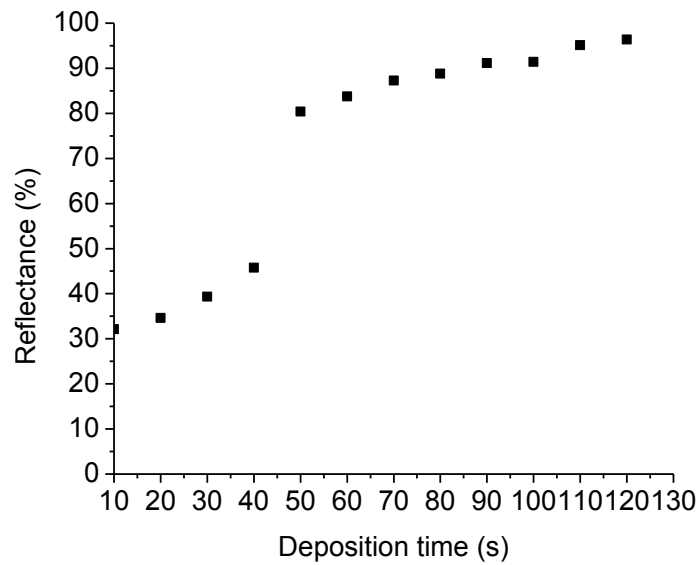


**Fig. 4.4. Reflectance at 623nm of gold mirror on glass substrate as a function of sputtering deposition time.**

Since the emission wavelength of the dye-doped cladding POF was 623nm, the reflectance at 623nm plotted as a function of sputtering deposition time is shown in Fig. 4.4. It can be seen that reflectivity larger than 90% could be obtained after 80 seconds of sputtering deposition time. The maximum reflectance of 96% was obtained for deposition time of 120 seconds. This deposition time was used in the subsequent experiments.

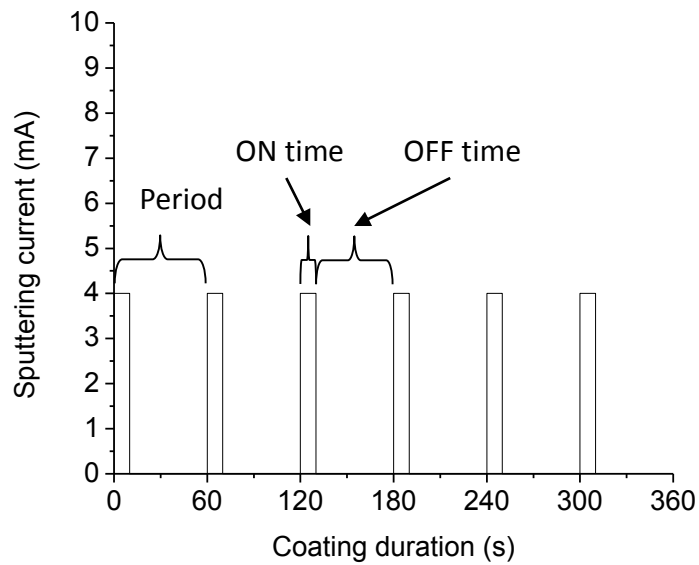


**Fig. 4.5. Sputtering profile for gold coating on the dye-doped fiber end.**

As seen in Fig. 4.1, the fiber end-face is very close to the sputtering target, the fiber end-face will be damaged by the energetic target atoms during sputtering at normal condition. To avoid this damage, a low current and repeated sputtering method was adopted. The gold coating process was divided into several periods, and each period consists of 10 seconds of coating time (sputtering is turned on) and 50 seconds of cooling time (sputtering is turned off). In other words, for 60 seconds of coating time, it was divided into 6 coating periods, and each period consists of 10 seconds of coating time (coating is turned on) and 50 seconds of cooling time (coating is turned off). The profile of coating process was shown in Fig. 4.5. This deposition technique was adopted in all experiments of this research work.

### 4.2.3 Study of emission characteristics of Rh640-dye-doped POF with both end-faces coated with gold mirrors

In this section, the emission performance of the dye-doped POF with integrated optical cavity, that is both fiber end-faces were coated with gold mirrors using the coating method described in section 4.2.2, was investigated. Five dye-doped POF with 5 cm long were prepared. One fiber end-face of each sample, acted as a cavity

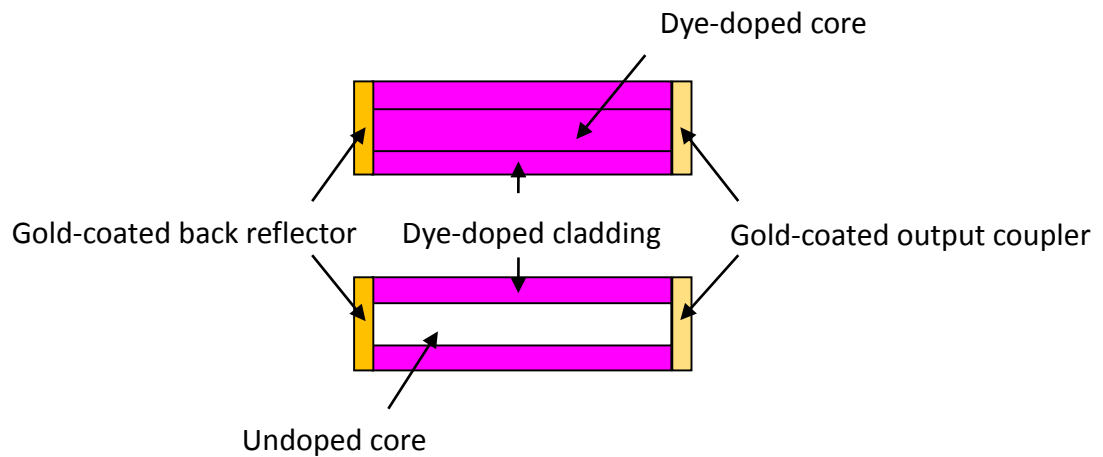


**Fig. 4.6. Schematic diagram of Rh640 doped cladding polymer optical fiber.**

reflector, was coated with gold mirror of 96% reflectance. Other fiber end-faces, acted as an output coupler, were coated with gold mirror of reflectance, 30%, 40%, 80%, and 90% respectively, and the fiber end-face of the fifth one did not coated with gold mirror. The schematic diagram of the dye-doped POFs with optical cavities is illustrated in Fig. 4.6.

The dye-doped POF was transversely optically pumped at 532nm by a frequency-doubled Q-switched Nd:YAG laser (Quanta-Ray GCR-16S, Spectra-Physics). The laser pulse width was  $\sim 6$ ns, and the repetition rate was set at 2.5Hz. The pumping power was varied by adjusting the Q-switch delay. The laser spot was expanded by a beam expander. A cylindrical lens was then used to focus the expanded laser spot into a thin stripe to illuminate the dye-doped POF. The output power of the dye-doped POF was measured by a power meter (Thorlabs PM100) with a silicon photodiode (Thorlabs S121B). The schematic diagram of the experimental set-up used in the present investigation is shown in Fig. 4.7.

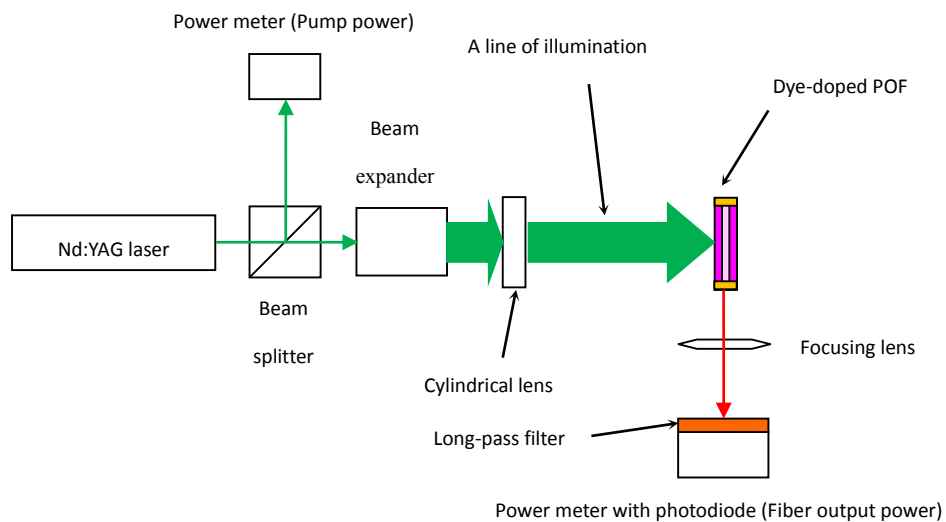


**Fig. 4.7. Experimental set-up for lasing performance characterization of Rh640-dye-doped POF.**

Fig. 4.8 shows the plots of the output power measured from the output coupler as a function of pump power for dye-doped core POFs and undoped core POFs with different reflectance  $R$  of gold mirror coated on the output coupler. For all plots, the output power grew slowly at low pump power for both types of POF. This is mainly due to the spontaneous emission of the organic dyes as their populations of excitation state are less than that of the ground state. Therefore as the pump power was further increased, the population of excitation state increased correspondingly. When the pump power was further increased and close to the laser-like threshold, population inversion occurred, and the spontaneous emission of the organic dyes was amplified. At pump power beyond the laser-like threshold, the output power increased dramatically, and this is mostly attributed to the occurrence of amplified spontaneous emission (ASE). It can also be seen in Fig. 4.8(b) to 4.8(e) that the laser-like threshold increased with the reflectance  $R$  of gold mirror coated on the output coupler.

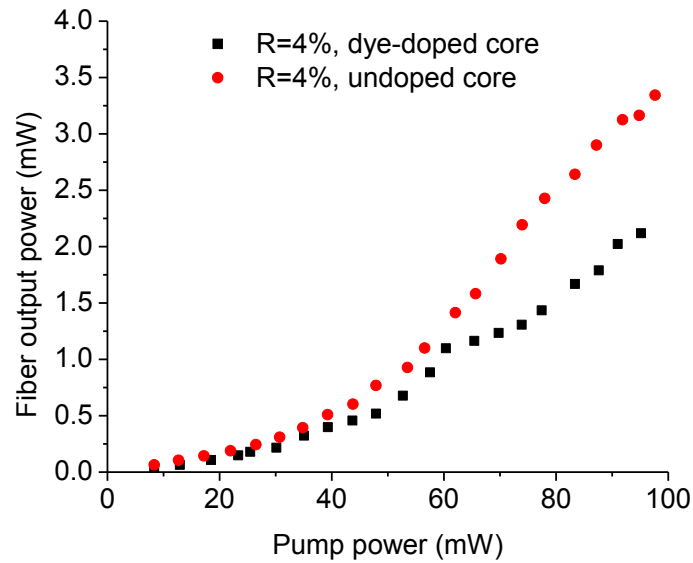


**Fig. 4.8(a). The fiber output power as a function of pump power for Rh640-dye-doped core POF and undoped core POF without gold mirror coated on the output coupler.**

It can be seen from Fig. 4.8(a) that for output coupler without gold mirror (i.e. assume 4% of reflectance), the output power of undoped core POF is much higher than that of dye-doped core POF at the pump power beyond the laser-like threshold. It is clear that for the undoped core POF the emitted light encounters only an optical attenuation loss in the core whereas the emitted light propagating in the core of dye-doped core POF experiences a relatively higher optical loss due to the combination of attenuation in the core material and absorption and scattering by the highly doped dye molecules. Although the emitted light is amplified by the

dye molecules when they propagated along the gain medium in the core, the total optical loss is still higher than the gain in the optical cavity.

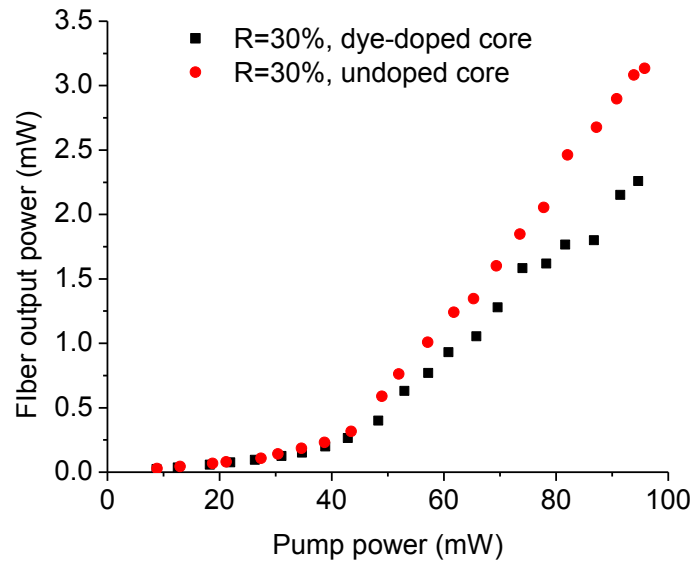


**Fig. 4.8(b). The fiber output power as a function of pump power for Rh640-dye-doped core POF and undoped core POF with gold mirror of 30% reflectance coated on the output coupler.**

As is shown in Fig. 4.8(b), when the reflectance of the output coupler was highly increased to 30%, the output power of undoped core POF was still larger than that of the dye-doped core POF at high pump power beyond the laser-like threshold. But it was lower compared with that of 4% reflectance while the output power of dye-doped core POF remained nearly unchanged. This is because the confined emitted

lights reflect multiple times in the undoped optical cavity in which they show higher attenuation loss, less light come out from the output coupler thereof. For the dye-doped core POF, however, the optical loss is still very high as is the case for 4% reflectance.

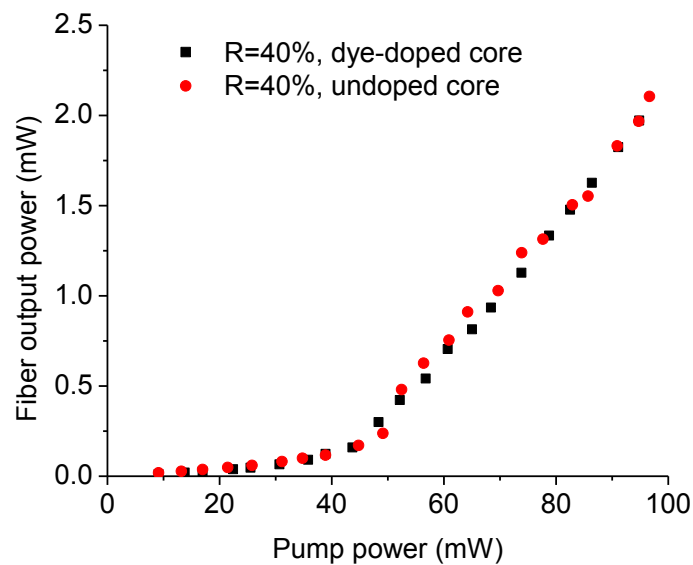


**Fig. 4.8(c). The fiber output power as a function of pump power for Rh640-dye-doped core POF and undoped core POF with gold mirror of 40% reflectance coated on the output coupler.**

However, when the reflectance was gradually increased to 40%, as shown in Fig. 4.8(c), both output powers of undoped and dye-doped core POFs were exactly the same. Although the total loss in the dye-doped core POF seems larger than that in

the undoped core one, it was completely balanced by the optical gain obtained through amplification by the dye due to more lights reflected back to the fiber when reflectance was increased to 40%.

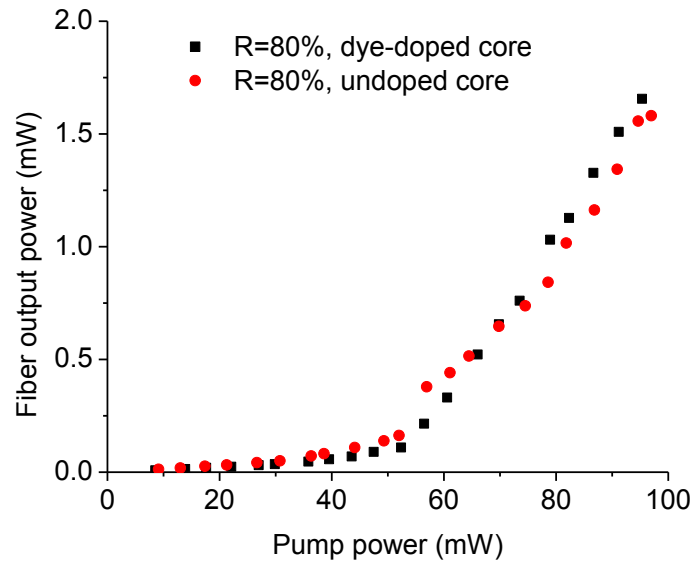


**Fig. 4.8(d). The fiber output power as a function of pump power for Rh640-dye-doped core POF and undoped core POF with gold mirror of 80% reflectance coated on the output coupler.**

As the reflectance was significantly increased to 80%, Fig. 4.8(d) indicates that the output powers of both types of POF decreased accordingly, but the output power of dye-doped core POF was slightly higher than that of undoped core POF. This probably reflects the fact that more emitted lights can be reflected back into the optical cavity and then get amplified with high reflectance of the output coupler

such that the optical gain starts to increase and is higher than the total loss in the optical cavity of the dye-doped core POF.

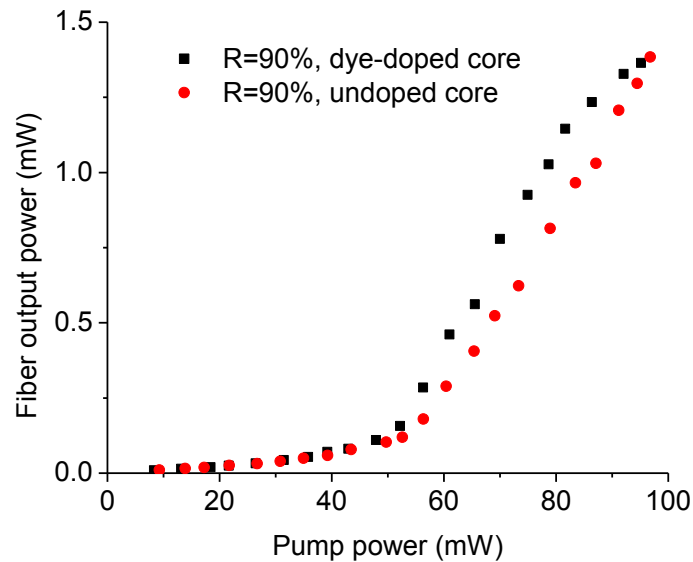


**Fig. 4.8(e). The fiber output power as a function of pump power for Rh640-dye-doped core POF and undoped core POF with gold mirror of 90% reflectance coated on the output coupler.**

Fig. 4.8(e) reveals that the output power of dye-doped core POF was obviously greater than that of undoped core POF at the pump power beyond the laser-like threshold when the reflectance of output coupler was further increased to 90%. It is obvious that more lights are reflected by the high reflective output coupler back into the gain medium, where they are amplified. In other words, the gain is much higher than the total optical loss in the optical cavity of the dye-doped core POF,

and a net optical gain is then obtained. However, the output power of dye-doped core POF could not maintain a linear increase at very high pump power. It gradually saturates with the pump power while the undoped core POF does not show the saturation.

#### **4.2.4 Conclusion**

All these interesting findings illustrate that the dye-doped POF with integrated optical cavity shows an emission characteristic with a laser-like threshold. Moreover, the reflectance of gold mirror coated directly on the output coupler has great effects on the emission performances of POFs with dye-doped core and POFs with undoped core. It is clear that POF with undoped core has superior emission performance when a relatively low reflectance of gold mirror is coated on the output coupler or no gold mirror coated on the output coupler to form an optical cavity.

On the other hand, the results indicate that although the core is heavily doped with organic dye as a gain medium for the amplification of the emitted light from the dye-doped cladding, the optical loss is very high which results from the high concentration of dye. To solve this problem, it is suggested that the fiber structure

of slightly low doping concentration of organic dye in the core and relatively high doping concentration of dye in the cladding may attain a net optical gain in the core.

### **4.3 Effect of dye concentration in core of Rh640-dye-doped POF on emission characteristics**

#### **4.3.1 Fabrication**

To maintain an acceptable level of output power used in optical system, an optical cavity is formed by a gold coated fiber end-face with 96% reflectance and uncoated fiber end-face. A POF structure of low doping concentration in the core and high doping concentration in the cladding is adopted. In this section, the effect of dye concentration in the core of dye-doped POF on the emission characteristics is presented.

In this study, a step-index dye-doped POF was drawn from a preform produced by the casting/moulding method as described in chapter 3. The preform has an inner diameter and an outer diameter of 10mm and 22mm respectively. The inner cylindrical core was made of copolymer of methyl methacrylate (MMA) and Benzyl methacrylate (BzMA) in mole ratio of 75 to 25. The outer tubular cladding was

made of pure MMA. The calculated refractive indexes of the core and cladding are 1.5135 and 1.4904 respectively. Four different kinds of preforms were prepared. All the claddings were doped with 200ppm Rh640 (Exciton) organic laser dye. The cores of three POF samples were doped with 200ppm, 50ppm, and 20ppm dye respectively. A POF sample with an undoped core was used to serve as a reference and a control sample. Another POF sample with 20ppm of Rh640-doped core and undoped cladding of poly methyl methacrylate (PMMA) was also fabricated for comparison. Each fiber has an outer diameter of  $\sim 950\mu\text{m}$ , and a core diameter of  $\sim 430\mu\text{m}$ .

The dye-doped POF was cut into 5cm long pieces, and their end-faces were polished to optical grade by hand using fiber polishing sheets of  $6\mu\text{m}$ ,  $3\mu\text{m}$  and  $1\mu\text{m}$  grit size in turn. As shown in Fig. 4.9, one fiber end-face was then coated with a gold layer of reflectance of 96% using the method described in section 4.2.2. This acted as a back reflector. The other polished end-face acted as an output coupler.

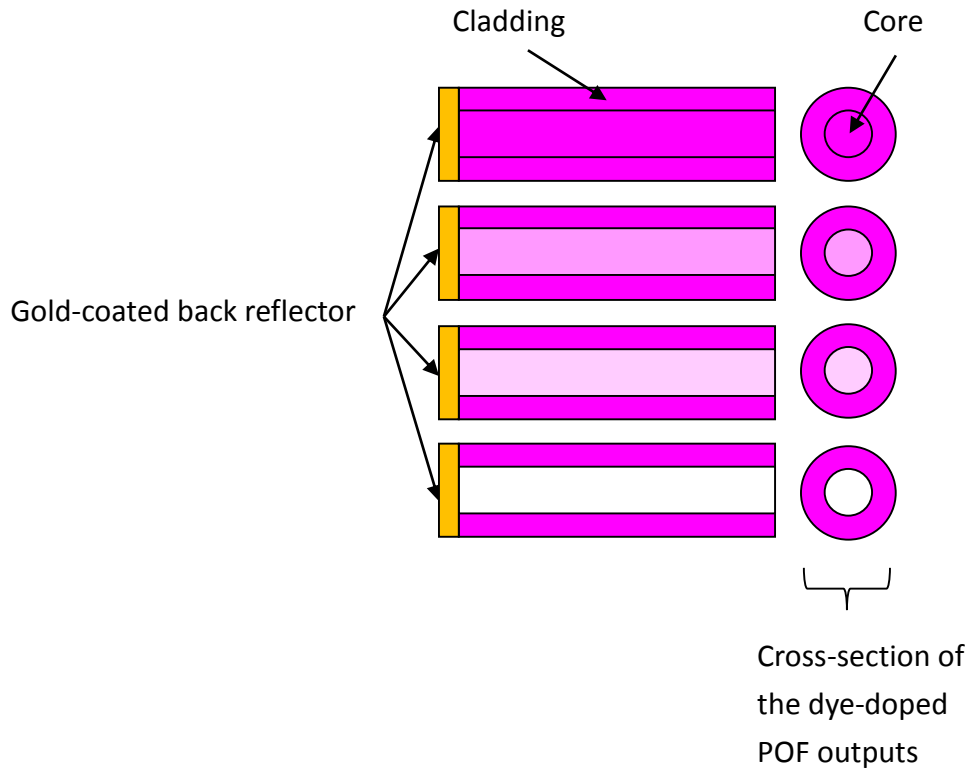


**Fig. 4.9. Schematic diagram of step-index POFs with cladding doped with 200ppm Rh640 dye, and cores doped with 200ppm, 50ppm, 20ppm and 0ppm Rh640 dye (top to bottom).**

### 4.3.2 Experiment

The experimental set-up used to investigate the lasing output power and emission spectrum of the POF is shown in Fig. 4.7 and Fig. 4.10, respectively. The dye-doped POF was transversely pumped at 532nm by a frequency-doubled Q-switched Nd:YAG pulse laser (Spectra-Physics, Quanta-Ray GCR-16S). The laser pulse width was ~6ns, and the repetition rate was set at 2.5Hz. The pumping power was varied by adjusting the Q-switch delay. The laser spot was expanded by a beam expander.

A cylindrical lens was then used to transform and focus the expanded laser spot into a thin rectangular-like stripe to illuminate the whole length of the dye-doped POF. The output power of pump laser and the dye-doped POF were monitored and measured by a power meter (Coherent, LabMax-Top) and a power meter (Newport, 2936-C) with a silicon photodiode (Newport, 918D-UV-OD3), respectively. A long-pass filter was used to remove the pump light. The emission spectrum was then obtained by a collecting fiber and spectrometer (Ocean Optics, HR4000). The spectral resolution is 0.2nm.

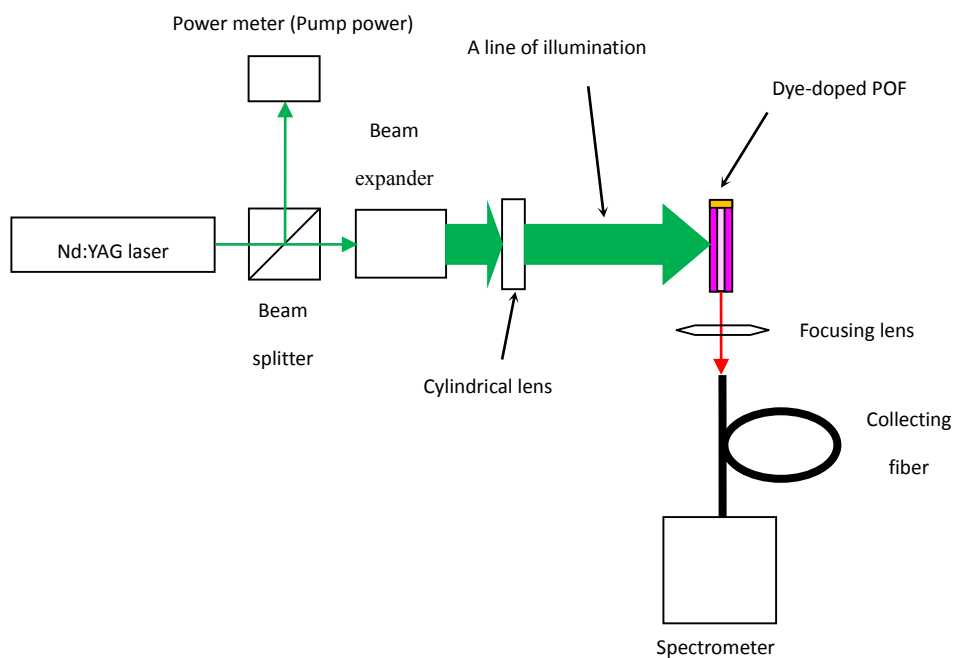


**Fig. 4.10. Experimental set-up for lasing spectra characterization of dye-doped**

**POF.**

The operation of side-pumped step-index dye-doped POF laser is that when a stripe of pump laser light (532nm) irradiates on the dye-doped cladding, the organic laser dyes are excited and the emitted light (642nm) is then coupled into and guided in the core. At the same time, some pump laser light penetrates the cladding and into the core, thus excites the organic laser dye in the core.

Fig. 4.11 shows the plots of the output power measured from the four dye-doped POFs as a function of pump power for 200ppm, 50ppm, 20ppm Rh640-doped core POFs, and an undoped core POF, all with 200ppm Rh640-doped cladding. A plot of POF with 20ppm Rh640-doped core and undoped cladding was also included for comparison. For all plots, the output power grew slowly at low pump power for all the POFs. This is mainly due to the spontaneous emission of the organic dyes as their populations of excitation state are less than that of the ground state. As the pump power was increased, the population of excitation state increased correspondingly. When the pump power was further increased and close to the laser-like threshold, population inversion occurred, and the spontaneous emission of the organic dyes was amplified. At pump power beyond the laser-like threshold, the output power increased dramatically, and this is mostly attributed to the amplified spontaneous emission (ASE). It can also be seen in Fig. 4.11, the 200ppm

dye-doped core POF has the lowest output power among the dye-doped core POFs tested, which is even lower than that of the undoped core POF. In the undoped core POF, the emitted lights from the cladding encounter only the optical attenuation loss owing to scattering in the core material, whereas the emitted lights from the cladding propagating in the core of 200ppm dye-doped core POF experience a relatively higher optical loss due to the absorption and scattering by the dye molecules and core material respectively. It is worth noting that, although the emitted lights from the dyes (in core and/or cladding) were amplified when they propagated along the gain medium in the core, the total optical loss is still higher than the gain in the optical cavity leading to low fiber output power. To reduce the optical loss in the dye-doped POF core, the concentration of dye doped in the core was reduced to 50ppm and 20ppm. It was found that a significant increase in the fiber output power was observed for doping concentrations of 50ppm and 20ppm as shown again in Fig. 4.11. It can also be seen that the maximum fiber output power of the POF with 20ppm dye-doped core and 200ppm dye-doped cladding is higher and that the laser-like threshold is lower than that of the 20ppm dye-doped core only POF. It is clear that low doping concentration of organic dye in the core can attain a net optical gain in the core and that doping the cladding with dye can improve the performance significantly. At 80mW pump

power, the fiber output power increased from 3mW to 5mW whereas the laser-like threshold decreased from about over 40mW to less than 20mW.

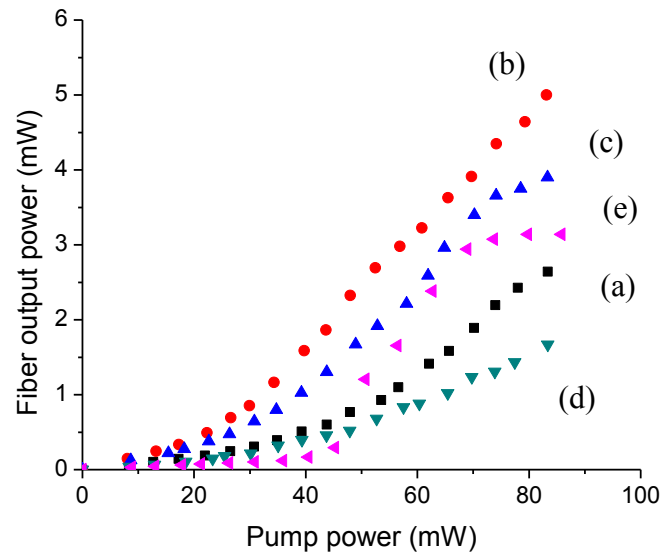


**Fig. 4.11. The output power as a function of pump power for POFs: (a) Core: undoped, Cladding: 200ppm Rh640-dye-doped, (b) Core: 20ppm Rh640-dye-doped, Cladding: 200ppm Rh640-dye-doped, (c) Core: 50ppm Rh640-dye-doped, Cladding: 200ppm Rh640-dye-doped, (d) Core: 200ppm Rh640-dye-doped, Cladding: 200ppm Rh640-dye-doped, and (e) Core: 20ppm Rh640-dye-doped, Cladding: undoped.**

### **4.3.3 Emission spectra of POF with 20ppm Rh640-dye-doped core and 200ppm Rh640-dye-doped cladding**

Next, the emission spectrum and photostability of the 20ppm dye-doped core POF were studied. Fig. 4.12 shows the emission spectra of 20ppm dye-doped core POF with 200ppm dye-doped cladding at various pump power. Fig. 4.12(a) shows the fluorescence emission spectrum of dye-doped POF at the pump power of 9.5mW. As the pump power is further increased, the emission spectrum narrows with linewidth (full width at half maximum, FWHM) of 42nm below the laser-like threshold down to 20nm above the laser-like threshold, as shown in Fig. 4.12(c) and Fig. 4.12(d), respectively. The linewidth further narrows down to about 10nm at pump power of 57.6mW, as shown in Fig. 4.12(f), where amplified spontaneous emission occurs. The corresponding emission linewidth for each pump power is illustrated in Fig. 4.13. It can be seen in Fig. 4.13 that the laser-like threshold is about 30mW.

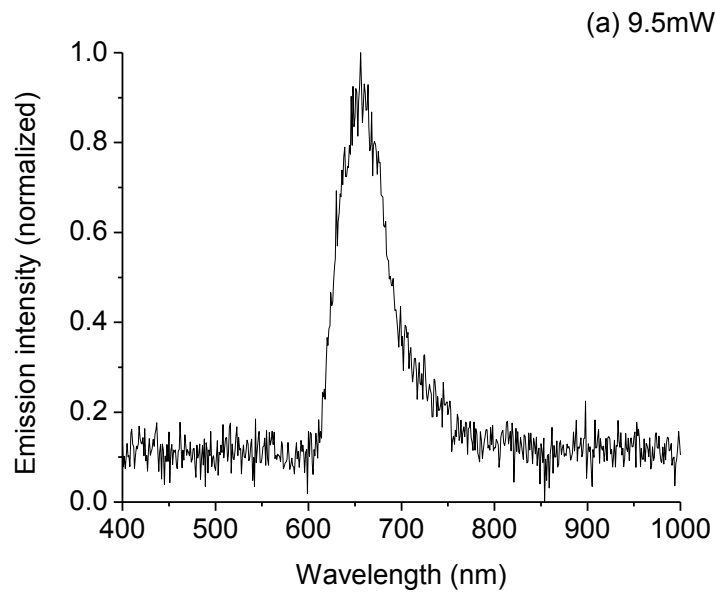


**Fig. 4.12(a).** Emission spectrum of 20ppm Rh640-dye-doped core POFs with 200ppm Rh640-dye-doped cladding at a pump power of 9.5mW.

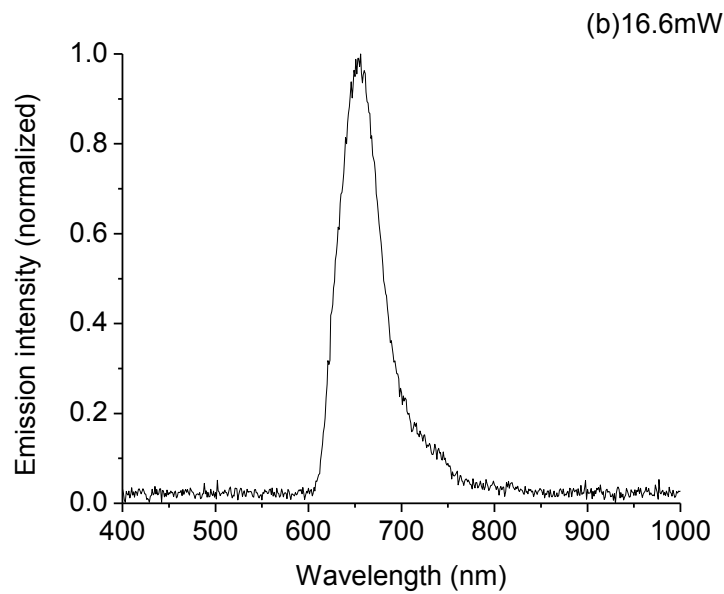


**Fig. 4.12(b).** Emission spectrum of 20ppm Rh640-dye-doped core POFs with 200ppm Rh640-dye-doped cladding at a pump power of 16.6mW.

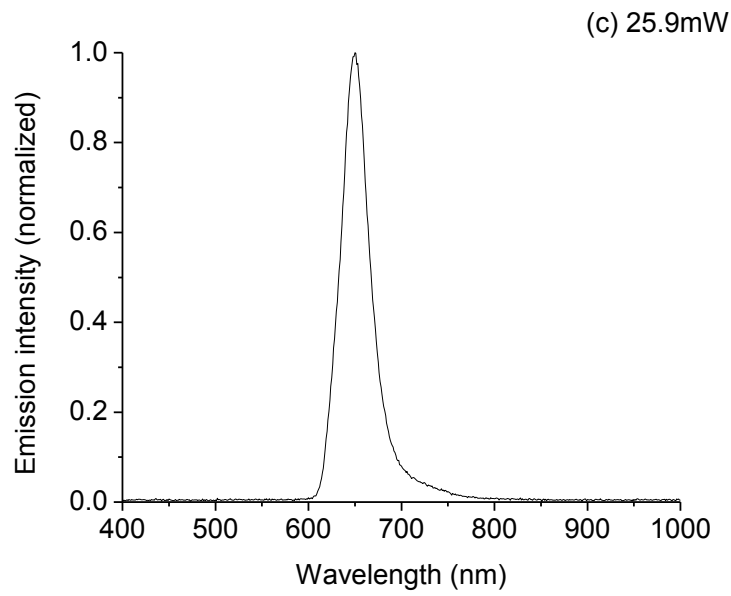


**Fig. 4.12(c).** Emission spectrum of 20ppm Rh640-dye-doped core POFs with 200ppm Rh640-dye-doped cladding at a pump power of 25.9mW.

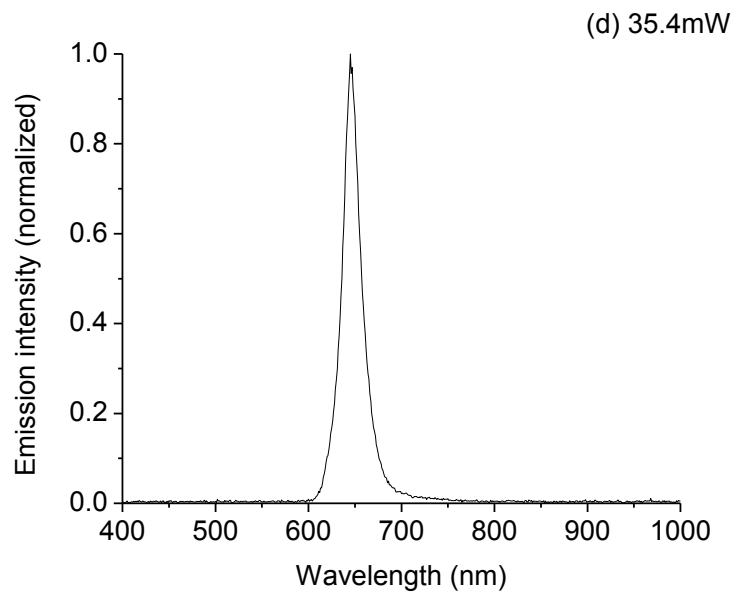


**Fig. 4.12(d).** Emission spectrum of 20ppm Rh640-dye-doped core POFs with 200ppm Rh640-dye-doped cladding at a pump power of 35.4mW.

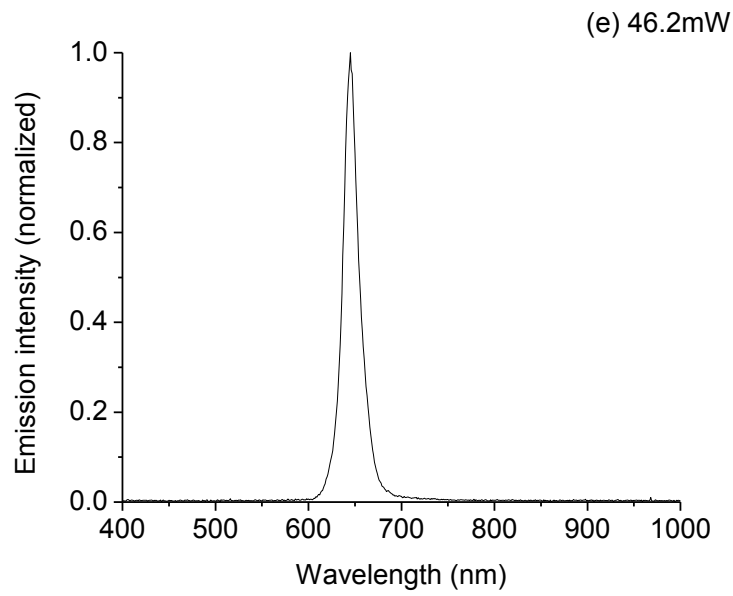


**Fig. 4.12(e).** Emission spectrum of 20ppm Rh640-dye-doped core POFs with 200ppm Rh640-dye-doped cladding at a pump power of 46.2mW.

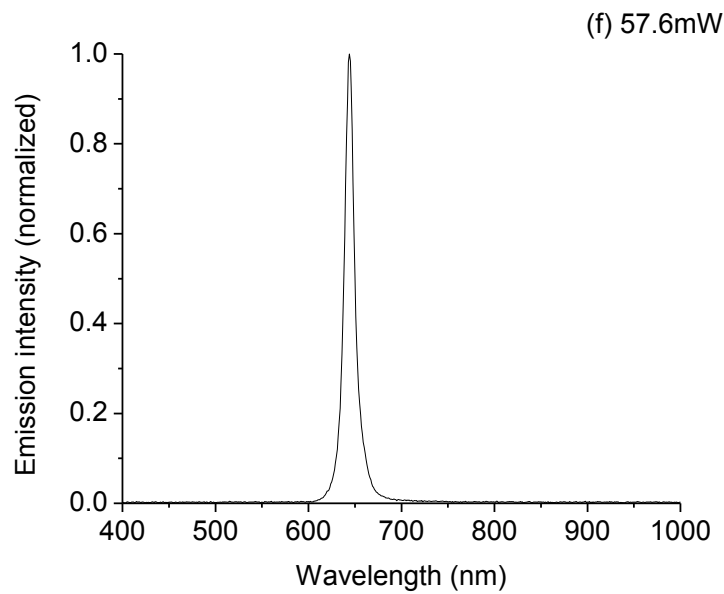


**Fig. 4.12(f).** Emission spectrum of 20ppm Rh640-dye-doped core POFs with 200ppm Rh640-dye-doped cladding at a pump power of 57.6mW.

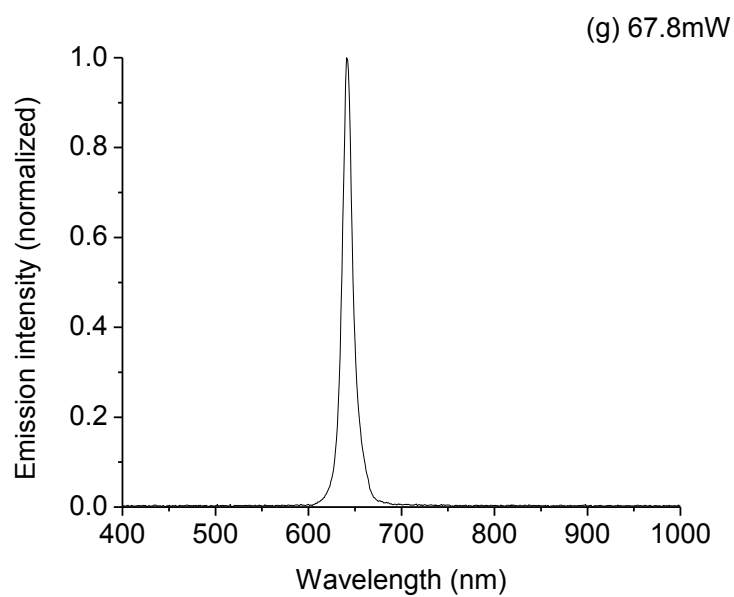


**Fig. 4.12(g).** Emission spectrum of 20ppm Rh640-dye-doped core POFs with 200ppm Rh640-dye-doped cladding at a pump power of 67.8mW.

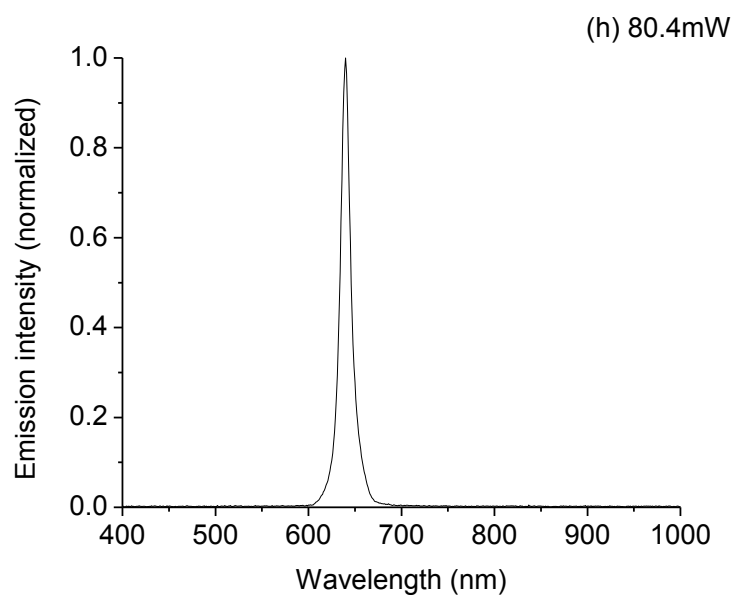


**Fig. 4.12(h).** Emission spectrum of 20ppm Rh640-dye-doped core POFs with 200ppm Rh640-dye-doped cladding at a pump power of 80.4mW.

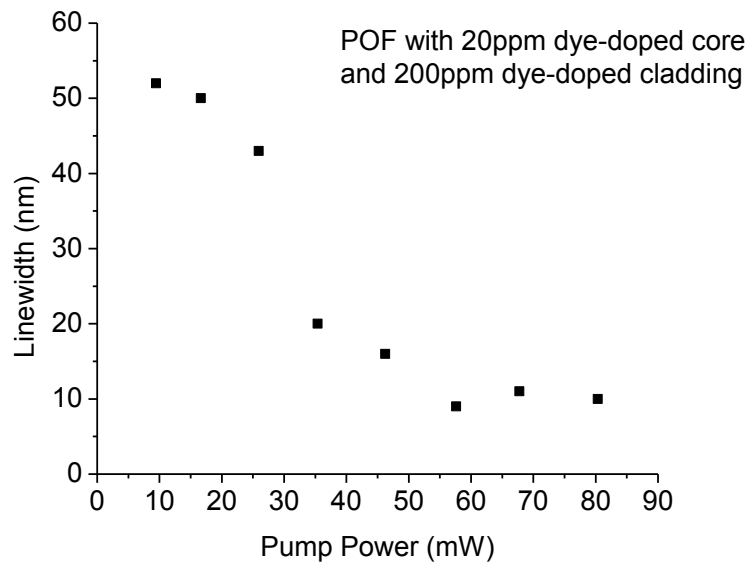


**Fig. 4.13.** The emission linewidth of 20ppm Rh640-dye-doped core POF with 200ppm Rh640-dye-doped cladding as a function of pump power.

#### 4.3.4 Photostability

Finally, we study the photostability of the side-pumped dye-doped POF. A sample of the same fiber is continuously pumped by the Nd:YAG laser pulse of 56mW at a repetition rate of 2.5Hz. Fig. 4.14 shows the temporal spectrum of output pulse chain of the 20ppm Rh640-dye-doped core POF with 200ppm Rh640-dye-doped cladding at pump power of 56mW. The observed pulse duration (FWHM) is limited to 2.7ms by the resolution of the measuring equipment. The figure is just used to

demonstrate the pulse form of the fiber output. The lifetime measurement was carried out at room temperature without external cooling.

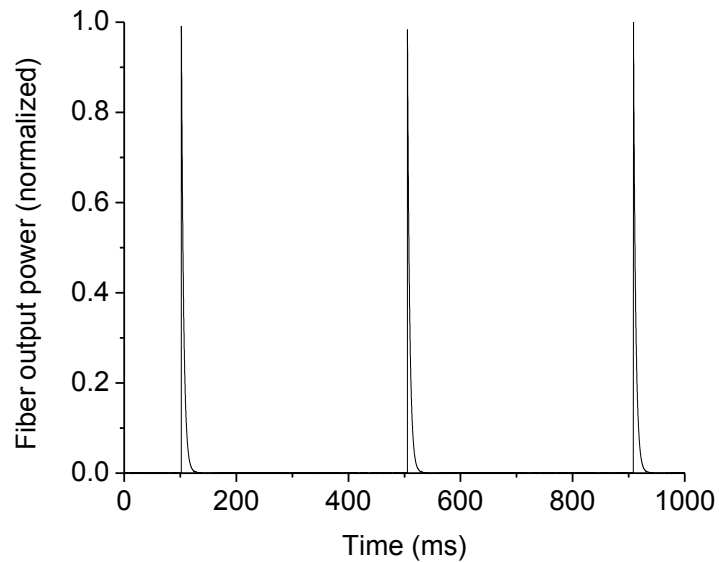


**Fig. 4.14. The temporal spectrum of the output pulse chain of 20ppm Rh640-dye-doped core POF with 200ppm Rh640-dye-doped cladding. It is just used to demonstrate the pulse form of output.**

The photostability of dye-doped POF with pumping time is plotted in Fig. 4.15. It can be seen that the fiber output power was reduced to a half of the initial value after 7 hours which is equal to 60,000 pulses. As shown in Fig. 4.16., although the number of pulses of our SI POF fiber laser is lower than that of the GI POF fiber laser in [2], it is still higher than that of copolymer bulk fiber laser in [2].

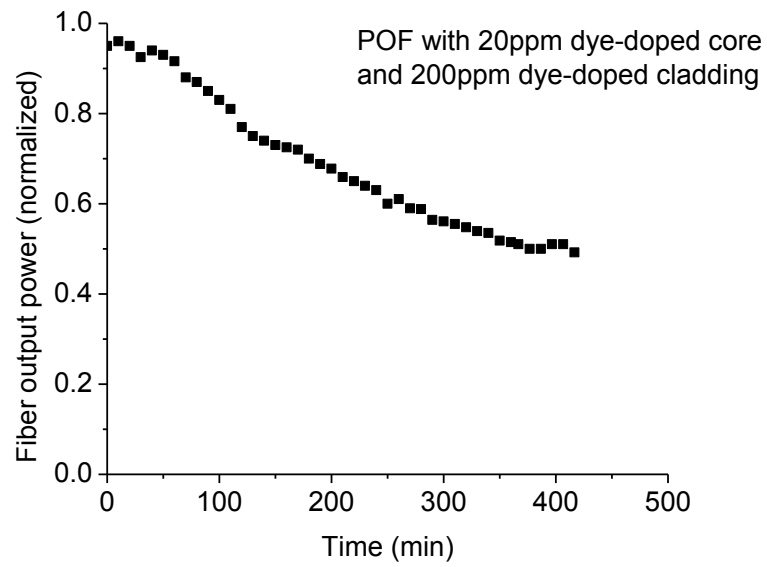


**Fig. 4.15. Photostability of 20ppm Rh640-dye-doped core POF with 200ppm Rh640-dye-doped cladding with pumping time.**

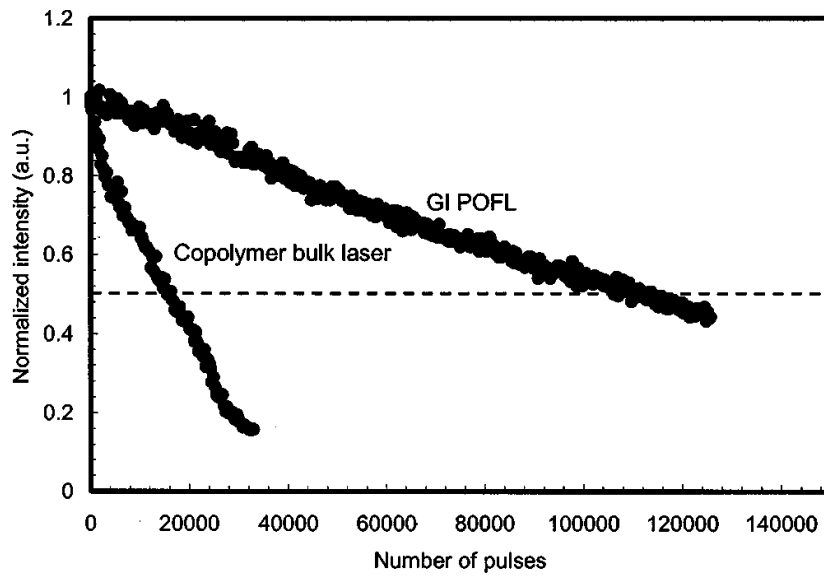


**Fig. 4.16. Degradation of laser energy output of the GI POFL and copolymer bulk laser with number of pulses [2].**

### **4.3.5 Conclusion**

A simple and integral step-index Rh640-perchlorate-dye-doped POF using a lightly dye-doped core and relatively highly dye-doped cladding was fabricated, and the ASE behavior of side pumping the POF was investigated and demonstrated. An external optical conversion efficiency of 6% was obtained, and an emission linewidth of 10nm was observed. A maximum fiber output power of 5mW at emission wavelength of 642nm has been achieved. These results indicated that with suitable fiber structural design and concentration of organic dopants, side-pumped dye-doped POFs can be potentially used as fiber pulse ASE light source operated in the visible region in area of optical communication and medical imaging or diagnosis uses. Further investigations are currently carried out in the POFs doped with various organic laser dyes.

### **4.4 Reference**

1. K. Kuriki, T. Kobayashi, N. Imai, T. Tamura, Y. Koike, and Y. Okamoto, "Organic dye-doped polymer optical fiber laser", *Polym. Adv. Technol.*, Vol. 11, 612 (2000)

2. K. Kuriki, T. Kobayashi, N. Imai, T. Tamura, S. Nishihara, Y. Nishizawa, A. Tagaya, Y. Koike, and Y. Okamoto, "High-efficiency organic dye-doped polymer optical fiber lasers", *Appl. Phys. Lett.*, Vol. 33, 331 (2000)
3. M. Sheeba, K. J. Thomas, M. Rajesh, V. P. N. Nampoori, C. P. G. Vallabhan, and P. Radhakrishnan, "Multimode laser emission from dye doped polymer optical fiber", *Appl. Opt.*, Vol. 44, 8089 (2007)

## CHAPTER 5

### POF Random Lasers

#### 5.1 Introduction

In this chapter, the fabrication process and emission characterization of a multimode POF random laser with coherent and resonant feedback is demonstrated experimentally. The gain medium was a solid Rh640-perchlorate-dye-doped polymer fiber core, and the optical feedback was provided by the multiple scattering of light between TiO<sub>2</sub> nanoparticles dispersed in the core. It was found that the POF random laser emission spectrum exhibited discrete narrow lasing linewidths when focused optical pumping above lasing threshold. The phenomenon behaved similar to conventional multimode lasers. This experimental observation confirmed that recurrent scattering of light not only lengthen the travelling path of light but also prolong the dwelling time of light in the active medium, thus enhancing the light amplification by stimulated emission with coherent and resonant feedback.

## 5.2 Fabrication of random lasers

The amplifying disordered system used in our experiment is POF containing Rh640 perchlorate dyes and TiO<sub>2</sub> nanoparticles. The Rh640 perchlorate dyes are to provide the gain, and the TiO<sub>2</sub> nanoparticles are used as the scatterers. The concentration of Rh640 perchlorate dyes is 800ppm or about 1.3mM. The TiO<sub>2</sub> (DuPont, Ti-Pure R-900) nanoparticles have a median diameter of 410nm. The particle density of the nanoparticles is 400ppm or about  $1.62 \times 10^{10} \text{ cm}^{-3}$ .

A step-index Rh640 perchlorate dyes and TiO<sub>2</sub> nanoparticles co-doped POF was made by drawing a preform produced by the casting/moulding method as stated in Chapter 3. The preform has an inner diameter and an outer diameter of 10mm and 22mm respectively. The inner cylindrical core was made of copolymer of MMA and BzMA in mole ratio of 75 to 25. The outer tubular cladding was made of pure MMA. The core materials were prepared, in a flask, by mixing 800ppm Rh640 perchlorate dyes in MMA and BzMA monomers solution until the dye was completely dissolved, then 400ppm TiO<sub>2</sub> powder was introduced in the laser dye-monomers solution provided that the mixture was viscous enough. This important step was to ensure that the TiO<sub>2</sub> nanoparticles could be distributed uniformly in the dye-doped monomers mixture before they went to the bottom of the mixture. The core

mixture was stirred until it became more viscous and then poured into the hole of a PMMA tube. The preform then underwent bulk polymerization process inside an oven. After several days, the preform was drawn into fibers with outer diameter of  $\sim 1004\mu\text{m}$ , and a core diameter of  $\sim 456\mu\text{m}$ .

The dyes and nanoparticles co-doped POF was cut into 5cm-long pieces, and their end-faces were polished to optical grade. As shown in Fig. 5.1, one fiber end-face that was then coated with gold mirror of reflectance 96% by the method mentioned in Chapter 4, acted as a back reflector, and another end-face acted simply as an output coupler. The white color dots represent the  $\text{TiO}_2$  nanoparticles randomly distributed in the Rh640-perchlorate-dye-doped core.

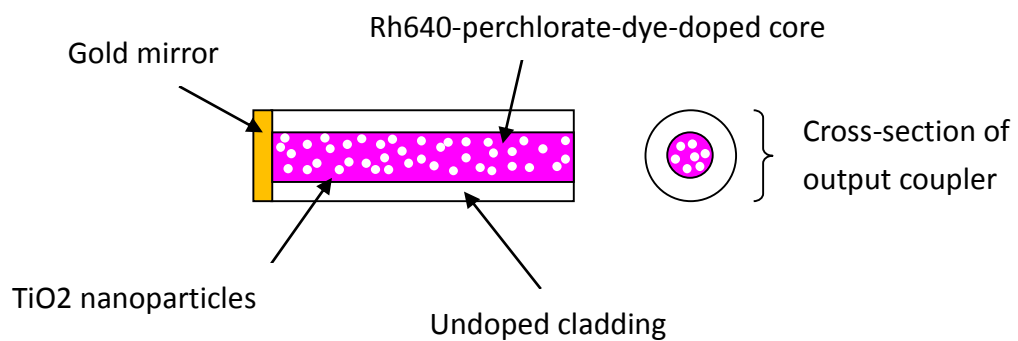


**Fig. 5.1. Schematic diagram of the POF containing 800ppm (1.3mM) Rh640 perchlorate dye (magenta color) and 400ppm ( $1.62 \times 10^{10} \text{ cm}^{-3}$ )  $\text{TiO}_2$  nanoparticles (white dots).**

## **5.3 Emission spectra characterization of random lasers**

In this section, the experimental results on the emission characteristics of POF containing Rh640 dye and TiO<sub>2</sub> nanoparticles are presented. Next, the lasing modes analysis is performed.

### **5.3.1 Lasing spectra of dye-doped POF without nanoparticles**

To distinguish the effect of scatterers in the lasing action of POF random lasers, a dye-doped POF without nanoparticles was prepared. The evolution of the emission spectra of the dye-doped POF with single-shot pumping power were shown in Fig. 5.2. At the pump power of 12.6mW, a broad fluorescence peak occurred, due to the spontaneous emission of the dye molecules. When the pump power increased to 26.4mW, the emission spectrum started to narrow down with the pump power. At high pump power, only an ASE occurred. The spectral linewidth of the discrete lasing peaks and ASE peak is illustrated in Fig. 5.3. The linewidth of the ASE is 53nm at low excitation power, and then dramatically narrows down to 4.5nm at high excitation power. A laser-like threshold is also observed at about 12mW.

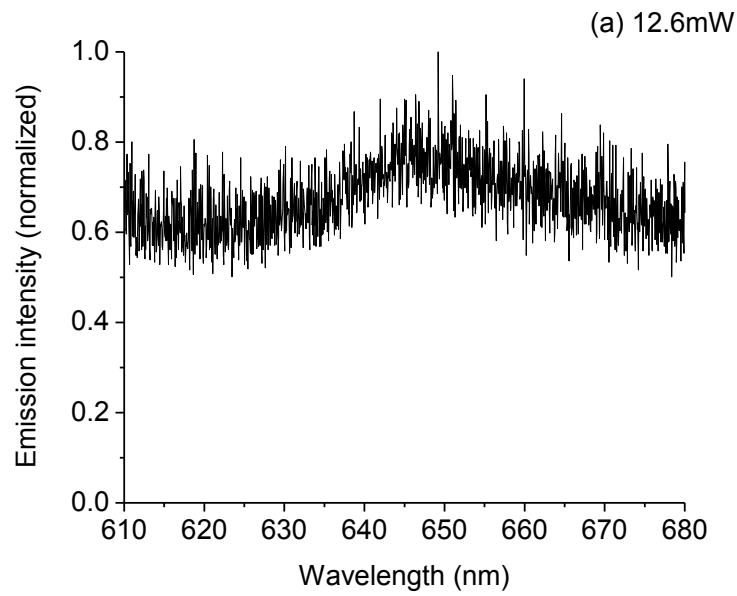


**Fig. 5.2(a). Emission spectrum of dye-doped POF without nanoparticles for incident pump power of 12.6mW.**

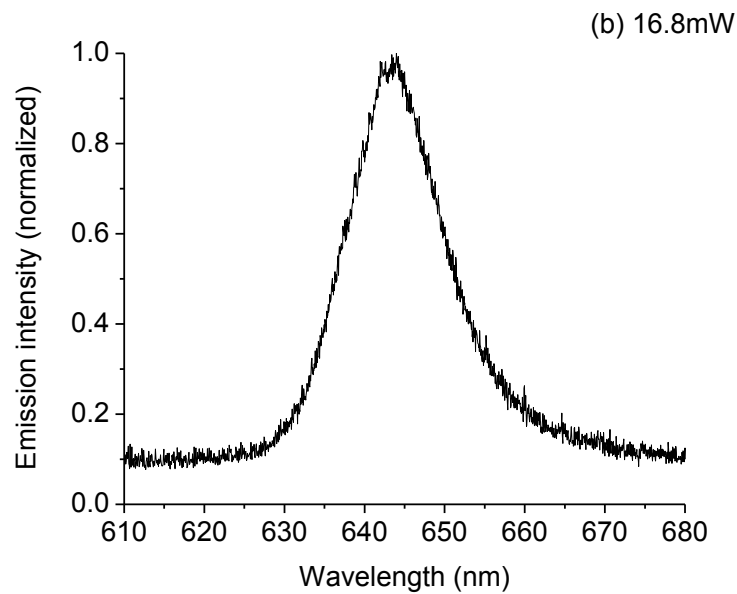


**Fig. 5.2(b). Emission spectrum of dye-doped POF without nanoparticles for incident pump power of 16.8mW.**

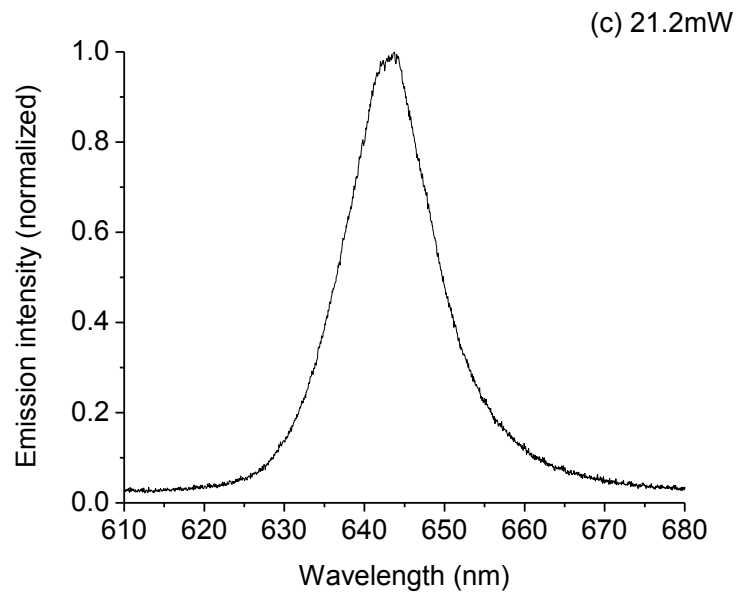


**Fig. 5.2(c). Emission spectrum of dye-doped POF without nanoparticles for incident pump power of 21.2mW.**

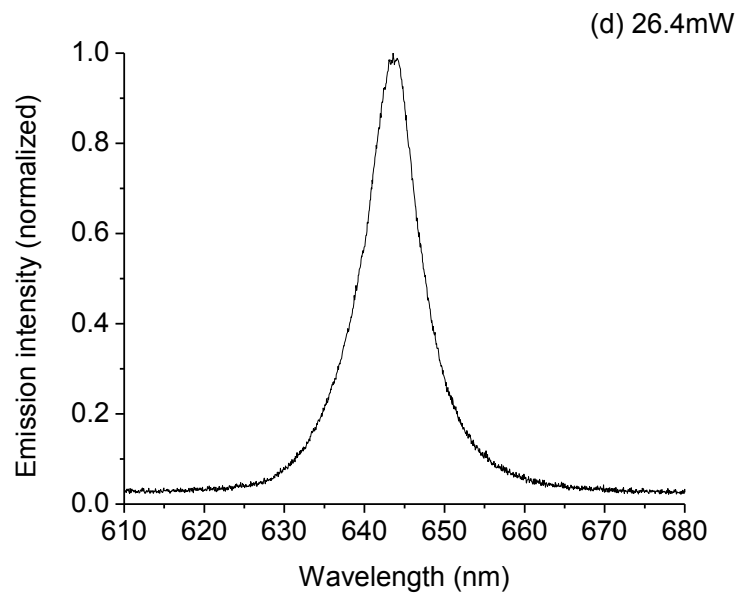


**Fig. 5.2(d). Emission spectrum of dye-doped POF without nanoparticles for incident pump power of 26.4mW.**

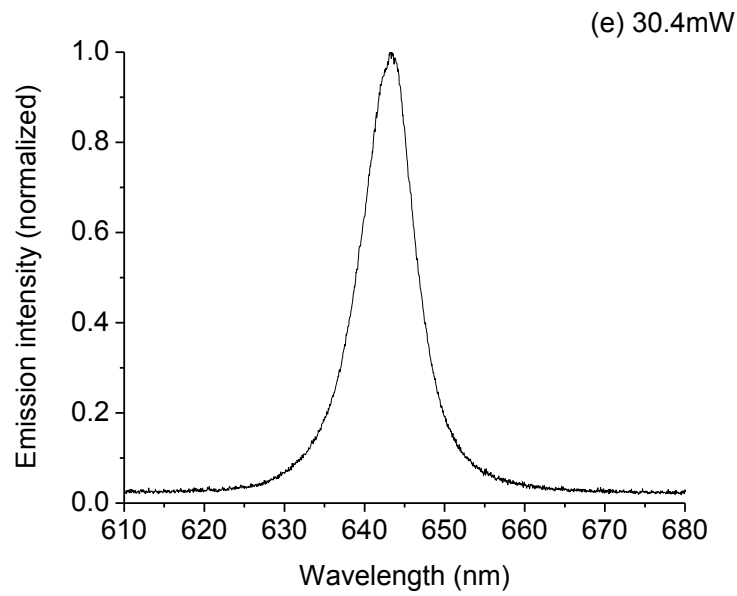


**Fig. 5.2(e). Emission spectrum of dye-doped POF without nanoparticles for incident pump power of 30.4mW.**

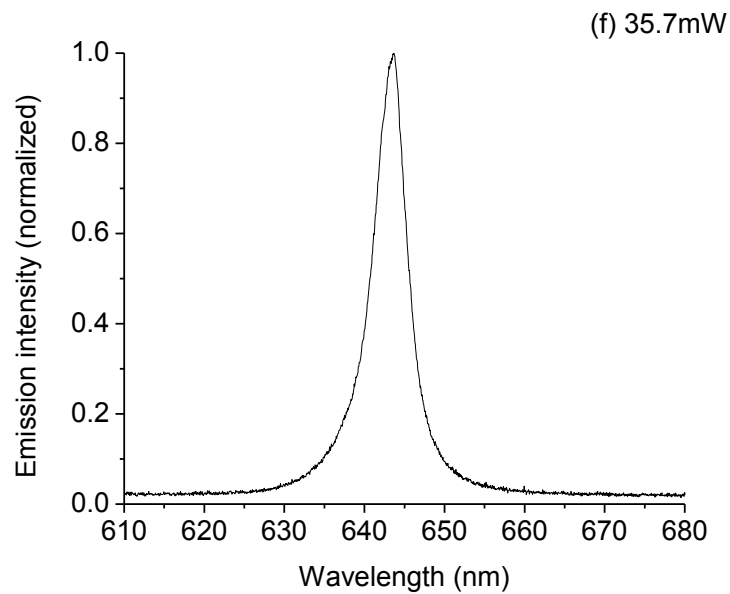


**Fig. 5.2(f). Emission spectrum of dye-doped POF without nanoparticles for incident pump power of 35.7mW.**

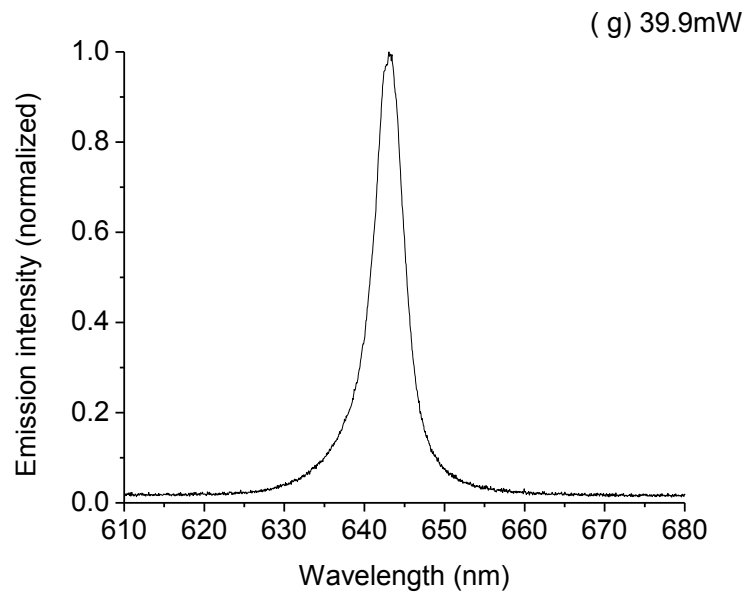


**Fig. 5.2(g). Emission spectrum of dye-doped POF without nanoparticles for incident pump power of 39.9mW.**

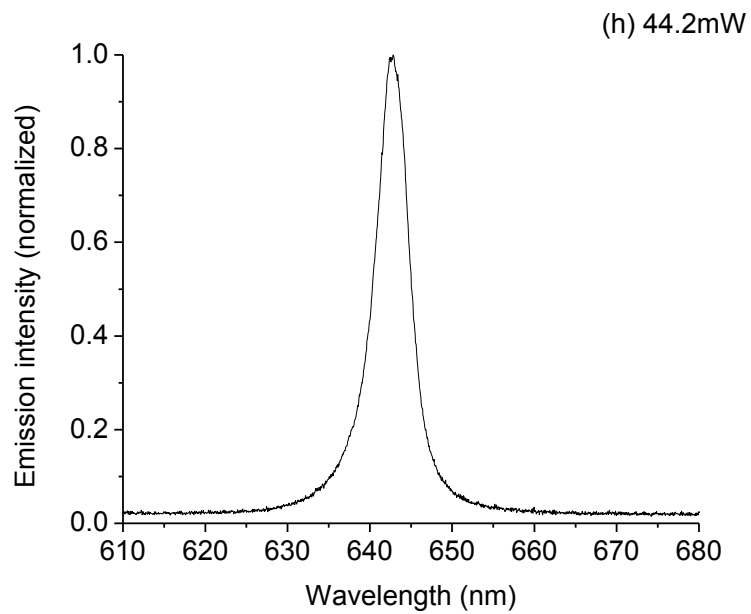


**Fig. 5.2(h). Emission spectrum of dye-doped POF without nanoparticles for incident pump power of 44.2mW.**

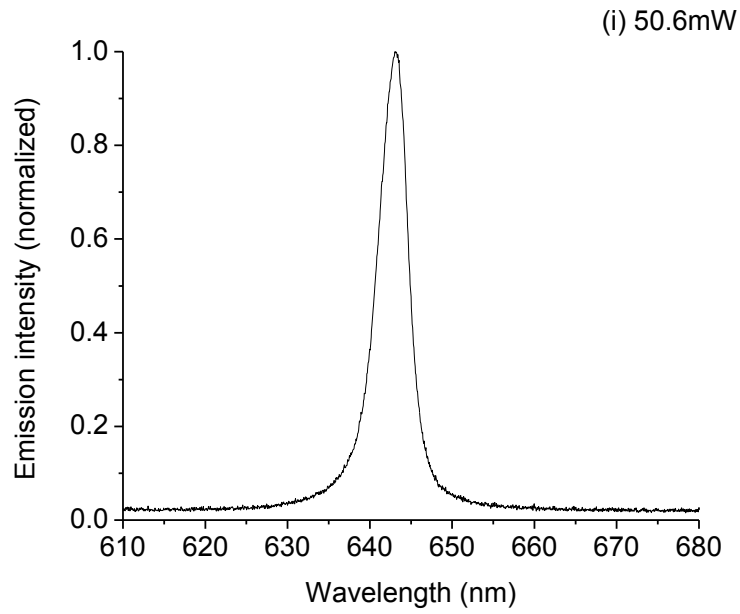


**Fig. 5.2(i). Emission spectrum of dye-doped POF without nanoparticles for incident pump power of 50.6mW.**

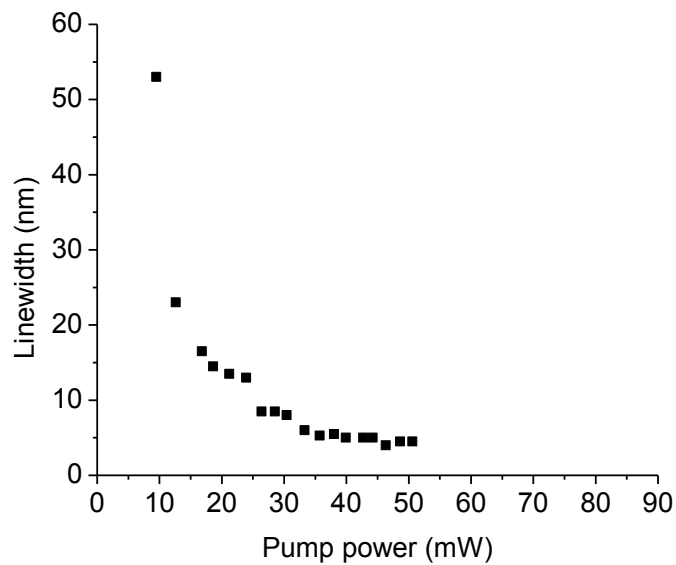


**Fig. 5.3. Spectral linewidth of the emission in the dye-doped POF lasing spectrum with pump power.**

### 5.3.2 Laser action in POF random lasers

Since the average particle size of scatterers is of the order of the emission wavelength in the medium, a particle cannot serve as a resonator for lasing. Instead, the resonators are formed by the recurrent light scattering.

The amplifying disordered POF was transversely optically pumped at 532nm by a frequency-doubled Q-switched Nd:YAG pulse laser (Spectra-Physics, Quanta-Ray GCR-16S). The laser pulse width was  $\sim 6$ ns. The pumping power was varied by adjusting the Q-switch delay. The laser spot was expanded by a beam expander. A cylindrical lens was then used to focus the expanded laser spot into a thin stripe to illuminate whole length of the amplifying disordered POF. The experimental set-up used in the random lasing investigation is the same as the one shown in Fig. 4.10 of Chapter 4. The output power of pump laser was monitored by a power meter (Coherent, LabMax-Top) with a thermal-pile detector. The emission spectrum of the amplifying disordered POF was then collected at the fiber output by a collecting fiber to a spectrometer (Ocean Optics, HR4000). The spectral resolution is 0.2nm. A long-pass filter was placed in front of the spectrometer to remove the pump light at pump wavelength.

Fig. 5.4 shows the evolution of the emission spectra of the POF random laser with single-shot pumping power. Table 5.1 shows the peak wavelengths of the discrete narrow lasing modes when the pumping intensity exceeds the lasing threshold.

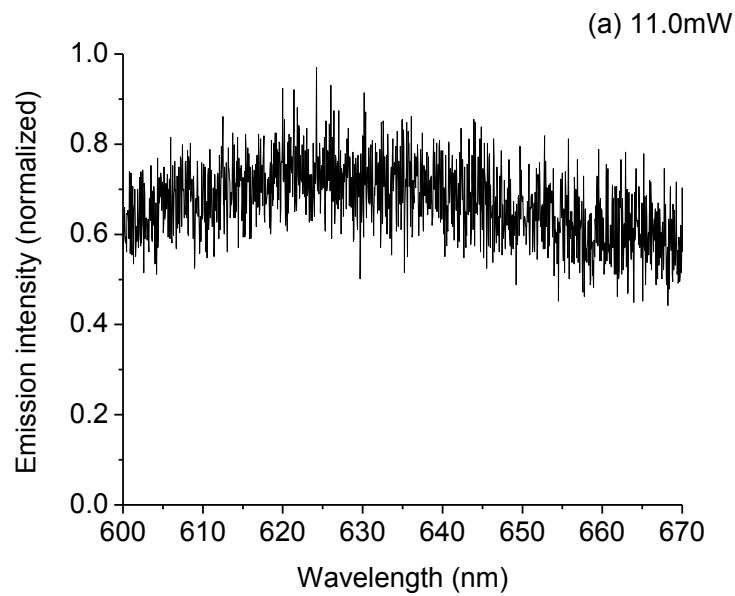


**Fig. 5.4(a). Emission spectrum of POF random lasers for incident pump power of 11.0mW.**

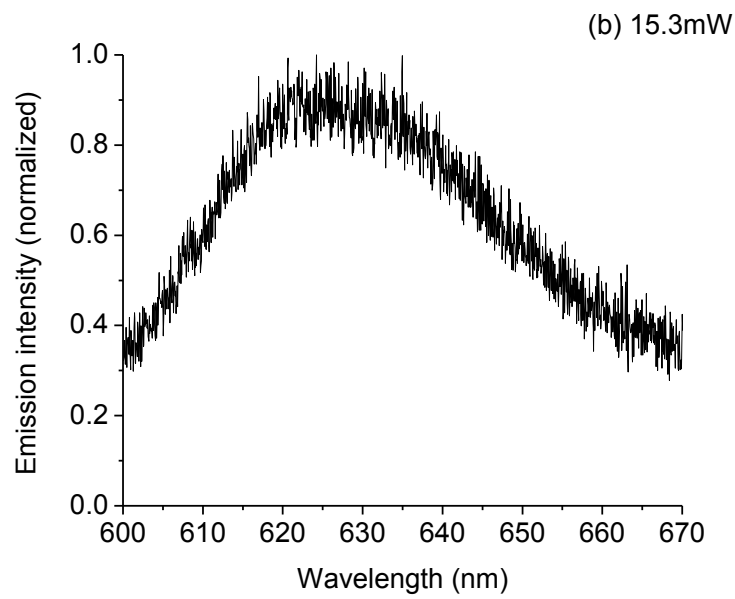


**Fig. 5.4(b).** Emission spectrum of POF random lasers for incident pump power of **15.3mW.**

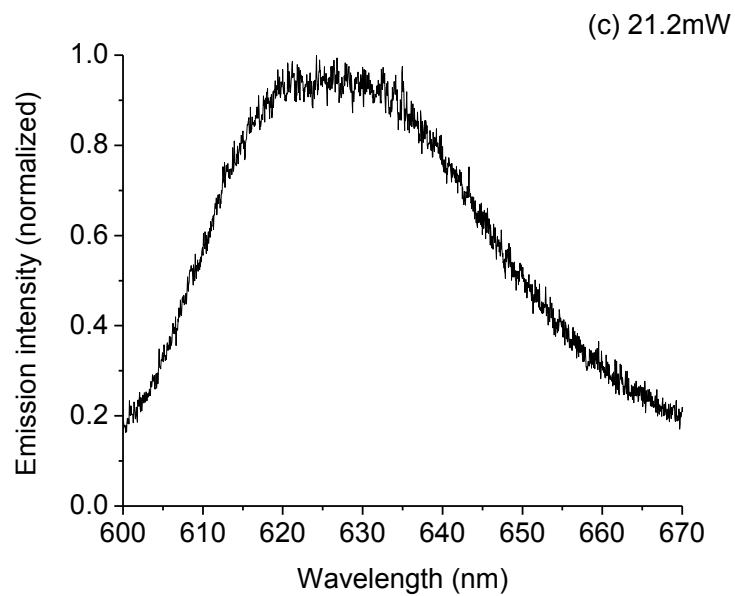


**Fig. 5.4(c).** Emission spectrum of POF random lasers for incident pump power of **21.2mW.**

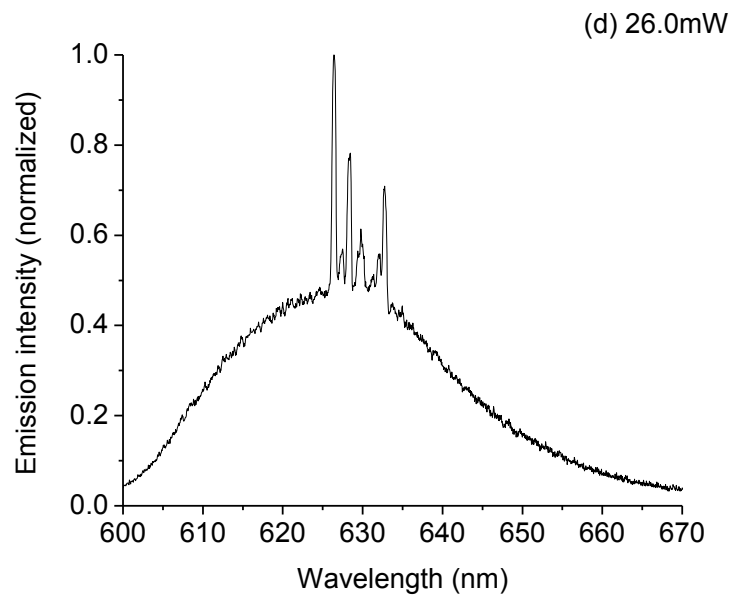


**Fig. 5.4(d). Emission spectrum of POF random lasers for incident pump power of 26.0mW.**

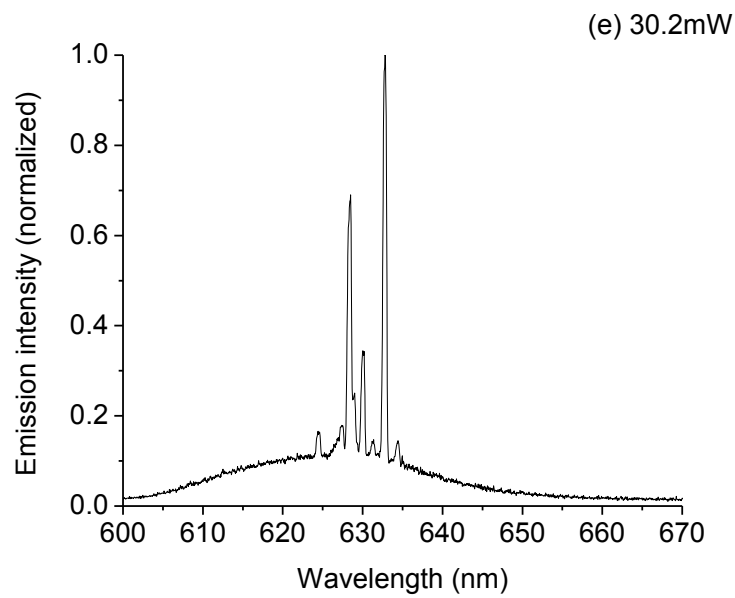


**Fig. 5.4(e). Emission spectrum of POF random lasers for incident pump power of 30.2mW.**

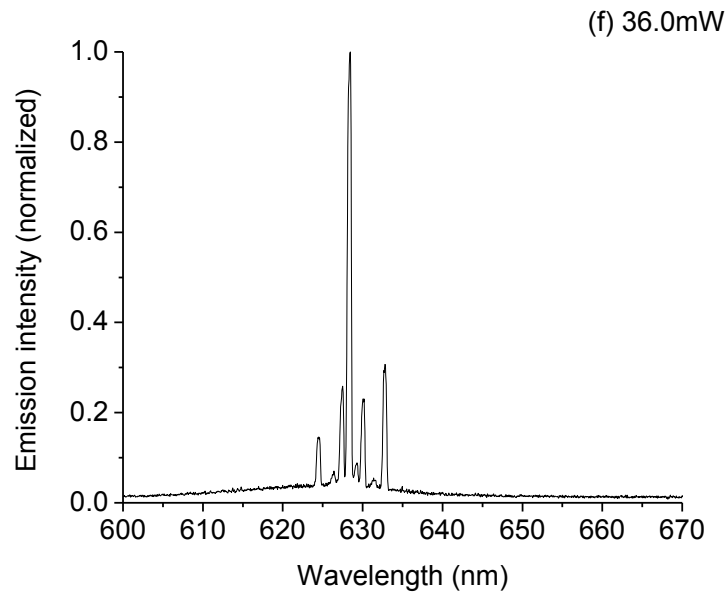


**Fig. 5.4(f). Emission spectrum of POE random lasers for incident pump power of 36.0mW.**

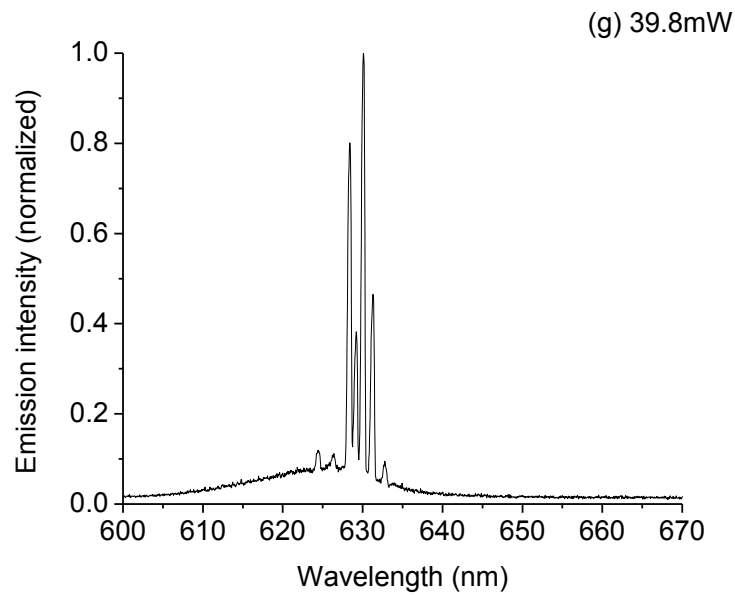


**Fig. 5.4(g). Emission spectrum of POE random lasers for incident pump power of 39.8mW.**

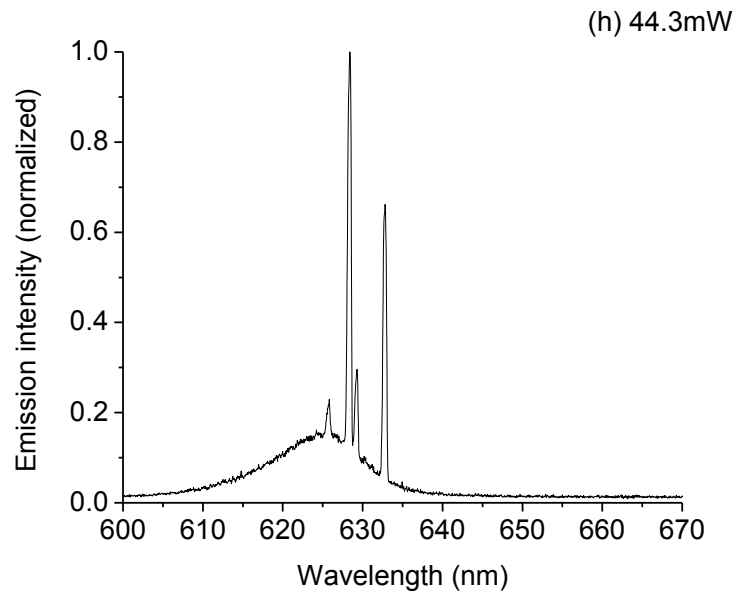


**Fig. 5.4(h).** Emission spectrum of POF random lasers for incident pump power of **44.3mW.**

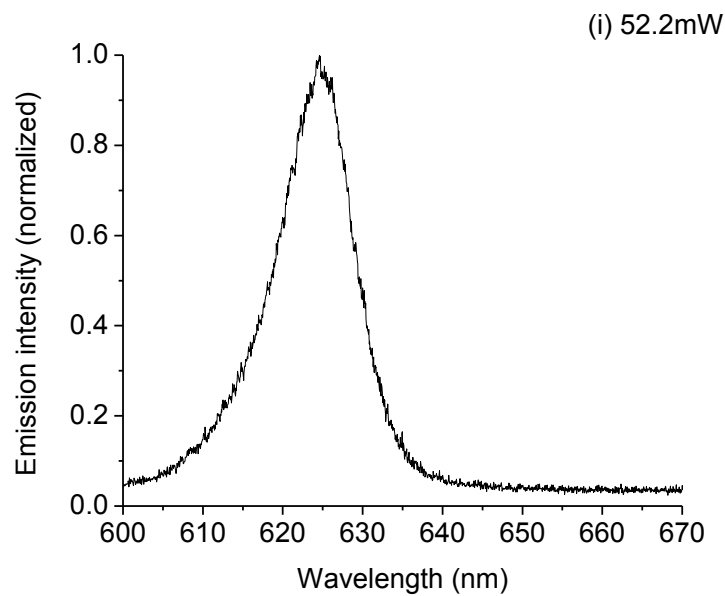


**Fig. 5.4(i).** Emission spectrum of POF random lasers for incident pump power of **52.2mW.**

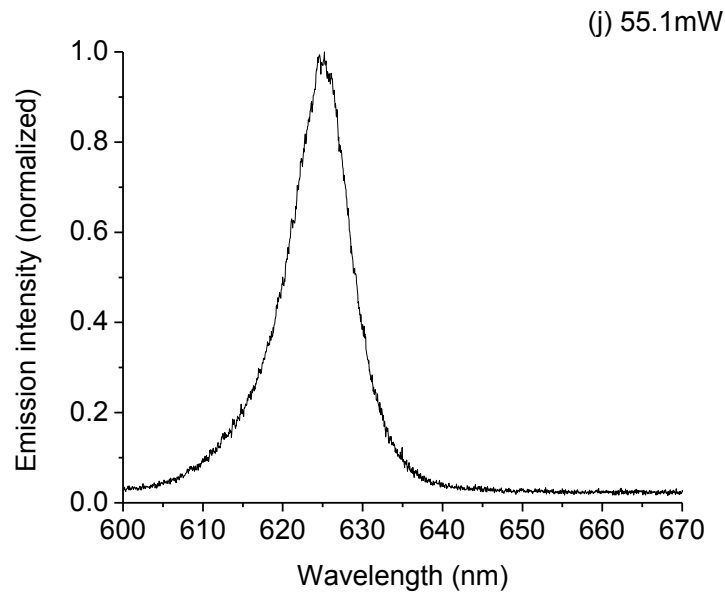


**Fig. 5.4(j).** Emission spectrum of POE random lasers for incident pump power of **55.1mW.**

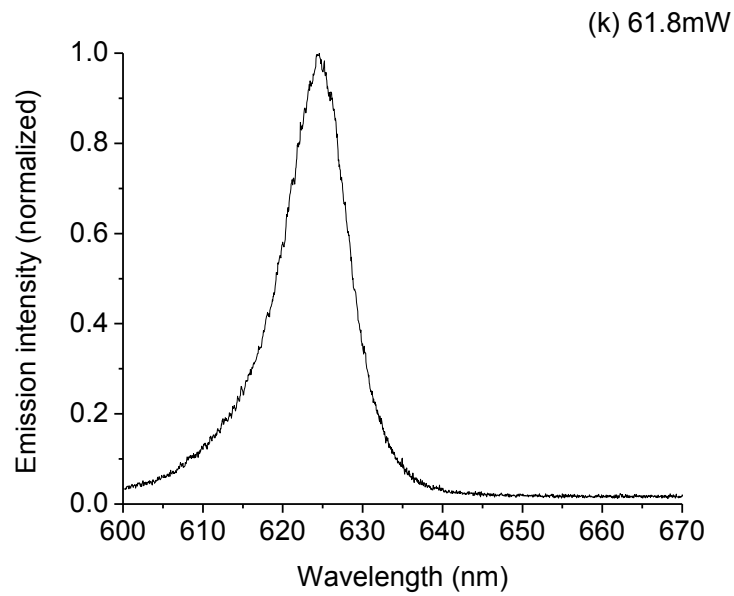


**Fig. 5.4(k).** Emission spectrum of POE random lasers for incident pump power of **61.8mW.**

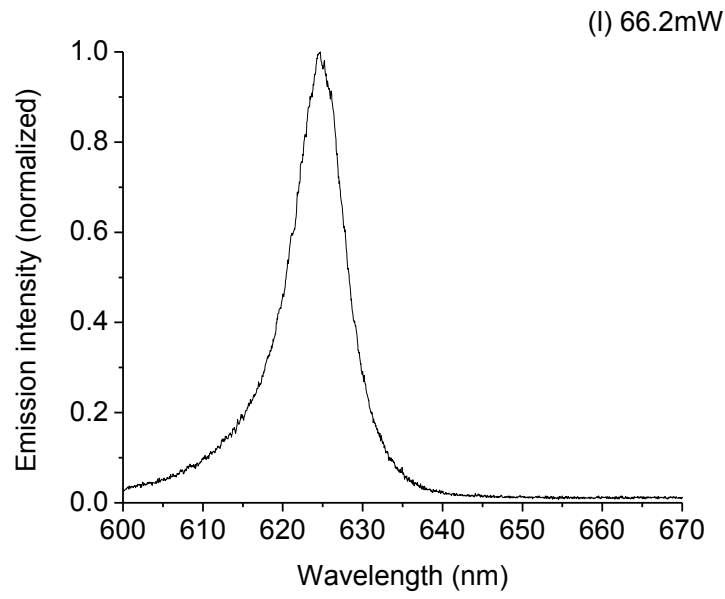


**Fig. 5.4(l). Emission spectrum of POF random lasers for incident pump power of 66.2mW.**

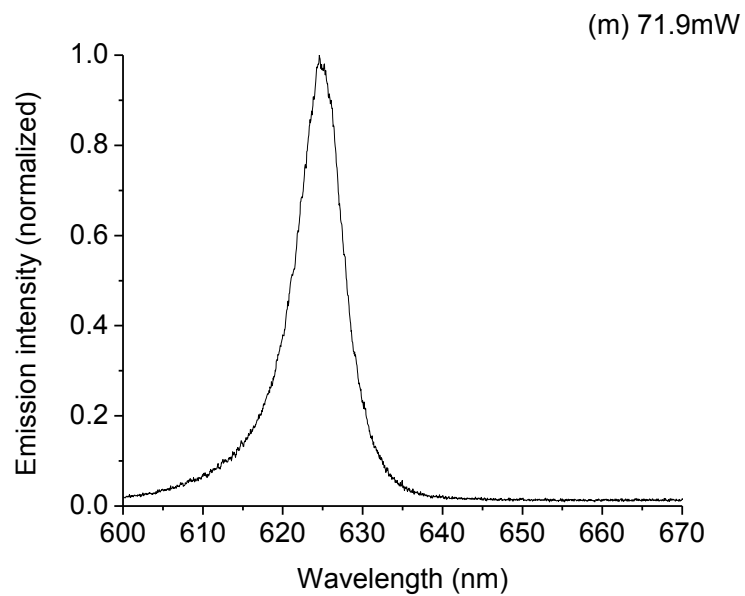


**Fig. 5.4(m). Emission spectrum of POF random lasers for incident pump power of 71.9mW.**

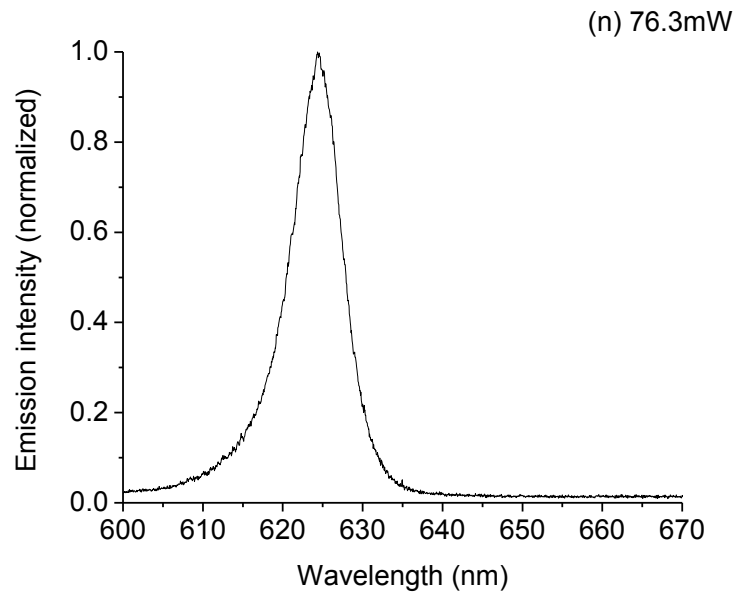


**Fig. 5.4(n). Emission spectrum of POF random lasers for incident pump power of 76.3mW.**

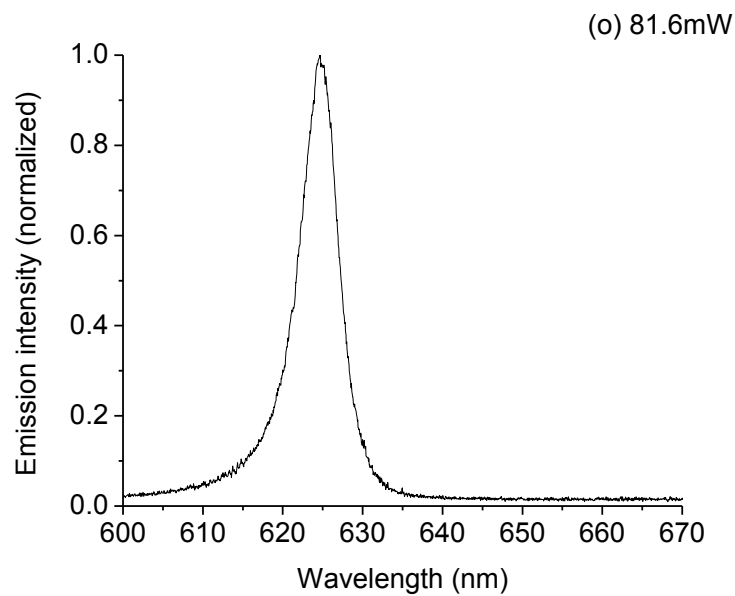


**Fig. 5.4(o). Emission spectrum of POF random lasers for incident pump power of 81.6mW.**

**Table 5.1. The spectral linewidth of the highest discrete lasing peak of each emission spectrum in Figure 5.2(d)-(h)**

Pump Power (mW)	Peak $\lambda$ (nm)	Linewidth (nm)
26.9	626.4	0.49
30.2	632.8	0.58
36.0	628.1	0.52
39.8	630.1	0.50
44.3	628.4	0.52

At very low pumping intensity and below the lasing threshold, as shown in Fig. 5.4(a)-(c), only a very broad spontaneous emission peak with a flat top is observed in the spectrum. The increase in gain cannot exceed the loss caused by the light scattering in the gain medium, only spontaneous emission occurs at any frequencies leading to a broad emission peak.

It can be seen in Fig. 5.4(d) that when the pumping intensity exceeds the lasing threshold, discrete narrow lasing lines with large intensity emerge and superimpose to the fluorescence in the emission spectrum [1]. The average linewidth, as shown in Table 5.1, of these discrete narrow peaks is about 0.5nm, which is 10 times much

narrower than the linewidth of the ASE at high excitation power in the emission spectrum. Since the gain exceeds the loss in the cavities formed by the recurrent scattering of light, laser oscillation with coherent feedback occurs in these cavities leading to emerging of discrete narrow lasing lines in the emission spectrum.

On the other hand, it is observed in Fig. 5.4(d)-(h) that the discrete lasing lines locate mainly near the gain maximum in addition to a red shift. Each discrete lasing line corresponds to a lasing mode. It is easily understood that near the gain maximum the gain obtained by the lasing modes exceeds the loss in the cavities. Among these discrete lasing modes, the emission intensities are different, and only one lasing mode emerges with maximum intensity with the single-shot pumping intensity. It is clear that mode competition or gain competition occurs between the lasing modes.

Moreover, the number of lasing modes does not increase with the pumping intensity above the lasing threshold, which is different from what Y. Ling, H. Cao and their co-workers [2, 3] have observed in their amplifying disordered polymer film. Furthermore, the spectral spacing, which is 0.91nm on average as shown in Table 5.2 of section 5.3.3, between each lasing mode does not change as the pumping

intensity increases during the whole excitation process. Because the nanoparticles are located in fixed positions in the solid-state gain medium, the frequencies of the lasing modes, which is related to the mean free path, do not change with repeated single-shot optical excitation.

When the pumping intensity increases further, the overall emission intensity of the discrete lasing modes grow rapidly and reach a maximum at pumping intensity of 36.0mW, as shown in Fig. 5.4(f). Then the overall emission intensity starts to decrease in accompany with an intensity increase and spectral narrowing of the amplified spontaneous emission (ASE) peak with higher pumping intensity. When the pumping intensity is extremely high as shown in Fig. 5.4(i), the discrete lasing lines disappear abruptly and only the amplified spontaneous emission (ASE) peak retain in the spectrum. This phenomenon may be caused by the photo-bleaching or thermal-bleaching of the organic dyes under high optical excitation strength.

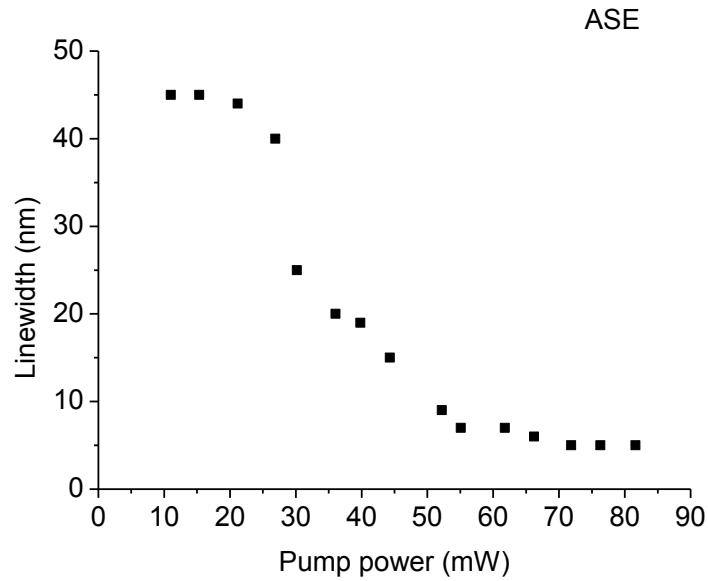


**Fig. 5.5. Spectral linewidth of the ASE in the random lasing spectrum with pump power.**

At even higher pumping intensity, the fluorescence in the emission spectrum, as shown in Fig. 5.4(a)-(o), narrows down with the pumping intensity, which behaves like typical dye-doped POF. This global narrowing with the pump power is also observed by H. Cao and her co-workers [4]. The spectral linewidth of the ASE peak is illustrated in Fig. 5.5. The linewidth of the ASE is 45nm at low excitation power, and then dramatically narrows down to 5nm at high excitation power. A laser-like threshold is also observed at about 30mW.

### 5.3.3 Lasing mode analysis of POF random lasers

Fig. 5.6 illustrates the positions of the discrete narrow lasing modes for the pumping

powers above lasing threshold. It can be seen that there are 10 observable discrete lasing modes in each emission spectrum with different excitation power. The spectral position of each lasing mode does not change from pulse to pulse excitation; however, the emission intensity of each lasing mode in the emission spectrum is different for each single-shot excitation power.

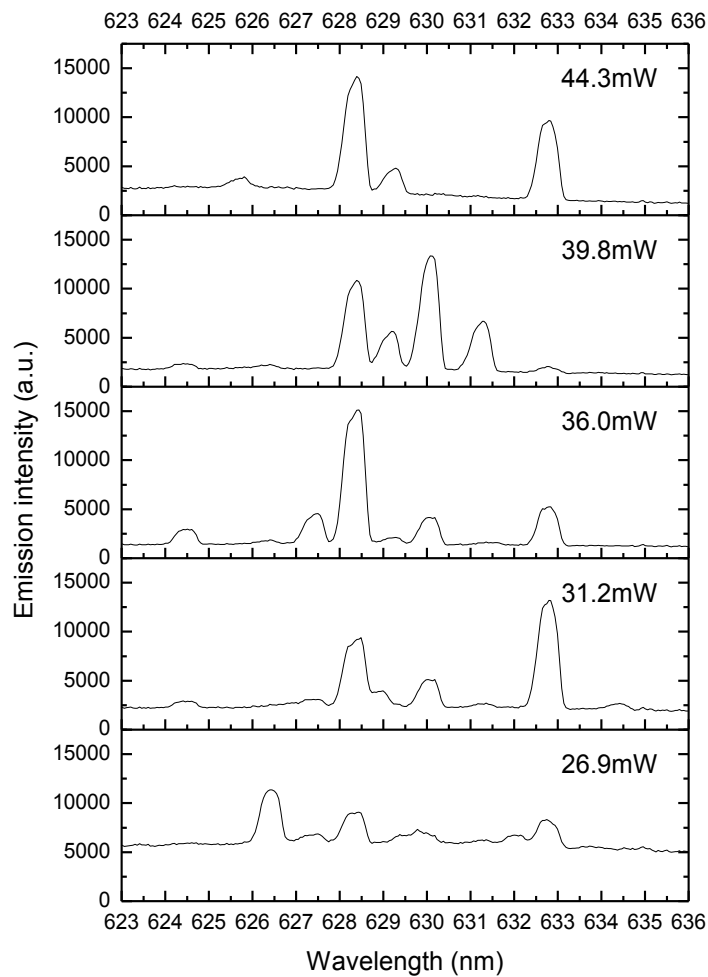


**Fig. 5.6. Distribution of discrete lasing modes in the emission spectra with pumping power of 26.9mW, 31.2mW, 36.0mW, 39.8mW, and 44.3mW (bottom to top).**

The lasing mode positions and the corresponding spectral spacing between adjacent modes are listed in Table 5.2.

**Table 5.2. Lasing mode positions and the corresponding spectral spacing between adjacent lasing modes.**

Mode (nm)		Mode spacing, $\Delta\lambda$ (nm)	
$\lambda_1$	624.5	$\lambda_2 - \lambda_1$	1.1
$\lambda_2$	625.6	$\lambda_3 - \lambda_2$	0.8
$\lambda_3$	626.4	$\lambda_4 - \lambda_3$	1.0
$\lambda_4$	627.4	$\lambda_5 - \lambda_4$	0.9
$\lambda_5$	628.3	$\lambda_6 - \lambda_5$	0.9
$\lambda_6$	629.2	$\lambda_7 - \lambda_6$	0.9
$\lambda_7$	630.1	$\lambda_8 - \lambda_7$	1.1
$\lambda_8$	631.2	$\lambda_9 - \lambda_8$	0.9
$\lambda_9$	632.1	$\lambda_{10} - \lambda_9$	0.6
$\lambda_{10}$	632.7	$\langle \Delta\lambda \rangle$	0.91

It is clear in Table 5.2 that the lasing modes are more or less equally spaced. It is also found that the average separation between adjacent lasing modes is 0.91nm which is similar to the spacing observed by H. Cao and her co-workers in their

PMMA film containing Rh640 dye and TiO<sub>2</sub> nanoparticles [5]. This spacing is limited by the room temperature homogeneous linewidth of Rh640 in PMMA [5].

## 5.4 Conclusion

In summary, we have demonstrated, for the first time, random lasing action with coherent and resonant feedback in POF inside which the core was doped with Rh640 organic laser dyes and dispersed with TiO<sub>2</sub> nanoparticles. The observation of discrete narrow lasing peaks is a strong evidence that coherent and resonant feedback is provided by recurrent scattering of light in the passive medium of randomly distributed nanoparticles, and stimulated emission occurs in the amplifying gain resonators formed. It is clear with evidence that diffusive system can exhibit discrete lasing lines with coherent feedback. It was observed that the number of discrete narrow lasing modes, their spectral positions, and the spectral spacing between each lasing modes were the same for repeated single-shot pumping above threshold. This reliable lasing behavior phenomenon led to long term lasing wavelengths stability, which cannot always be found in other liquid core fiber random lasers [6], or in liquid based polymer random laser. Since the random laser is in the fiber form, single mode operation can be expected with specific laser designs.

## 5.5 Reference

1. M. Leonetti, C. Conti, and C. López, “Random laser tailored by directional stimulated emission”, *Phys. Rev. A*, Vol. 85, 043841 (2012)
2. Y. Ling, H. Cao, A. L. Burin, M. A. Ratner, X. Yu, and R. P. H. Chang, “Investigation of random lasers with resonant feedback”, *Phys. Rev. A*, Vol. 64, 063808 (2001)
3. H. Cao, Xunya Jiang, Y. Ling, J. Y. Xu, and C. M. Soukoulis, “Mode repulsion and mode coupling in random lasers”, *Phys. Rev. B*, Vol. 67, 161101 (2003)
4. H. Cao and Y. G. Zhao, “Random laser action in semiconductor powder”, *Phys. Rev. Lett.*, Vol. 82, 2278 (1999)
5. H. Cao, Xunya Jiang, Y. Ling, J. Y. Xu, and C. M. Soukoulis, “Mode repulsion and mode coupling in random lasers”, *Phys. Rev. B*, Vol. 67, 161101 (2003)
6. Christiano J. S. de Matos, Leonardo de S. Menezes, Antônio M. Brito-Silva, M. A. Martinez Gámez, Anderson S. L. Gomes, and Cid B. de Araújo, “Random fiber laser”, *Phys. Rev. Lett.*, Vol. 99, 153903 (2007)

## **CHAPTER 6**

# **Effect of Scatterers Concentration on Lasing Properties of POF Random Lasers**

### **6.1 Introduction**

Since the optical feedback in a random laser is provided by multiple scattering of light in a disordered medium, the density of scatterers or the scattering mean free path plays an important role in the ultimate emission characteristic such as number of modes, mode spacing, spectral linewidth, etc. By making characterization of many fiber samples, a better understanding of the major working principle of a random laser can be achieved. Moreover, it leads to the possibility of using the random laser as a sensor for anything that modifies the scattering characteristics of the medium. So sensing is certainly one potential application through altering the scattering mean free path by heating or cooling the fiber or stretching the fiber.

In this chapter, by changing the TiO<sub>2</sub> nanoparticles density in the samples, the amount of scattering can be varied in order to study the effect of TiO<sub>2</sub> nanoparticles density on the lasing action in POF random laser under optical excitation; and to observe the transition from ASE to random lasing, and again to ASE. The

investigation was divided into two parts. In the first part, dye-doped POFs with low density of TiO<sub>2</sub> nanoparticles were fabricated and characterized. In the second part, dye-doped POFs with high density of TiO<sub>2</sub> nanoparticles were also fabricated and characterized. In order to prevent the sedimentation of TiO<sub>2</sub> nanoparticles during the polymerization process encountered in the preliminary studies in Chapter 5, a rotating system for the polymerization process was developed. The fabrication process of uniformly distributed TiO<sub>2</sub> nanoparticles in the dye-doped preform with different density of TiO<sub>2</sub> nanoparticles is demonstrated in Section 6.2. After that the characterization method and results of lasing spectra of fibers are discussed in Section 6.3. The conclusion is shown in Section 6.4.

## 6.2 Fabrication of POF random lasers

In this experiment, a series of dye-doped preforms with low concentration of TiO<sub>2</sub> nanoparticles were fabricated and drawn into fibers. The structure of the dye-doped fibers is the same as that shown in Fig. 5.1 in Chapter 5. The length of the fibers are 5cm. The TiO<sub>2</sub> particle density  $\rho$  were 10ppm ( $6.69 \times 10^7 \text{ cm}^{-3}$ ), 15ppm ( $1.00 \times 10^8 \text{ cm}^{-3}$ ), 20ppm ( $1.34 \times 10^8 \text{ cm}^{-3}$ ), 25ppm ( $1.67 \times 10^8 \text{ cm}^{-3}$ ), and 40ppm ( $2.67 \times 10^8 \text{ cm}^{-3}$ ). Another series of dye-doped preforms with high concentration of TiO<sub>2</sub> nanoparticles were also prepared. The particle density  $\rho$  were 100ppm ( $6.69 \times 10^8 \text{ cm}^{-3}$ ), 600ppm

( $4.01 \times 10^9 \text{ cm}^{-3}$ ), and 1000ppm ( $6.69 \times 10^9 \text{ cm}^{-3}$ ). Assume the  $\text{TiO}_2$  nanoparticles are spherical and do not absorb light. The scattering mean free path  $l_s$  was estimated numerically by Equation 3.9 in Chapter 3. The corresponding calculated values of  $l_s$  for the dye-doped POF with low concentration of  $\text{TiO}_2$  nanoparticles were listed in Table 6.1. On the other hand, the corresponding calculated values of  $l_s$  for the dye-doped POF with high concentration of  $\text{TiO}_2$  nanoparticles were listed in Table 6.2. The concentration of Rh640 dye was fixed at 800ppm (1.3mM) for all fibers.

**Table 6.1. The particle density and scattering mean free path for the series of dye-doped POF with low concentration of  $\text{TiO}_2$  nanoparticles.**

$\rho$	$l_s$
$6.69 \times 10^7 \text{ cm}^{-3}$	2.38 cm
$1.00 \times 10^8 \text{ cm}^{-3}$	1.59 cm
$1.34 \times 10^8 \text{ cm}^{-3}$	1.19 cm
$1.67 \times 10^8 \text{ cm}^{-3}$	0.95 cm
$2.67 \times 10^8 \text{ cm}^{-3}$	0.60 cm

**Table 6.2. The particle density and scattering mean free path for the series of dye-doped POF with high concentration of TiO<sub>2</sub> nanoparticles.**

$\rho$	$l_s$
$6.69 \times 10^8 \text{ cm}^{-3}$	0.24 cm
$4.01 \times 10^9 \text{ cm}^{-3}$	396 $\mu\text{m}$
$6.69 \times 10^9 \text{ cm}^{-3}$	238 $\mu\text{m}$

The pre-polymerization process is the same as that used in the fabrication of preform in the previous chapters. In the process, the Rh640 dye was firstly added in the MMA monomer solution, and the mixture was heated at 80°C on a hotplate stirrer. Until the dye was completely dissolved in the MMA monomer solution, TiO<sub>2</sub> nanoparticles were then gradually introduced into the solution. The mixture solution was then stirred on the hotplate until it became viscous. The viscous mixture was then quickly poured into several pure PMMA tubes. The tubes were covered with permeable membranes to prevent the mixture come out and to ensure that the gases produced can go out during the chemical reaction in the polymerization process. The tubes were finally mounted on a rotating system as shown in Figure 6.1.

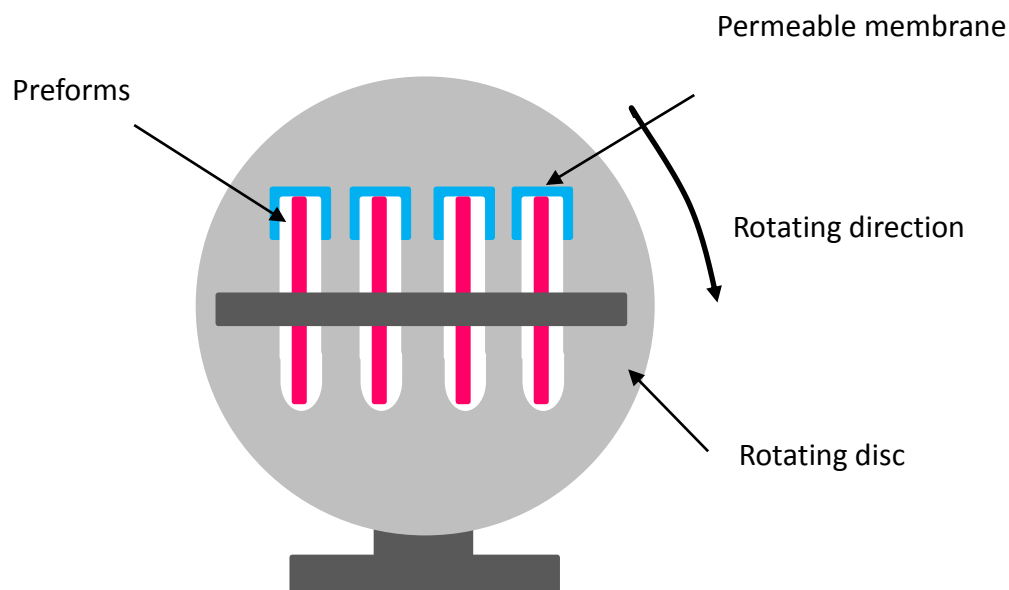


**Fig. 6.1. Rotating system for ensuring the uniform distribution of  $\text{TiO}_2$**

**nanoparticles in the dye-doped core materials during the long duration (4-5 days) of the preform polymerization (curing) stage. The whole system is put in an oven during the whole polymerization process.**

The rotating machine with the tubes was put in an oven. The tubes were rotated at a very slow speed during the polymerization process in the oven for four days. Since the tubes were rotated during the polymerization process, a uniform distribution of  $\text{TiO}_2$  nanoparticles in dye-doped preform could be obtained. When the polymerization process completed, the preforms were then drawn into fibers for emission characterization.

## **6.3 Emission spectra of POF random lasers**

The lasing spectra characterization of dye-doped POF with low and high density of TiO<sub>2</sub> nanoparticles were demonstrated respectively in Section 6.3.1 and 6.3.2. Again, the fibers were 5cm long. The fibers are transversely pumped by a ( $\lambda=532\text{nm}$ ) frequency-doubled Q-switched Nd:YAG pulse laser. The emission spectra were measured at fiber ends and recorded by a spectrometer with 0.2nm resolution.

### **6.3.1 Lasing spectra characterization of dye-doped POF with low concentration of TiO<sub>2</sub> nanoparticles**

The emission spectra of the dye-doped POF with low concentration of TiO<sub>2</sub> nanoparticles namely 10ppm ( $6.69 \times 10^7 \text{ cm}^{-3}$ ), 15ppm ( $1.00 \times 10^8 \text{ cm}^{-3}$ ), 20ppm ( $1.34 \times 10^8 \text{ cm}^{-3}$ ), 25ppm ( $1.67 \times 10^8 \text{ cm}^{-3}$ ), and 40ppm ( $2.67 \times 10^8 \text{ cm}^{-3}$ ) for three different power of pumping pulse were reported respectively in Fig. 6.2, 6.3, 6.4, 6.5, and 6.6.

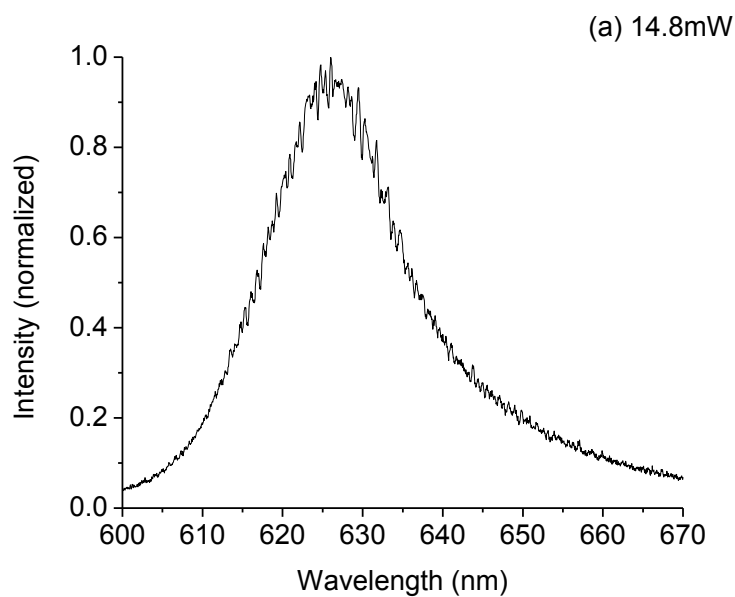


**Fig. 6.2(a). Emission spectra of 800ppm (1.3mM) Rh640 dye-doped POF with 10ppm ( $6.69 \times 10^7 \text{ cm}^{-3}$ ) of TiO<sub>2</sub> nanoparticles for pump power of 14.8mW.**

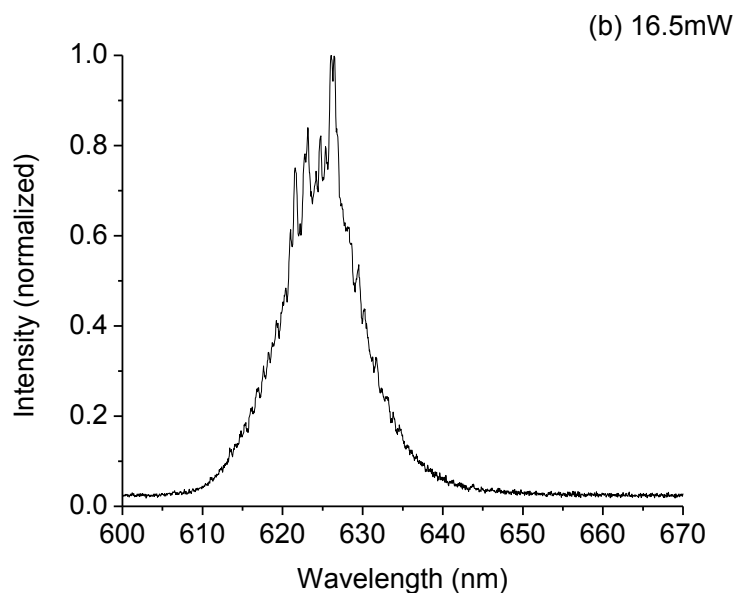


**Fig. 6.2(b). Emission spectra of 800ppm (1.3mM) Rh640 dye-doped POF with 10ppm ( $6.69 \times 10^7 \text{ cm}^{-3}$ ) of TiO<sub>2</sub> nanoparticles for pump power of 16.5mW.**

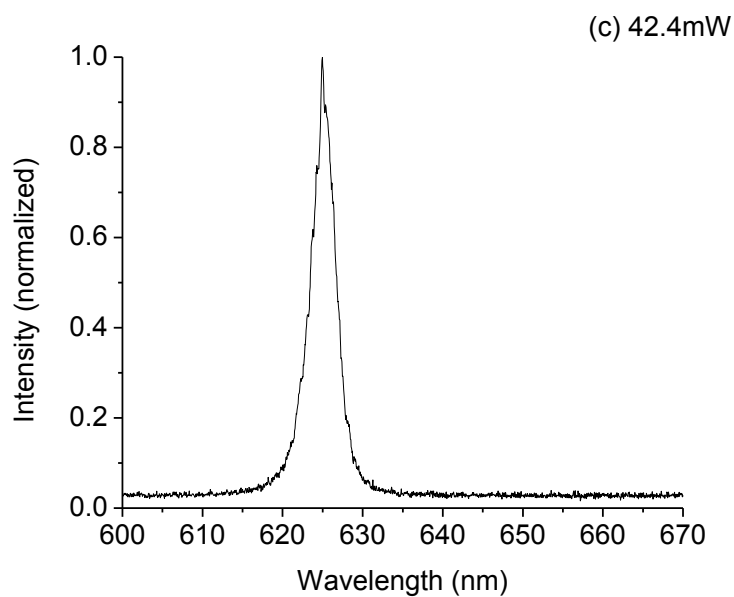


**Fig. 6.2(c).** Emission spectra of 800ppm (1.3mM) Rh640 dye-doped POF with 10ppm ( $6.69 \times 10^7 \text{ cm}^{-3}$ ) of  $\text{TiO}_2$  nanoparticles for pump power of 42.4mW.

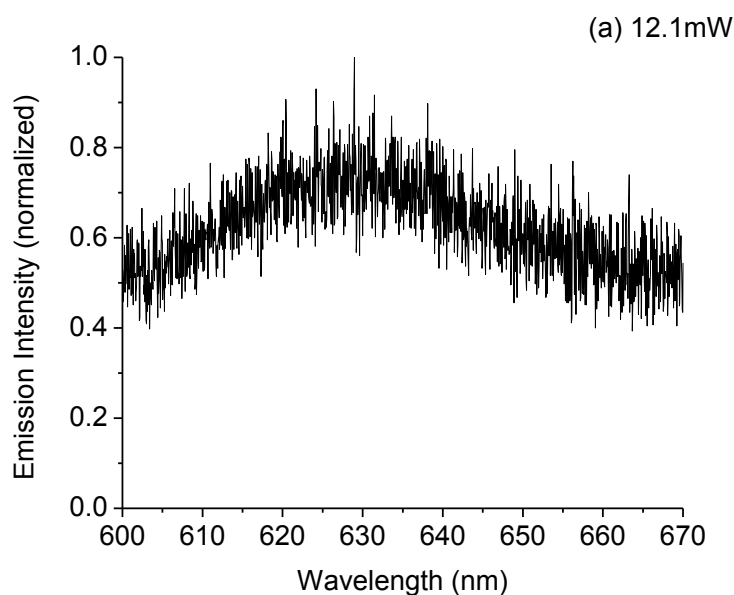


**Fig. 6.3(a).** Emission spectra of 800ppm (1.3mM) Rh640 dye-doped POF with 15ppm ( $1.00 \times 10^8 \text{ cm}^{-3}$ ) of  $\text{TiO}_2$  nanoparticles for pump power of 12.1mW.

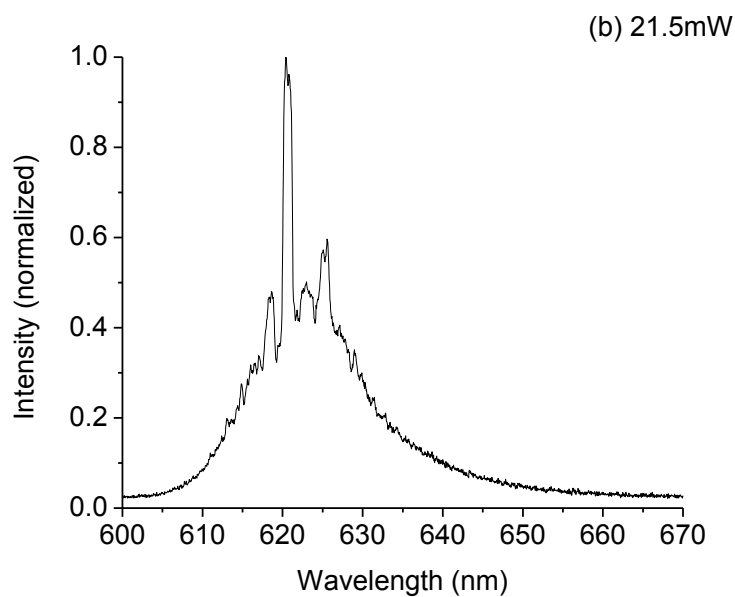


**Fig. 6.3(b). Emission spectra of 800ppm (1.3mM) Rh640 dye-doped POF with 15ppm ( $1.00 \times 10^8 \text{ cm}^{-3}$ ) of  $\text{TiO}_2$  nanoparticles for pump power of 21.5mW.**

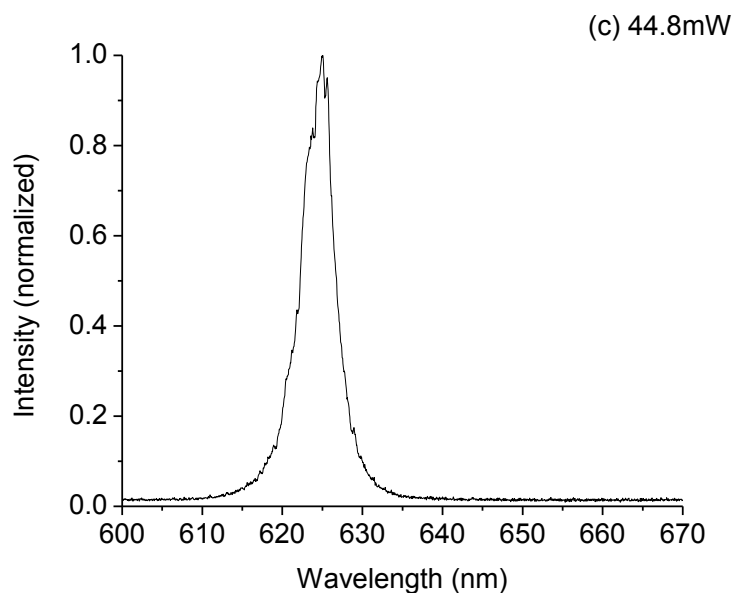


**Fig. 6.3(c). Emission spectra of 800ppm (1.3mM) Rh640 dye-doped POF with 15ppm ( $1.00 \times 10^8 \text{ cm}^{-3}$ ) of  $\text{TiO}_2$  nanoparticles for pump power of 44.8mW.**

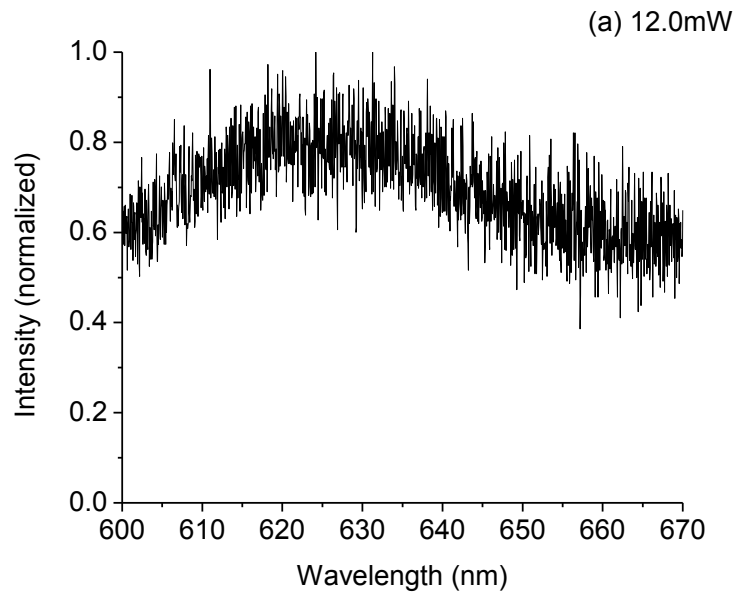


**Fig. 6.4(a).** Emission spectra of 800ppm (1.3mM) Rh640 dye-doped POF with 20ppm ( $1.34 \times 10^8 \text{ cm}^{-3}$ ) of  $\text{TiO}_2$  nanoparticles for pump power of 12.0mW.

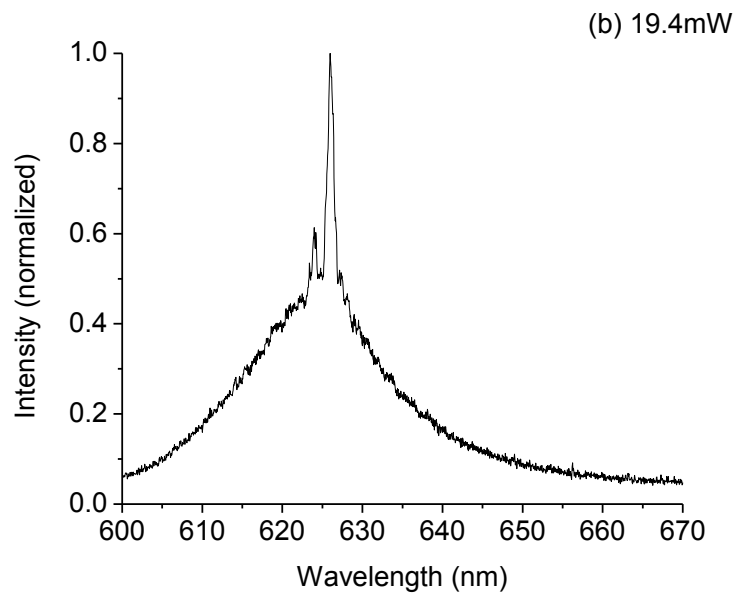


**Fig. 6.4(b).** Emission spectra of 800ppm (1.3mM) Rh640 dye-doped POF with 20ppm ( $1.34 \times 10^8 \text{ cm}^{-3}$ ) of  $\text{TiO}_2$  nanoparticles for pump power of 19.4mW.

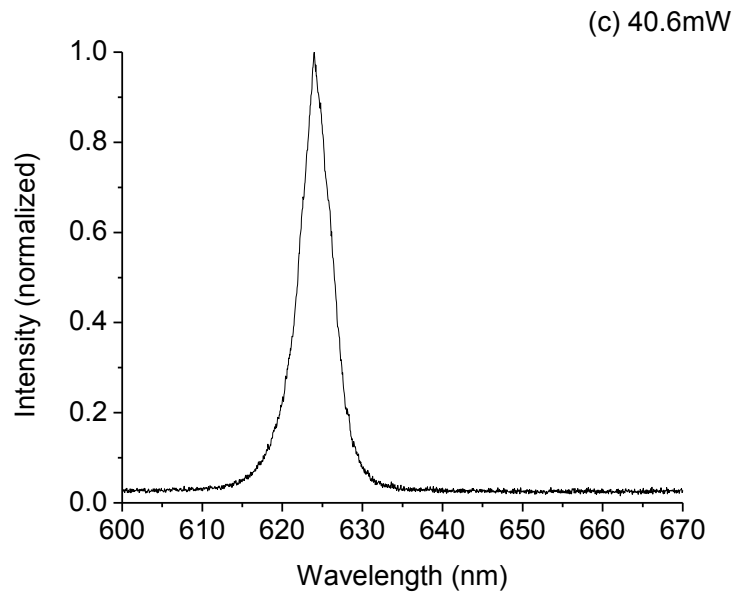


**Fig. 6.4(c).** Emission spectra of 800ppm (1.3mM) Rh640 dye-doped POF with 20ppm ( $1.34 \times 10^8 \text{ cm}^{-3}$ ) of  $\text{TiO}_2$  nanoparticles for pump power of 40.6mW.

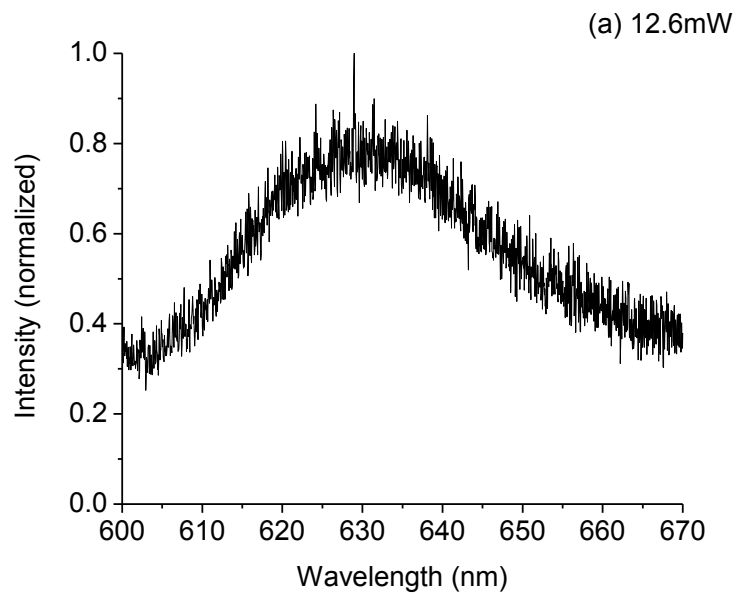


**Fig. 6.5(a).** Emission spectra of 800ppm (1.3mM) Rh640 dye-doped POF with 25ppm ( $1.67 \times 10^8 \text{ cm}^{-3}$ ) of  $\text{TiO}_2$  nanoparticles for pump power of 12.6mW.

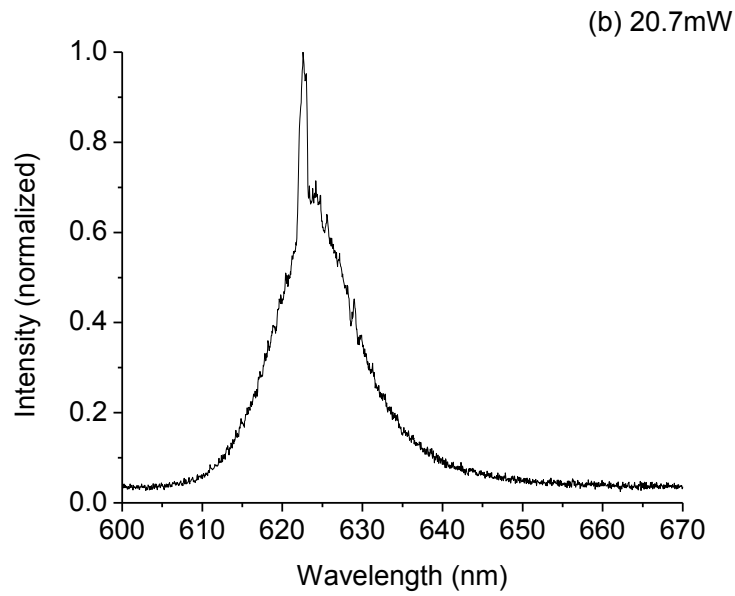


**Fig. 6.5(b).** Emission spectra of 800ppm (1.3mM) Rh640 dye-doped POF with 25ppm (1.67x10<sup>8</sup> cm<sup>-3</sup>) of TiO<sub>2</sub> nanoparticles for pump power of 20.7mW.

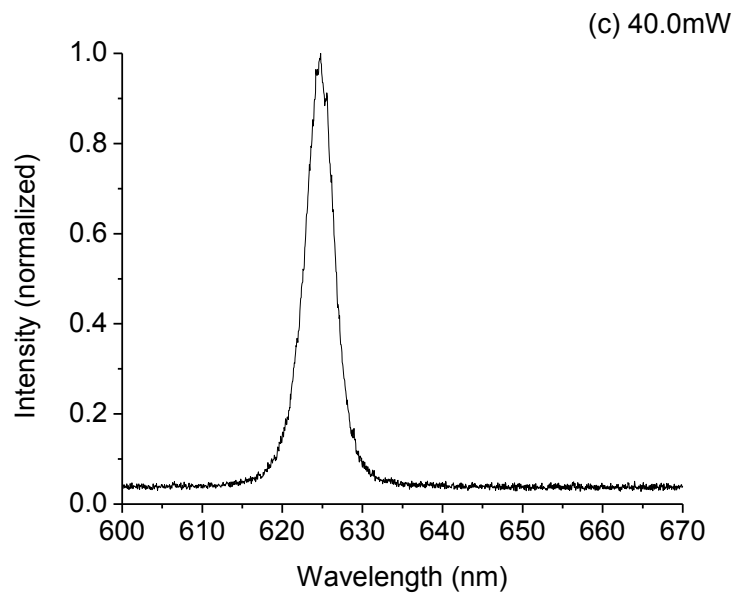


**Fig. 6.5(c).** Emission spectra of 800ppm (1.3mM) Rh640 dye-doped POF with 25ppm (1.67x10<sup>8</sup> cm<sup>-3</sup>) of TiO<sub>2</sub> nanoparticles for pump power of 40.0mW.

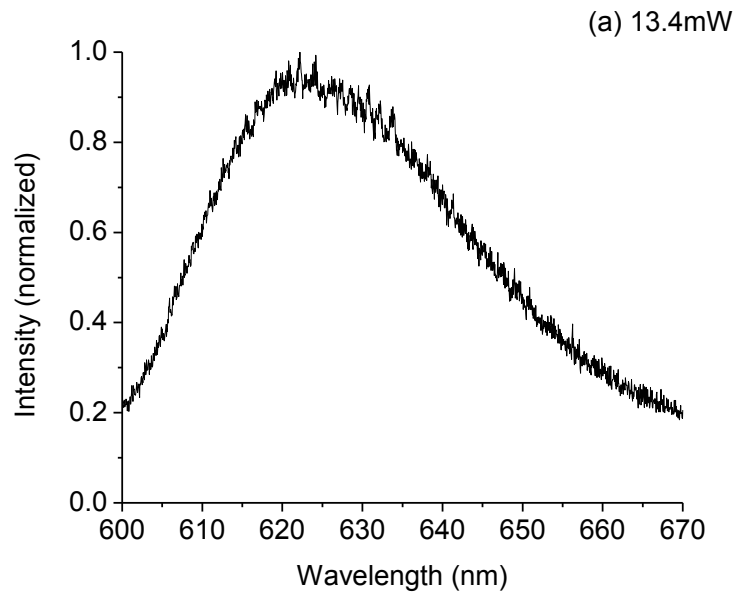


**Fig. 6.6(a).** Emission spectra of 800ppm (1.3mM) Rh640 dye-doped POF with 40ppm ( $2.67 \times 10^8 \text{ cm}^{-3}$ ) of TiO<sub>2</sub> nanoparticles for pump power of 13.4mW.

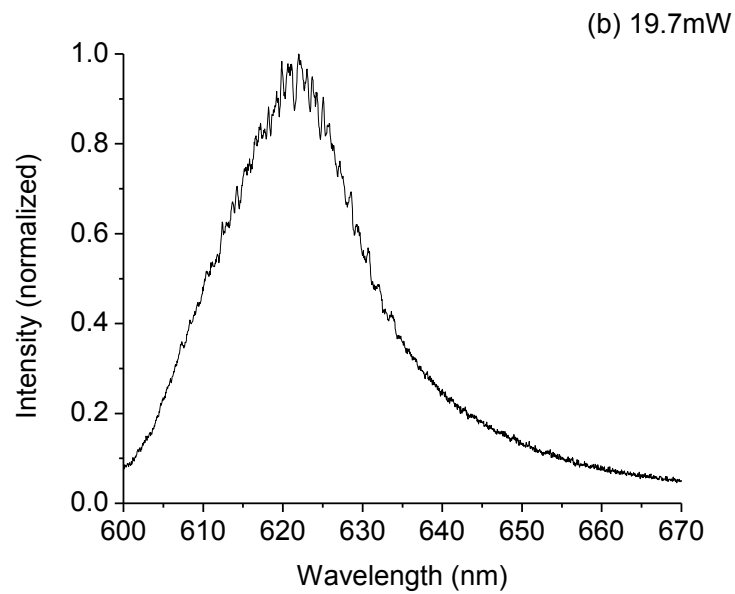


**Fig. 6.6(b).** Emission spectra of 800ppm (1.3mM) Rh640 dye-doped POF with 40ppm ( $2.67 \times 10^8 \text{ cm}^{-3}$ ) of TiO<sub>2</sub> nanoparticles for pump power of 19.7mW.

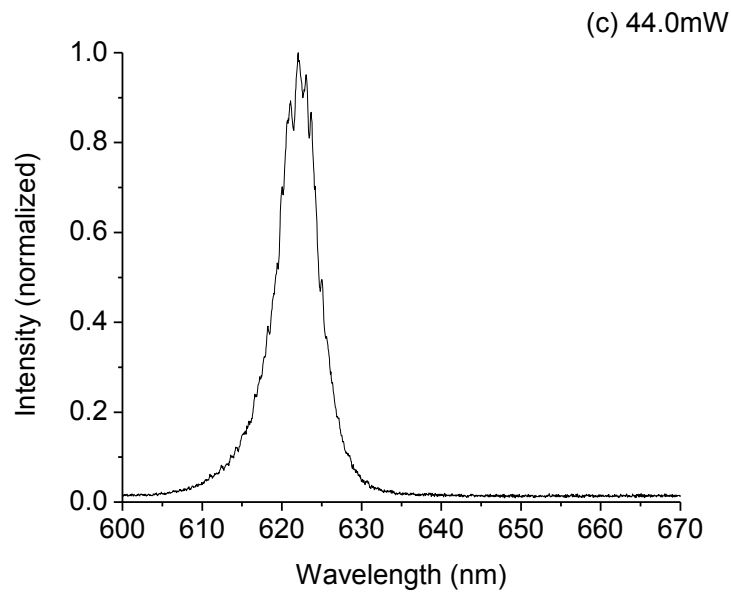


**Fig. 6.6(c). Emission spectra of 800ppm (1.3mM) Rh640 dye-doped POF with 40ppm ( $2.67 \times 10^8 \text{ cm}^{-3}$ ) of  $\text{TiO}_2$  nanoparticles for pump power of 44.0mW.**

At low concentration of  $\text{TiO}_2$  nanoparticles and below the lasing threshold, as shown in Fig. 6.2(a), 6.3(a), 6.4(a), 6.5(a), and 6.6(a), only a very broad spontaneous emission peak with a flat top is observed in the spectrum. The increase in gain cannot exceed the loss caused by the light scattering in the gain medium, only spontaneous emission occurs at any frequencies leading to a broad emission peak. However, very different lasing spectra are observed for the fibers near lasing threshold. In Fig. 6.2(b), near the threshold, discrete narrow random lasing peaks are observed in the emission spectrum of fiber with 10ppm ( $6.69 \times 10^7 \text{ cm}^{-3}$ ) concentration of  $\text{TiO}_2$  nanoparticles. However, the emission intensity and the

spectral position of the random lasing peaks are quite frustrating.

Next, as shown in Fig. 6.3(b), when the density of TiO<sub>2</sub> nanoparticles was increased to 15ppm ( $1.00 \times 10^8 \text{ cm}^{-3}$ ), discrete random lasing peaks with uniform spectral spacing between adjacent peaks are observed near lasing threshold. These random lasing spectrum is similar to the results observed in Chapter 5 in which the concentration of TiO<sub>2</sub> nanoparticles in the dye-doped fiber cannot be determined due to the sedimentation of TiO<sub>2</sub> nanoparticles during polymerization process. It can be seen in Fig. 6.4(b) that the number of narrow random lasing peaks significantly decreased when the concentration of TiO<sub>2</sub> nanoparticles was increased to 20ppm ( $1.34 \times 10^8 \text{ cm}^{-3}$ ). There are only two narrow lasing peaks in the emission spectra near and above threshold. The number of narrow lasing peaks further reduced to one when the concentration of TiO<sub>2</sub> nanoparticles was increased to 25ppm ( $1.67 \times 10^8 \text{ cm}^{-3}$ ). It is important to note that single mode POFRL was realized in this configuration. However, there is no random lasing peaks in the emission spectra in the case of 40ppm ( $2.67 \times 10^8 \text{ cm}^{-3}$ ) TiO<sub>2</sub> nanoparticles dye-doped fiber with pump power near and above threshold.

### 6.3.2 Lasing spectra characterization of dye-doped POF with high concentration of TiO<sub>2</sub> nanoparticles

Fig. 6.7 to 6.9 illustrates the lasing spectra of dye-doped POF with high concentration of TiO<sub>2</sub> nanoparticles below threshold, near threshold, and above lasing threshold.

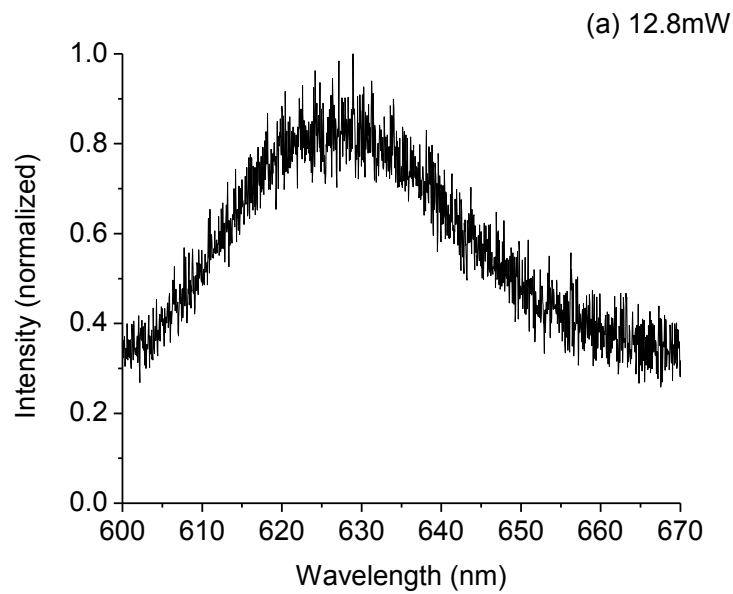


**Fig. 6.7(a). Emission spectra of 800ppm (1.3mM) Rh640 dye-doped POF with 100ppm ( $6.69 \times 10^8 \text{ cm}^{-3}$ ) of TiO<sub>2</sub> nanoparticles for pump power of 12.8mW.**

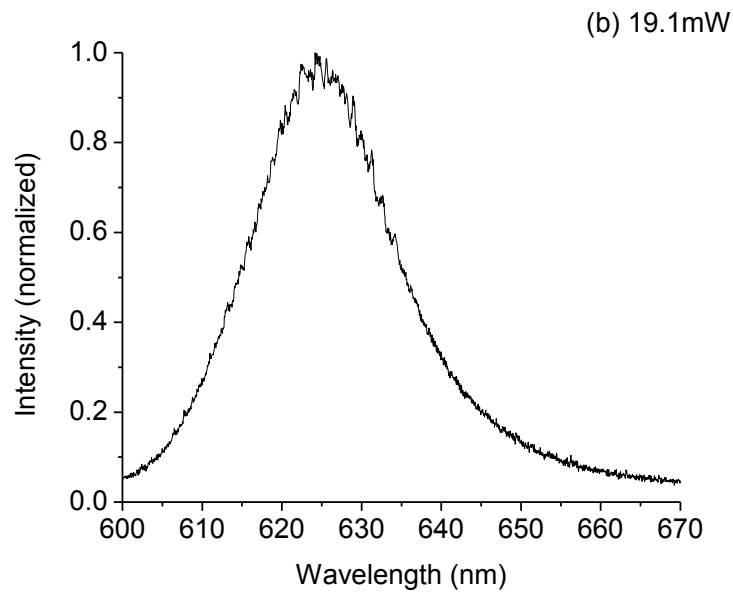


**Fig. 6.7(b).** Emission spectra of 800ppm (1.3mM) Rh640 dye-doped POF with 100ppm ( $6.69 \times 10^8 \text{ cm}^{-3}$ ) of  $\text{TiO}_2$  nanoparticles for pump power of 19.1mW.

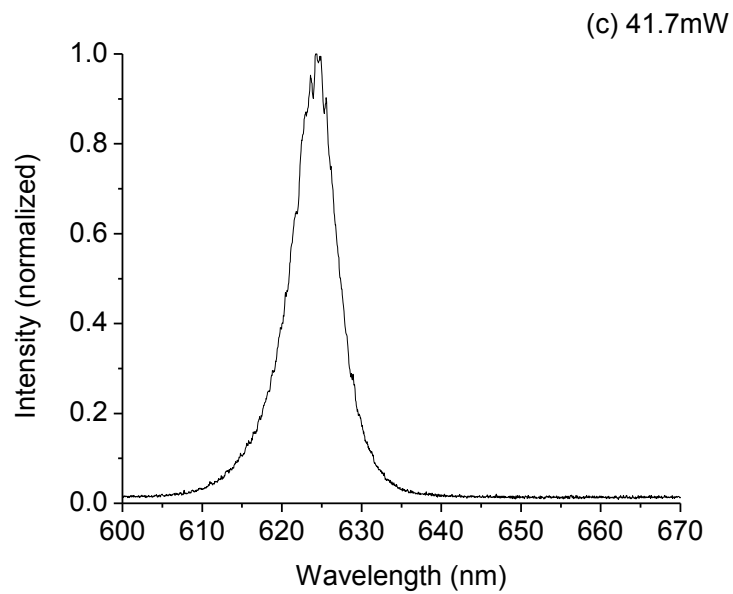


**Fig. 6.7(c).** Emission spectra of 800ppm (1.3mM) Rh640 dye-doped POF with 100ppm ( $6.69 \times 10^8 \text{ cm}^{-3}$ ) of  $\text{TiO}_2$  nanoparticles for pump power of 41.7mW.

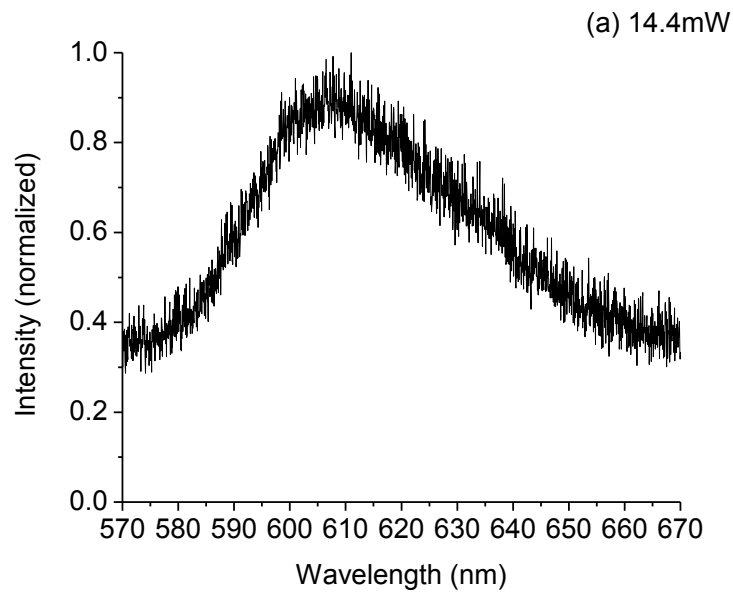


**Fig. 6.8(a).** Emission spectra of 800ppm (1.3mM) Rh640 dye-doped POF with 600ppm ( $4.01 \times 10^9 \text{ cm}^{-3}$ ) of  $\text{TiO}_2$  nanoparticles for pump power of 14.4mW.

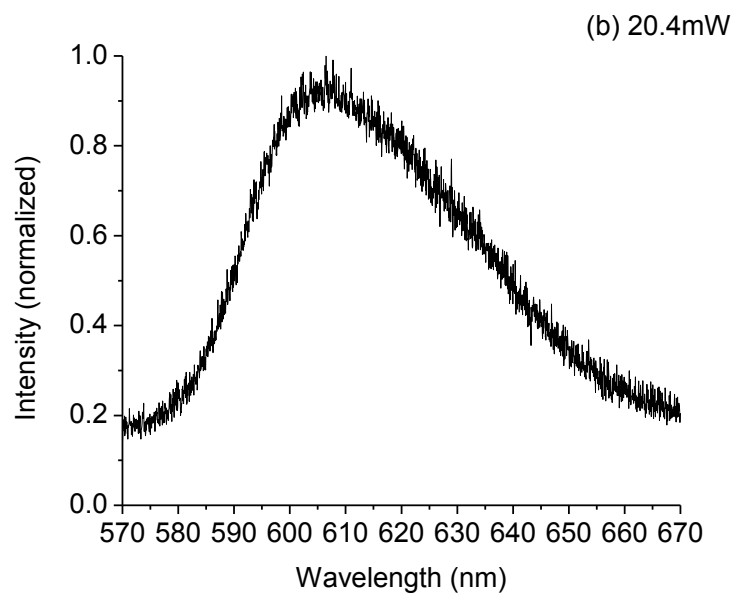


**Fig. 6.8(b).** Emission spectra of 800ppm (1.3mM) Rh640 dye-doped POF with 600ppm ( $4.01 \times 10^9 \text{ cm}^{-3}$ ) of  $\text{TiO}_2$  nanoparticles for pump power of 20.4mW.

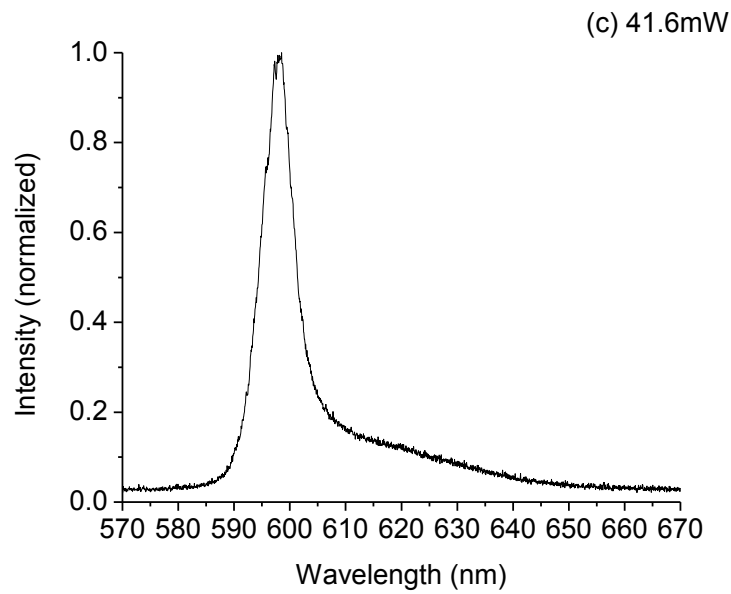


**Fig. 6.8(c).** Emission spectra of 800ppm (1.3mM) Rh640 dye-doped POF with 600ppm ( $4.01 \times 10^9 \text{ cm}^{-3}$ ) of  $\text{TiO}_2$  nanoparticles for pump power of 41.6mW.

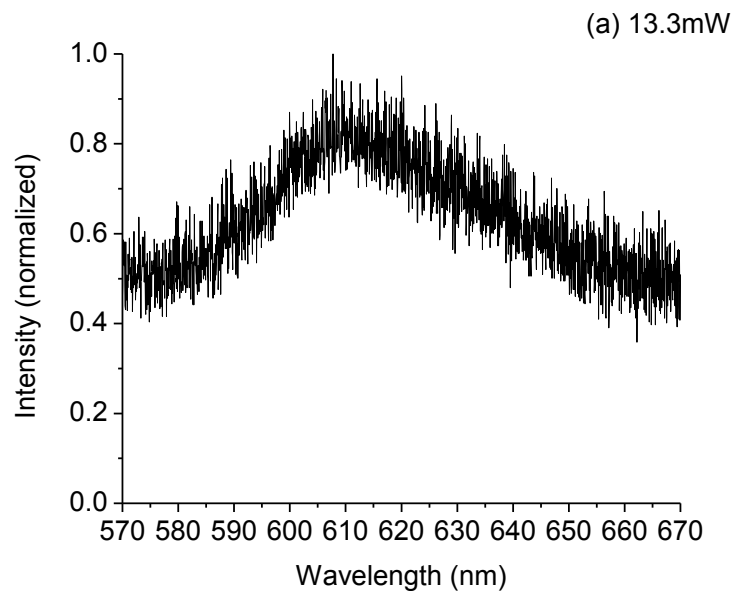


**Fig. 6.9(a).** Emission spectra of 800ppm (1.3mM) Rh640 dye-doped POF with 1000ppm ( $6.69 \times 10^9 \text{ cm}^{-3}$ ) of  $\text{TiO}_2$  nanoparticles for pump power of 13.3mW.

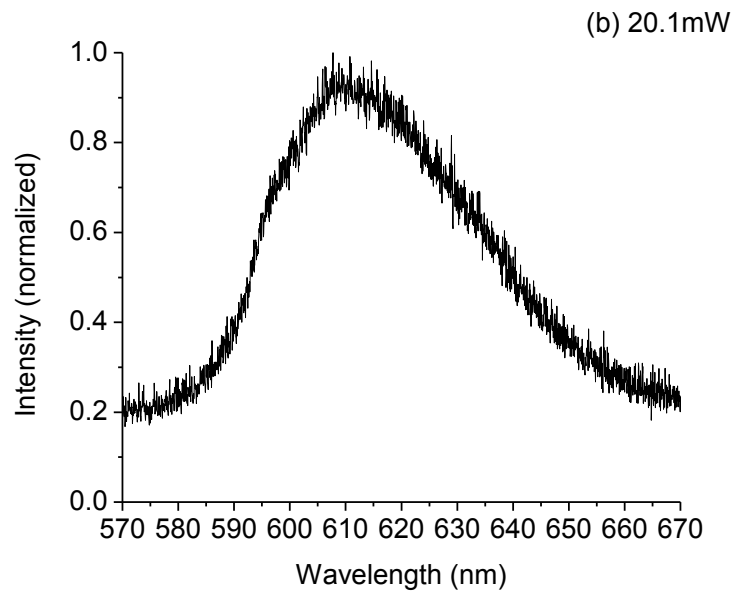


**Fig. 6.9(b).** Emission spectra of 800ppm (1.3mM) Rh640 dye-doped POF with 1000ppm ( $6.69 \times 10^9 \text{ cm}^{-3}$ ) of  $\text{TiO}_2$  nanoparticles for pump power of 20.1mW.

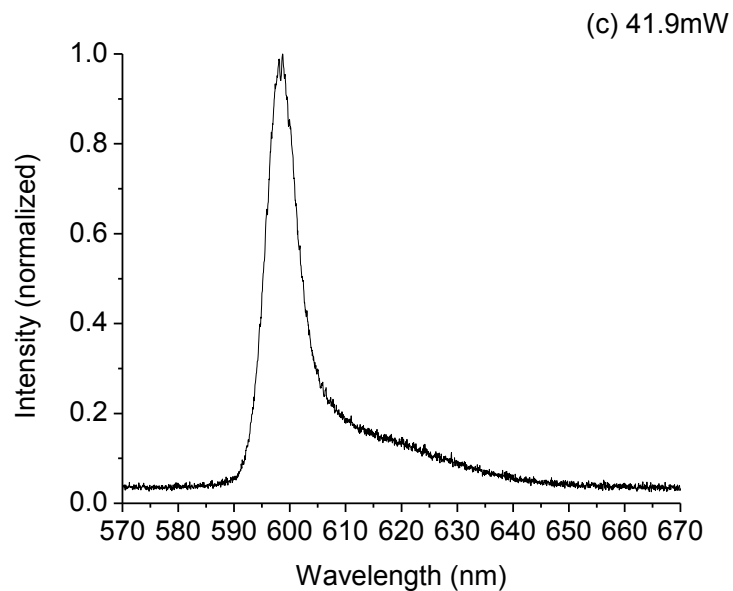


**Fig. 6.9(c).** Emission spectra of 800ppm (1.3mM) Rh640 dye-doped POF with 1000ppm ( $6.69 \times 10^9 \text{ cm}^{-3}$ ) of  $\text{TiO}_2$  nanoparticles for pump power of 41.9mW.

It can be seen in Fig. 6.7 to Fig. 6.9 that there are no observable discrete lasing modes in the emission spectra for all fibers with high concentration of TiO<sub>2</sub> nanoparticles. Only narrowing of fluorescence are observed in the emission spectra with increasing pumping power. Although the transporting path of light was lengthened and the dwelling time of light was prolonged in the gain medium by increasing the concentration of TiO<sub>2</sub> nanoparticles, the gain obtained by the light cannot exceed the loss encountered in the medium.

### **6.3.3 Effect of scatterers concentration on random laser threshold**

In Fig. 6.10, the pump power at the lasing threshold is plotted against the TiO<sub>2</sub> nanoparticle density for the samples characterized in this chapter. At particle density of  $0.067 \times 10^9 \text{ cm}^{-3}$ , random lasing started at 16.5mW. When the particle density increased to  $0.10 \times 10^9 \text{ cm}^{-3}$ , the threshold pump power decreased gradually to 12.6mW. Then the threshold started to rise at  $0.10 \times 10^9 \text{ cm}^{-3}$  and went up with the particle density. When the particle density increased up to  $26.7 \times 10^9 \text{ cm}^{-3}$ , no random lasing peaks were observed. Therefore, the threshold pump power was found experimentally to depend on the scattering mean free path. These effect was also observed in the weakly scattering systems by X. Wu and the co-workers [1, 2]. The particles played an essential role in the lasing process in the scattering gain

medium because random lasing peaks did not appear in emission spectra of the neat dye-doped sample.

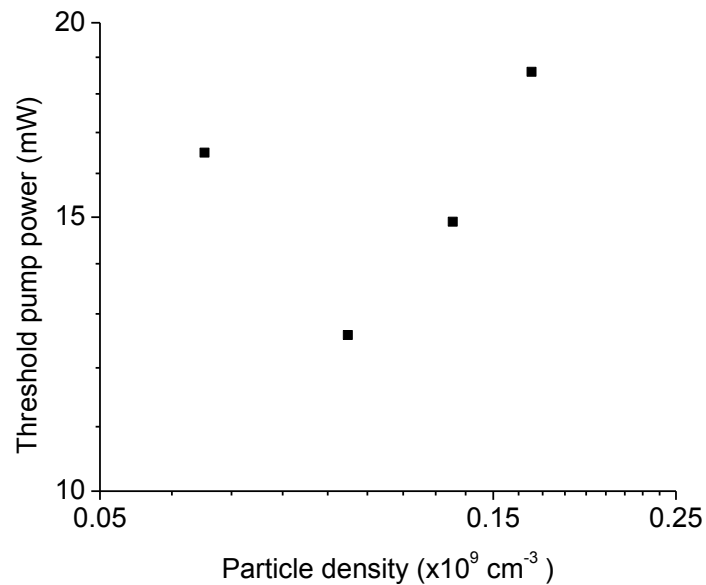


**Fig. 6.10.** The random laser threshold as a function of the  $\text{TiO}_2$  nanoparticle density. The concentration of Rh640 dye is 800ppm (1.3mM).

## **6.4 Theoretical investigation of statistical regimes in random laser emission**

Although there are a few experimental studies conducted on the emission characteristics of different random laser materials as well as theoretical models [3, 4, 5] reported in literature, a clear and accurate theory to explain and interpret the

occurrence of the random lasing peaks in the experimental results is still lacking. Recently, a numerical model in a theoretical work, based on an intensity feedback that does not include the effects of the field interference, have been proposed [6, 7]. The model shows that the emission spectra of random laser can be approximated by three statistical regimes: an initial Gaussian regime is followed by Lévy statistics, and Gaussian statistics is recovered again for high pump power. These different statistical regimes are possible in a weakly diffusive active medium, while the region of Lévy statistics disappears when the medium is strongly diffusive presenting always a Gaussian regime with a smooth emission spectrum [6, 7]. The numerical analysis is performed by a Monte Carlo simulation of a two-dimension model with a square sample size. The simulation consists of three steps in each iteration: (1) Spontaneous emission, (2) Diffusion, and (3) Stimulated emission. The numerical results of different statistical regimes are then obtained by changing the value of scattering mean free path.

In this section, we presented a theoretical model of random lasing based on Monte Carlo simulation of light being scattered and amplified in our dye-doped core POF with immobile scatters. The simulation is adopted from the work done by Wiersma and co-workers in [6, 7]. The theoretical study of random lasing phenomenon in a

weakly diffusive regime ( $\lambda \ll l_s$ ) using the numerical model is based on an intensity feedback. In other words, the light beams propagate independently in the model, hence the effects of the interference of backscattering light are not considered.

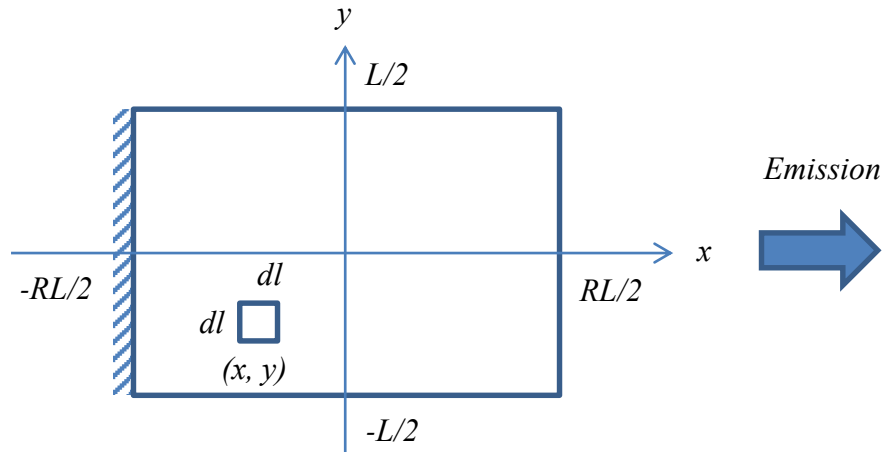


**Fig. 6.11. Schematic diagram of two-dimensional (2D) model of length  $RL$  and height  $L$ . A square unit of length  $dl$  at position  $(x, y)$  is shown. The shaded area on the left hand side denotes the reflective mirror on the fiber end-face.**

In Fig. 6.11, the sample model is a two-dimensional (2D) rectangle partitioned into square units of equal size with length  $dl$ . The position of each square unit is identified by a vector index  $(x, y)$  where  $x$  and  $y$  are integers in the range of  $-RL/2 \leq x \leq RL/2$  and  $-L/2 \leq y \leq L/2$ , respectively. The sample is  $RL$  long and  $L$  height and the total number of units is  $RL^2$  where  $R$  is the fiber aspect ratio.

The amplifying medium is considered as a simple three-level system with population inversion  $N(x, y)$  when excited by pumping. At time  $t = 0$ , the initial population distribution  $N_0(x, y)$  is assumed to have a Gaussian distribution:

$$N(t = 0, x, y) = N_0(x, y) = A \exp\left(-\frac{x^2 + y^2}{2\sigma^2}\right) \quad \text{Equation 6.1}$$

The normalization factor  $A$  is assigned to have an initial energy  $E$  of excitation:

$$E = \hbar\omega_p \int_{-L/2}^{L/2} \int_{-RL/2}^{RL/2} N_0(x, y) dx dy \quad \text{Equation 6.2}$$

The propagation of light in the sample is described in terms of a large number of random walkers, and each walker carries a number of photons  $n_i$  with a randomly assigned frequency  $\omega_i$  around the central frequency  $\omega_0$ . The assigned frequency  $\omega_i$  is obtained randomly from a Cauchy distribution of random number with full-width at half-maximum  $2w$ .

The numerical simulation consists of three steps running in a loop for each time step  $dt$ :

1. Spontaneous emission. For each square unit, a spontaneous emission event can randomly occurs with a probability of  $\gamma_0 N(x, y) dt$ , where  $\gamma_0$  denotes the spontaneous emission rate of a single atom. If the event occurs, the population inversion  $N(x, y)$  is reduced by one:

$$N(x, y) \rightarrow N(x, y) - 1 \quad \text{Equation 6.3}$$

Hence a new walker is generated with an initial number of photons  $n_i = 1$ , with an assigned frequency  $\omega_i$ , and with a random initial propagating direction. The total number of walkers  $M$  is then increased by one.

2. Diffusion with scattering and boundary condition. Each walker moves with equal probability to one of its four neighbors. In the present of scatters, each walker can undergo a scattering event with a probability determined by the scattering mean free path  $l_s$ . Its propagating direction changed randomly after the scattering event. If the walker reaches the boundary of  $x = -RL/2$  (reflective mirror coated fiber end-face in real situation), the walker is reflected back to the sample. If the walker reaches the boundary of  $y = -L/2$  or  $y = L/2$  (core/cladding interface of fiber), the walker is considered as leakage light beam,

and it is removed from the simulation and  $M$  is decreased by one. If the walker reaches the boundary of  $x = RL/2$ , the number of photons carried by it and its frequency are recorded for spectrum analysis. After a predetermined time steps, the numerical emission spectrum is formed by 1001 frequency channels ranging from -500 to 500 centered on channel 0 with a linewidth of  $w$  channels. The frequency (channel) of the spectrum relates to the experimental results shown in wavelength (nm).

3. Stimulated emission. The number of photons carried by each walker and the population inversion of each square unit are updated according to the following equations:

$$n_i \rightarrow n_i + [\gamma(\omega_i)Ndt]n_i \quad \text{Equation 6.4}$$

$$N(x, y) \rightarrow N(x, y) - [\gamma(\omega_i)n_idt]N(x, y) \quad \text{Equation 6.5}$$

where the stimulated emission coefficient  $\gamma(\omega_i)$  depends on the assigned frequency of each walker as follow:

$$\gamma(\omega_i) = \frac{\gamma_0}{1 + \left(\frac{\omega_i}{w}\right)^2} \quad \text{Equation 6.6}$$

It is important to note that despite each walker is independently generated and propagate in the sample, they all interact with the same population distribution during the simulation. In the simulation,  $dl = 1$  and  $dt = 1$  for simplicity. By choosing  $\gamma_0 = 10^{-4}$ ,  $w = 50$ ,  $\sigma = 80$ ,  $L = 320$ , and  $R = 1$  for first trial (real aspect ratio of fiber will be used in the future work of theoretical study), the simulation was performed by varying the excitation energy  $E$  through the initial population inversion distribution  $N(x, y)$  for three different values of  $l_s$  from 1 (strongest scattering strength) through 100 (modest scattering strength) to 200 (weakest scattering strength).

Fig. 6.12 shows the simulation results of the POF random lasers with  $l_s = 100$  for three different pump energies. The values of the pumping energy are chosen to be subthreshold, near threshold, and above the random laser threshold. For comparison, modest scattering POF random lasers with  $l_s = 1.59\text{cm}$  in this study is presented. In both theoretical and experimental results, it can be seen that an initial featureless emission spectrum is followed by a feature one and then a smooth featureless one with increasing pumping energy as observed in [7].

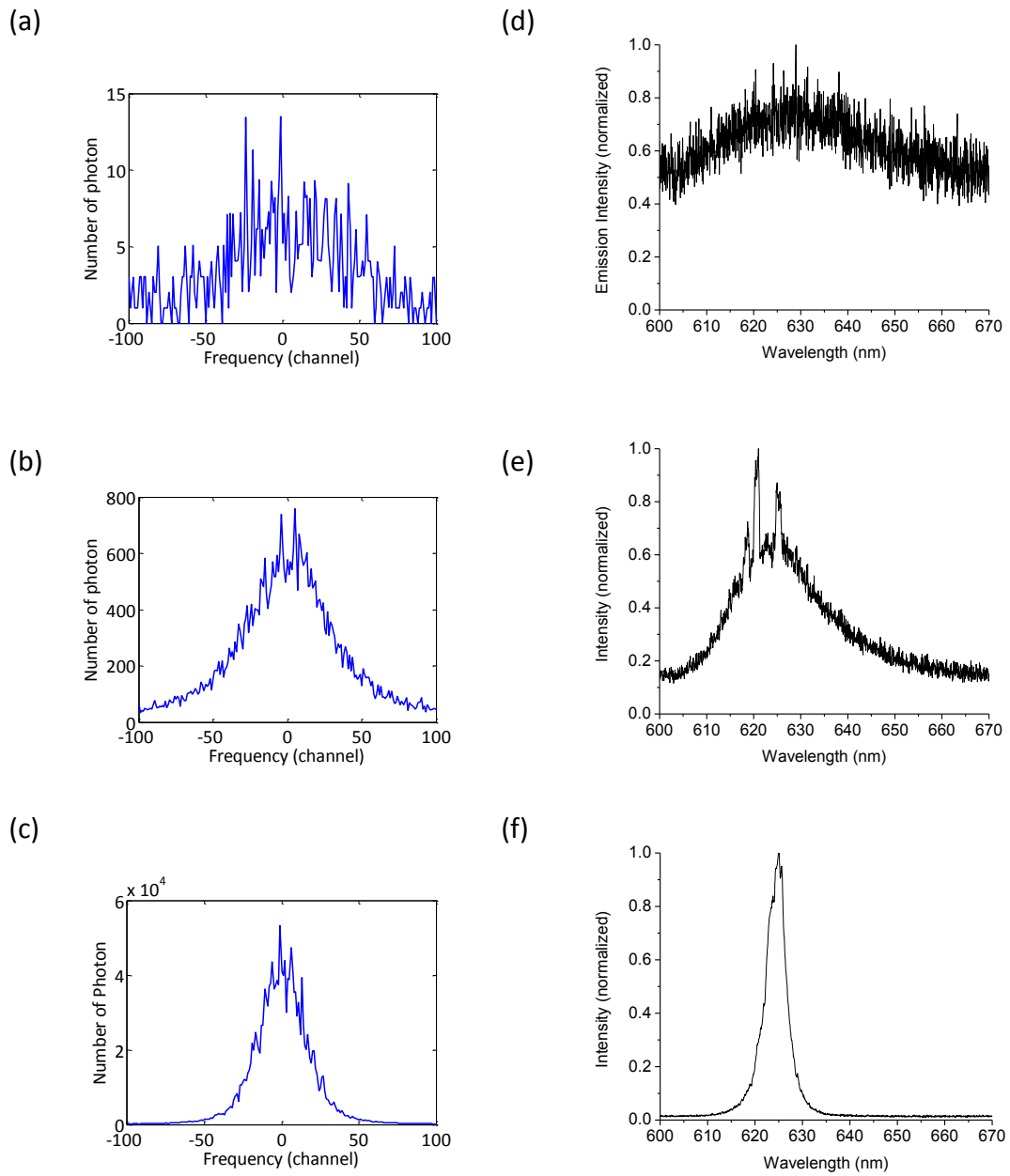


**Fig. 6.12. Numerical spectra for three different pumping energy in units of  $\hbar\omega_0$ :  $1 \times 10^5$  for (a),  $3 \times 10^6$  for (b) and  $9 \times 10^6$  for (c), for scattering mean free path  $l_s = 100$ . Experimental emission spectra of POF random laser for  $l_s = 1.59\text{cm}$  for three different pumping powers: 12.1mW for (d), 15.2mW for (e), and 44.8mW for (f).**

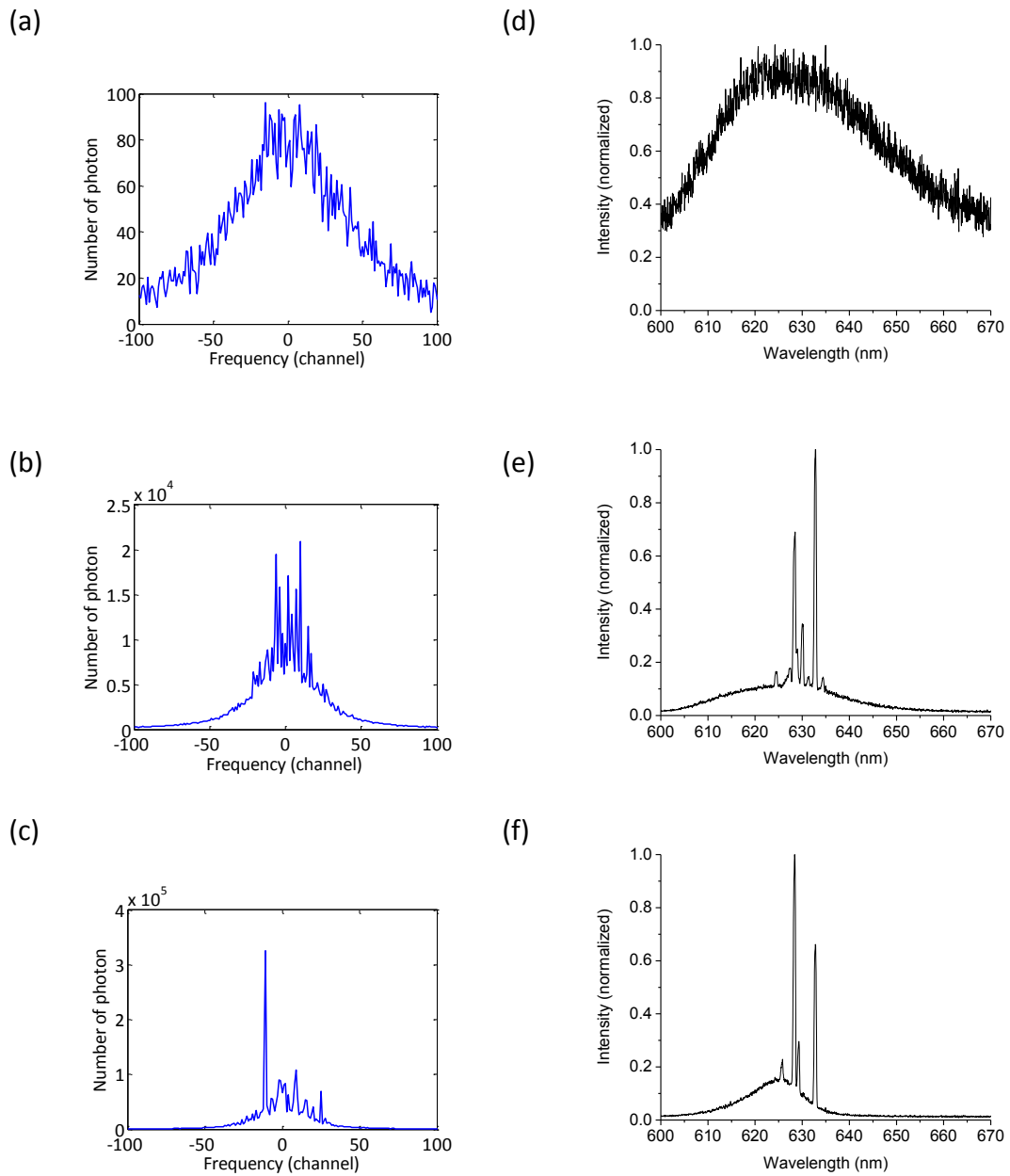


**Fig. 6.13. Numerical spectra for three pumping energies in units of  $\hbar\omega_0$ :  $3 \times 10^5$  for (a),  $6 \times 10^6$  for (b), and  $9 \times 10^6$  for (c), for extreme value of scattering mean free path  $l_s = 200$ . Experimental emission spectra of POF random laser from Chapter 5 for three different pumping powers: 15.3mW for (d), 30.2mW for (e), and 44.3mW for (f).**

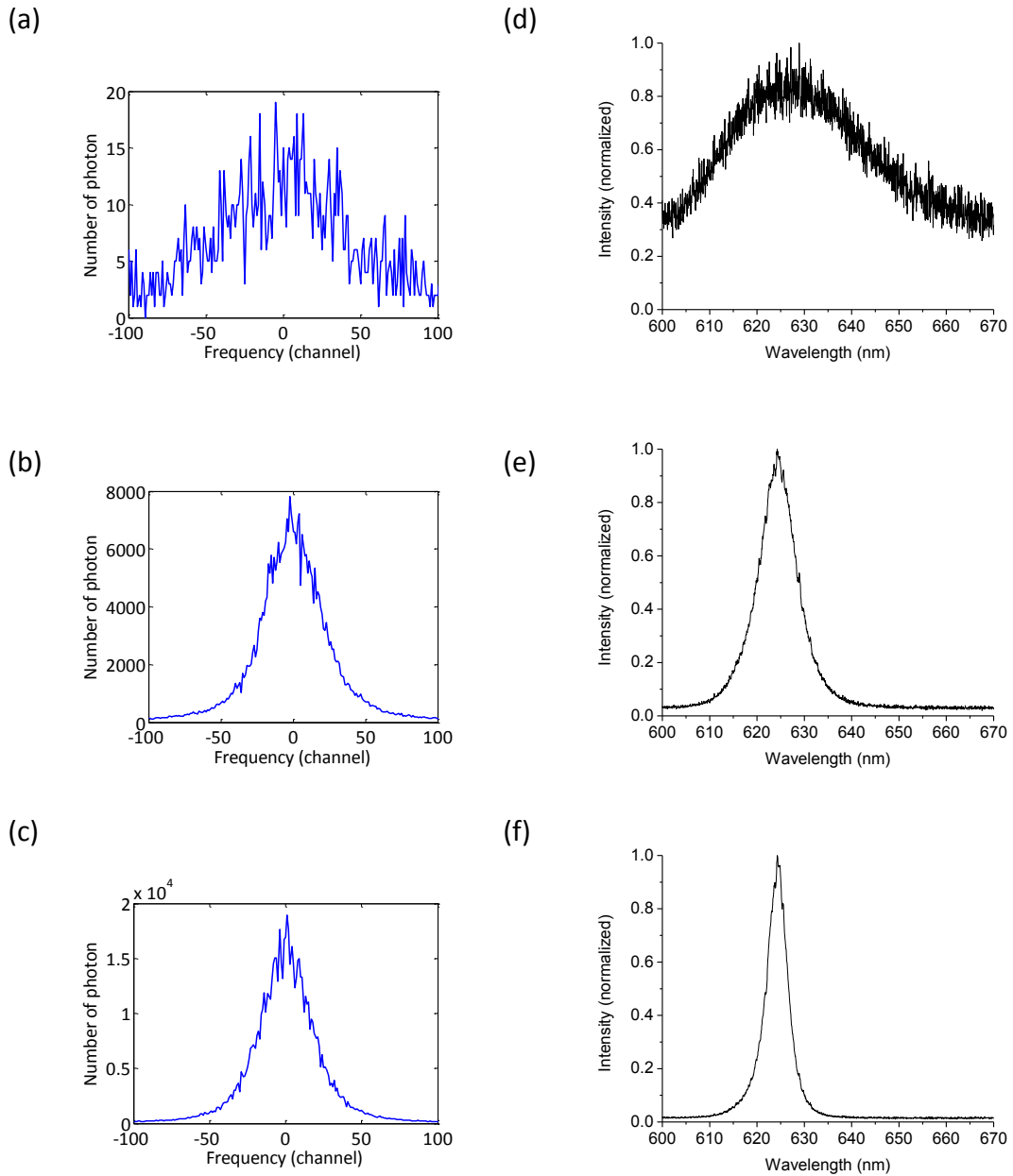


**Fig. 6.14. Numerical spectra for three pumping energies in units of  $\hbar\omega_0$ :  $1.5 \times 10^5$  for (a),  $6 \times 10^6$  for (b), and  $9 \times 10^6$  for (c), for extreme value of scattering mean free path  $l_s = 1$ . Experimental emission spectra of POF random laser for  $l_s = 0.24\text{cm}$  for three different pumping powers: 12.8mW for (d), 30.2mW for (e), and 43.4mW for (f). No random lasing peak is observed in the both strong scattering cases.**

In Fig. 6.13 and Fig. 6.14, numerical spectra of two extreme values of the scattering mean free path for similar pumping energies are reported. The numerical spectra in Fig. 6.13 was calculated with  $l_s = 200$ , that is, larger than the active region of pumping, and the numerical spectra in Fig. 6.14 was calculated with  $l_s = 1$ , which is much smaller than the active region of pumping. It can be seen that the spectra are completely different in the two regimes: In the weakly scattering regime ( $l_s = 200$ ) random lasing peaks appear even at larger pumping energy while in the strongly scattering regime ( $l_s = 1$ ) only smooth spectra are observed for any pumping energy. For comparison, weakly scattering and strongly scattering POF random lasers in this study are also presented in Fig. 6.13 and Fig. 6.14 respectively.

It can be seen that the experimental results in this study can ascertain the theory that emission spectra can be predicted by statistical regimes in random lasers. It is therefore polymer random fiber laser is an excellent medium to study random lasing action.

## 6.5 Conclusion

Rh640 dye-doped POF with low and high concentration of TiO<sub>2</sub> nanoparticles were fabricated, and their lasing properties were studied experimentally. The experimental results demonstrate that random lasing emerges only in weakly scattering medium (low concentration of TiO<sub>2</sub> nanoparticles or large scattering mean free path). A transition from random lasing emission to ASE was observed with increasing concentration of TiO<sub>2</sub> nanoparticles from 10ppm (large scattering mean free path) to 1000ppm (small scattering mean free path). A theoretical study of random lasing phenomenon using the method of numerical simulation was presented. It can be seen that the experimental emission spectra of amplifying disordered medium can be predicted by statistical investigation of photons transport in the medium. It is clear that the scattering mean free path plays an important role in determining the presence of random lasing in a scattering medium with gain. Moreover, single mode or multimode POFRL can be realized by changing the refractive index and size ratios of the fiber core and cladding. Single wavelength and multi-wavelength emissions can be realized by properly turning the scattering mean free path of the system. This encouraging result leads to the possibility of using the random laser as a sensor for anything that modifies the

scattering characteristics of the medium. So sensing is certainly one potential application.

## 6.6 Reference

1. H. Cao, "Lasing in random media", *Wav. Rand. Med.*, Vol. 13, R1 (2003)
2. X. Wu, W. Fang, A. Yamilov, A. A. Chabanov, A. A. Asatryan, L. C. Botten, and H. Cao, "Random lasing in weakly scattering systems", *Phys. Rev.*, Vol. 74, 053812 (2006)
3. X. Jiang and C. M. Soukoulis, "Time dependent theory for random lasers", *Phy. Rev. Lett.*, Vol. 85, 70 (2000)
4. M. Patra, "Theory for the photon statistics of random lasers", *Phy. Rev. A*, Vol. 65, 043809 (2002)
5. O. Zaitsev and L. Deych, "Recent developments in the theory of multimode random lasers", *J. Opt.*, Vol. 12, 024001 (2010)
6. S. Lepri, S. Cavalieri, G. Oppo, and D. S. Wiersma, "Statistical regimes of random laser fluctuations", *Phy. Rev. A*, Vol. 75, 063820 (2007)
7. E. Ignesti, F. Tommasi, L. Fini, S. Lepri, V. Radhalakshmi, D. Wiersma, and S. Cavalieri, "Experimental and theoretical investigation of statistical regimes in random laser emission", *Phy. Rev. A*, Vol. 88, 033820 (2013)

## **CHAPTER 7**

### **Conclusions and Suggestions for Future Research**

In this thesis, I report on the investigations of dye-doped POF ASE light source and on first demonstration of POF random laser. The experimental results are very interesting and encouraging.

The aim of this research is to study and demonstrate a simple plug-and-play and integrated-cavity POF laser. That is there are no excess optical components in the laser system except the pumping light source. My research study starts from making dye-doped POF in which the optical cavity is formed by directly coating a gold mirror of high reflectivity onto one fiber end-face, and another fiber end-face acts as an output coupler. The dye-doped optical fiber with optical excitation shows laser-like output characteristics. The emission spectrum narrows down dramatically when the excitation power is increased above the laser-like threshold. This spectral narrowing phenomenon can be considered as an ASE. Thereby the dye-doped POF can be used as an ASE light source in an integrated optical system.

To realize a true laser with simple structure as signified in the research objective, I have demonstrated a true laser action in the POF based on the idea of random lasing. Random lasing and conventional lasing differ greatly in optical feedback mechanism. For conventional laser, the optical feedback is provided by the cavity formed by two highly reflective mirrors, while for random laser, the feedback is mainly operated through recurrent multiple scattering of light. With this idea, I introduced TiO<sub>2</sub> nanoparticles into the dye-doped core of our POF. With optical excitation, the emitted light is scattered by the nanoparticles and amplified by the dye molecules, this recurrent scattering and amplification of light form a resonator for laser oscillation in the fiber. We name it “polymer optical fiber random laser”. The POF random laser shows discrete narrow lasing peaks with very high intensities in the emission spectrum. The linewidth of the discrete lasing peak is only 0.5nm which is 20 times smaller than that of ASE obtained in the dye-doped POF in the first part of my research work. It is clear with evidence that it is a true laser with coherent and resonant feedback. In this research, I have contributed the first realization of a POF random laser. I believe that the POF random laser can potentially be used in various areas from integrated photonics to biomedical systems. Moreover, I observed that the number of discrete narrow lasing modes, their spectral positions, and the spectral spacing between each lasing modes were

the same for repeated single-shot pumping above threshold. This reliable lasing behavior phenomenon led to long term lasing wavelengths stability, which cannot always be found in other liquid core fiber random lasers, or in liquid based polymer random laser. Since the random laser is in the fiber form, single mode operation can be expected with specific laser designs.

## APPENDIX 1

### Evaluation of Scattering Efficiency Factor by Mie Theory

#### A1.1

When the size of the scatterers is much larger than the wavelength of light that travels in the disordered medium, the scattering mean free path can be deduced by Mie theory.

Assume the scatterers are spherical particles of the scattering mean free path  $l_s$  of photons in a suspension of non-light-absorbing spherical particles of diameter  $d$  with a volume fraction  $\phi$  in a medium can be calculated by

$$l_s = \frac{2d}{3\phi Q_s}$$

, where  $Q_s$  is the scattering efficiency factor, and it can be evaluated numerically for spherical particles by Mie theory calculation. The scattering efficiency factor  $Q_s$  is defined as the ratio of the scattering cross section  $\sigma_s$  to the physical cross section ( $\pi r^2$ ) of the particle, that is  $Q_s = \sigma_s / (\pi r^2)$ .

Consider a spherical particle of radius  $r_0$  with complex electric permittivity  $\varepsilon = n^2$  embedded in a dielectric medium of permittivity  $\varepsilon_m = n_m^2$ . This particle is illuminated by a plane wave of angular frequency  $\omega = 2\pi c/\lambda_0 = kc/n_m$ .

A set of useful dimensionless parameters is defined as follows:

$$m = n/n_m$$

$$x = kr_0$$

$$\omega = mx$$

In these conditions, the total scattering cross section  $\sigma_s$  can be defined as the ratio of the total radiant power scattered by a particle in all directions, to the radiant power incident on the particle. It is given by

$$\sigma_s = \frac{\lambda^2}{2\pi} \sum_{n=1}^{\infty} (2n+1)(|a_n|^2 + |b_n|^2)$$

, where

$$a_n = \frac{m\psi_n(\omega)\psi'_n(v) - \psi_n(v)\psi'_n(\omega)}{m\psi_n(\omega)\xi'_n(v) - \xi_n(v)\psi'_n(\omega)}$$

$$b_n = \frac{\psi_n(\omega)\psi'_n(v) - m\psi_n(v)\psi'_n(\omega)}{\psi_n(\omega)\xi'_n(v) - m\xi_n(v)\psi'_n(\omega)}$$

In these expressions,  $\psi_n$  and  $\xi_n$  are Riccati-Bessel functions and are defined as follows:

$$\psi_n(x) = \sqrt{\frac{\pi x}{2}} J_{n+\frac{1}{2}}(x)$$

$$\xi_n(x) = \sqrt{\frac{\pi x}{2}} \left[ J_{n+\frac{1}{2}}(x) + iY_{n+\frac{1}{2}}(x) \right]$$

, where  $J_\nu$  and  $Y_\nu$  are the Bessel functions of the first and second order respectively.

These functions are solutions of the Bessel differential equation:

$$x^2 \frac{d^2 y}{dx^2} + 2x \frac{dy}{dx} + [x^2 - \nu(\nu + 1)]y = 0$$

While  $\varphi_n$  and  $\xi_n$  are the solutions of the following differential equation:

$$x^2 \frac{d^2 y}{dx^2} + [x^2 - n(n+1)]y = 0$$

And  $\psi_n$  and  $\xi_n$  can be expressed as a sum of sines and cosines.

For instance, the first terms are as follows:

$$\psi_0(x) = \sin(x)$$

$$\xi_0(x) = \sin(x) - i\cos(x)$$

$$\psi_1(x) = \frac{\sin(x)}{x} - \cos(x)$$

$$\xi_1(x) = \frac{\sin(x)}{x} - i \left[ \frac{\cos(x)}{x} + \sin(x) \right]$$

The sum over  $n$  can be restricted to only a few terms, up to  $n = N$ . Bohren and

Huffman [xxx] proposed the value  $N = v + 4v^{1/3} + 2$ .  $\leftarrow v$  is the size parameter

The primes indicate differentiation with respect to the argument in parenthesis. The

derivatives can be conveniently expressed as follows:

$$\psi'(x) = \psi_{n-1}(x) - \frac{n}{x} \psi_n(x)$$

$$\xi'(x) = \xi_{n-1}(x) - \frac{n}{x} \xi_n(x)$$

The MATLAB code used to determine the scattering cross section  $\sigma_s$  by numerically calculating the scattering efficiency factor  $Q_s$  is listed in the section A2.2.

## Reference

1. Guillaume Baffou, "Mie theory for metal nanoparticles", Chargé de recherche CNRS, Institut Fresnel, Université Aix-Marseille, France, (2012)
2. C. F. Bohren and D. R. Huffman, "Absorption and scattering of light by small particles", Wiley interscience, (1983)

## A1.2

MATLAB code:

```
%% SCATTERING BY A SPHERICAL TiO2 NANOPARTICLE USING MIE THEORY
%% inputs
% n_m refractive index of the medium
% lambda0 wavelength of light in nm
% r0 radius of the nanoparticle in nm
% N=5 maximum n-pole
function [Qext,Qsca,Qabs]=MieScattering2(lambda0,r0,n_m)
%% parameters
n_TiO2=sqrt(5.913+(0.2441/((lambda0/1000)^2-0.0803))); %refractive index of TiO2 from dispersion
formula
```

```

m=n_TiO2/n_m;
k=2*pi*n_m/lambda0;
x=k*r0;
z=m*x;
N=round(2+x+4*x^(1/3));
%% computation
j=(1:N);
sqr=sqrt(pi*x/2);
sqrM=sqrt(pi*z/2);
phi=sqr.*besselj(j+0.5,x);
xi=sqr.*(besselj(j+0.5,x)+i*bessely(j+0.5,x));
phim=sqrM.*besselj(j+0.5,z);
phi1=[sin(x), phi(1:N-1)];
phi1m=[sin(z), phim(1:N-1)];
y=sqr*bessely(j+0.5,x);
y1=[-cos(x), y(1:N-1)];
phip=(phi1-j/x.*phi);
phimp=(phi1m-j/z.*phim);
xip=(phi1+i*y1)-j/x.*(phi+i*y);
aj=(m*phim.*phip-phi.*phimp)./(m*phim.*xip-xi.*phimp);
bj=(phim.*phip-m*phi.*phimp)./(phim.*xip-m*xi.*phimp);
Qsca=sum( (2*j+1).*(abs(aj).*abs(aj)+abs(bj).*abs(bj)) );
Qext=sum( (2*j+1).*real(aj+bj) );
Qext=Qext*2*pi/(k*k);
Qsca=Qsca*2*pi/(k*k);
Qabs=Qext-Qsca;

```